

1 **Overview of the 2010 Carbonaceous Aerosols and Radiative Effects Study (CARES)**

2 R.A. Zaveri,¹ W.J. Shaw,¹ D.J. Cziczo,² B. Schmid,¹ R.A. Ferrare,³ M.L. Alexander,⁴ M. Alexandrov,⁵
3 R.J. Alvarez,⁶ W.P. Arnott,⁷ D.B. Atkinson,⁸ S. Baidar,⁹ R.M. Banta,⁶ J.C. Barnard,¹ J. Beranek,¹
4 L.K. Berg,¹ F. Brechtel,¹⁰ W.A. Brewer,⁶ J.F. Cahill,¹¹ B. Cairns,¹² C.D. Cappa,¹³ D. Chand,¹ S. China,¹⁴
5 J.M. Comstock,¹ M.K. Dubey,¹⁵ R.C. Easter,¹ M.H. Erickson,¹⁶ J.D. Fast,¹ C. Floerchinger,¹⁷
6 B.A. Flowers,¹⁵ E. Fortner,¹⁸ J.S. Gaffney,¹⁹ M.K. Gilles,²⁰ K. Gorkowski,¹⁴ W.I. Gustafson,¹
7 M. Gyawali,⁷ J. Hair,³ R.M. Hardesty,⁶ J.W. Harworth,⁸ S. Herndon,¹⁸ N. Hiranuma,¹ C. Hostetler,³
8 J.M. Hubbe,¹ J.T. Jayne,¹⁸ H. Jeong,²¹ B.T. Jobson,¹⁶ E.I. Kassianov,¹ L.I. Kleinman,²² C. Kluzek,¹
9 B. Knighton,¹⁷ K.R. Kolesar,¹³ C. Kuang,²² A. Kubátová,²¹ A.O. Langford,⁶ A. Laskin,⁴ N. Laulainen,¹
10 R.D. Marchbanks,⁶ C. Mazzoleni,¹⁴ F. Mei,²² R.C. Moffet,²³ D. Nelson,¹ M.D. Obland,³ H. Oetjen,⁹
11 T.B. Onasch,¹⁸ I. Ortega,⁹ M. Ottaviani,²⁴ M. Pekour,¹ K.A. Prather,¹¹ J.G. Radney,⁸ R.R. Rogers,³
12 S.P. Sandberg,⁶ A. Sedlacek,²² C.J. Senff,⁶ G. Senum,²² A. Setyan,²⁵ J.E. Shilling,¹ M. Shrivastava,¹
13 C. Song,¹ S.R. Springston,²² R. Subramanian,²⁶ K. Suski,¹¹ J. Tomlinson,¹ R. Volkamer,⁹
14 H.W. Wallace,¹⁶ J. Wang,²² A.M. Weickmann,⁶ D.R. Worsnop,¹⁸ X.-Y. Yu,¹ A. Zelenyuk,²⁷ and
15 Q. Zhang²⁵

16 ¹Atmospheric Sciences & Global Change Division, Pacific Northwest National Laboratory, Richland, WA, USA

17 ²Massachusetts Institute of Technology, Cambridge, MA, USA

18 ³NASA Langley Research Center, Hampton, VA, USA

19 ⁴Environmental Molecular Sciences Laboratory, Pacific Northwest National Laboratory, Richland, WA, USA

20 ⁵Department of Applied Physics and Applied Mathematics, Columbia University, New York, NY, USA

21 ⁶Chemical Sciences Division, NOAA Earth System Research Laboratory, Boulder, CO, USA

22 ⁷University of Nevada, Reno, NV, USA

23 ⁸Portland State University, Portland, OR, USA

24 ⁹Department of Chemistry and Biochemistry, University of Colorado at Boulder, CO, USA

25 ¹⁰Brechtel Manufacturing, Inc, Hayward, CA, USA

26 ¹¹University of California, San Diego, CA, USA

27 ¹²NASA Goddard Institute for Space Studies, New York, NY, USA

28 ¹³Department of Civil and Environmental Engineering, University of California, Davis, CA, USA

29 ¹⁴ Atmospheric Science Program, Michigan Technological University, Houghton, MI, USA

30 ¹⁵Los Alamos National Laboratory, Los Alamos, NM, USA

31 ¹⁶Washington State University, Pullman, WA, USA

32 ¹⁷Montana State University, Bozeman, MT, USA

33 ¹⁸Aerodyne Research, Inc., Billerica, MA, USA

34 ¹⁹University of Arkansas, Little Rock, AR, USA

35 ²⁰Lawrence Berkeley National Laboratory, Berkeley, CA, USA

36 ²¹University of North Dakota, ND, USA

37 ²²Brookhaven National Laboratory, Upton, NY, USA

38 ²³University of the Pacific, Stockton, CA, USA

39 ²⁴NASA Postdoctoral Program Fellow, NASA Goddard Institute for Space Studies, New York, NY, USA

40 ²⁵Department of Environmental Toxicology, University of California, Davis, CA, USA

41 ²⁶Droplet Measurements Technologies, Boulder, CO, USA

42 ²⁷Chemical and Materials Sciences Division, Pacific Northwest National Laboratory, Richland, WA, USA

43

44 Correspondence to: R.A. Zaveri (rahul.zaveri@pnnl.gov)

45

46

47

48 **Abstract.** Substantial uncertainties still exist in the scientific understanding of the possible
49 interactions between urban and natural (biogenic) emissions in the production and transformation
50 of atmospheric aerosol and the resulting impact on climate change. The U.S. Department of
51 Energy (DOE) Atmospheric Radiation Measurement (ARM) program’s Carbonaceous Aerosol and
52 Radiative Effects Study (CARES) carried out in June 2010 in Central Valley, California, was a
53 comprehensive effort designed to improve this understanding. The primary objective of the field
54 study was to investigate the evolution of secondary organic and black carbon aerosols and their
55 climate-related properties in the Sacramento urban plume as it was routinely transported into the
56 forested Sierra Nevada foothills area. Urban aerosols and trace gases experienced significant
57 physical and chemical transformations as they mixed with the reactive biogenic hydrocarbons
58 emitted from the forest. Two heavily-instrumented ground sites – one within the Sacramento
59 urban area and another about 40 km to the northeast in the foothills area – were set up to
60 characterize the evolution of meteorological variables, trace gases, aerosol precursors, aerosol
61 size, composition, and climate-related properties in freshly polluted and “aged” urban air. On
62 selected days, the DOE G-1 aircraft was deployed to make similar measurements upwind and
63 across the evolving Sacramento plume in the morning and again in the afternoon. The NASA B-200
64 aircraft, carrying remote sensing instruments, was also deployed to characterize the vertical and
65 horizontal distribution of aerosols and aerosol optical properties within and around the plume.
66 This overview provides: a) the scientific background and motivation for the study, b) the
67 operational and logistical information pertinent to the execution of the study, c) an overview of
68 key observations and initial findings from the aircraft and ground-based sampling platforms, and
69 d) a roadmap of planned data analyses and focused modeling efforts that will facilitate the
70 integration of new knowledge into improved representations of key aerosol processes and
71 properties in climate models.

72

73 **1. Introduction**

74 The strategy of the U.S. Department of Energy for improving the treatments of
75 atmospheric aerosol processes and properties in global climate models involves building up from
76 the microscale with observational validation at every step (Ghan and Schwartz, 2007). Particular
77 emphasis is placed on improving the scientific understanding of the possible interactions between
78 various urban (anthropogenic) and natural (biogenic) emissions in aerosol formation and evolution
79 of aerosol properties over a range of meteorological and chemical environments via an integrated
80 approach of field, laboratory, and modeling studies. The Carbonaceous Aerosols and Radiative
81 Effects (CARES) field campaign conducted in June 2010 in Sacramento, California, was a
82 comprehensive effort designed to contribute toward accomplishing this goal. This paper provides
83 an overview of the CARES project, and presents: a) the scientific background and motivation for
84 the field campaign, b) the operational and logistical information pertinent to the execution of the
85 campaign, c) an overview of key observations and initial findings from the aircraft and ground-
86 based sampling platforms, and d) a roadmap of planned data analyses and focused modeling
87 efforts that will facilitate the integration of new knowledge into improved representations of key
88 aerosol processes and properties in regional and global climate-chemistry models.

89 Field observations show that ambient aerosol can be composed of a wide variety of
90 compounds, including sulfate, nitrate, ammonium, sea salt, crustal species from soil dust, and
91 carbonaceous materials (e.g., Murphy et al., 1998; Seinfeld and Pandis, 1998). Primary

92 carbonaceous aerosols include black carbon (BC) particles mixed with varying amounts of organic
93 compounds that are directly emitted from fossil fuel combustion, cooking, industrial processes,
94 and biomass burning (agricultural burning and natural wildfires). Secondary carbonaceous
95 aerosols, more commonly referred to as secondary organic aerosols (SOA), are those formed in
96 the atmosphere via homogeneous nucleation, condensation, and heterogeneous reactions of
97 myriad gas-phase oxidation products from numerous volatile and semi-volatile organic compounds
98 of both anthropogenic and biogenic origins. Analyses of ambient aerosols in urban and rural areas
99 have shown that carbonaceous compounds may constitute up to 90% of the dry non-refractory
100 submicron particle mass (Kanakidou et al., 2005; Zhang et al., 2007).

101 Depending on their size and composition, aerosol particles can efficiently scatter and
102 absorb solar radiation and serve as cloud condensation nuclei (CCN), thereby affecting climate
103 (Forster et al., 2007). Significant progress has been made in the past two decades in representing
104 the various inorganic and carbonaceous species in state-of-the-art aerosol models that include
105 treatments for trace gas photochemistry, aerosol microphysics, aerosol thermodynamics, gas-
106 particle mass transfer, and heterogeneous chemistry (e.g., Wexler and Seinfeld, 1991; Jacobson,
107 2002; Zhang et al., 2004; Bauer et al., 2008; Zaveri et al., 2008). However, substantial uncertainties
108 still exist in our understanding of the evolution of organic and black carbon aerosols of both
109 anthropogenic and biogenic origins and the associated optical and CCN activation properties. The
110 CARES campaign was particularly motivated by three inter-related science questions:

- 111 (1) How do anthropogenic and biogenic precursors interact to form SOA?
- 112 (2) How rapidly does BC mix with other species (especially SOA), and what are the relative
113 contributions of condensation and coagulation to BC mixing state evolution?
- 114 (3) What are the effects of aerosol mixing state and organic (primary and secondary) species on
115 the associated optical and CCN activation properties?

116 During summer, the Sacramento urban plume transport is controlled by consistent,
117 thermally-driven upslope winds that draw polluted air to the northeast, into the Sierra Nevada
118 foothills area rich in biogenic emissions (Dillon et al., 2002). As a result, the anthropogenic BC,
119 primary organic aerosols (POA), SOA, and reactive trace gases from the Sacramento urban area
120 undergo significant photochemical ageing as they mix with biogenic SOA precursors such as
121 isoprene, monoterpenes, and related species. Some of these aged aerosols and trace gases could
122 be transported back into the urban area by nighttime downslope flows. In this way, the
123 Sacramento plume forms a natural chemical reactor useful for studying evolution of various
124 carbonaceous and related aerosols. The CARES campaign observational strategy was designed to
125 take advantage of this flow pattern by setting up two observation sites – one located within the
126 Sacramento urban area, referred to as the “T0 site,” and another located about 40 km to the
127 northeast in Cool, CA, a small town in the foothills area, referred to as the “T1 site” (Figure 1).
128 Comprehensive measurement suites deployed at the T0 and T1 sites provided continuous
129 information on the evolution of meteorological variables, trace gases, aerosol size, composition,
130 optical properties, solar radiation, and CCN activation properties during the entire campaign
131 period from June 2 through 28. The ground measurements were complemented by a similar set of
132 airborne measurements onboard the DOE Gulfstream-1 (G-1) aircraft, with flight plans involving
133 sampling upwind, within, and outside of the evolving Sacramento urban plume in the morning and
134 again in the afternoon. The NASA B-200 King Air aircraft, equipped with remote sensing

135 instruments, was also deployed to characterize the vertical and horizontal distribution of aerosol
136 optical properties and provide the vertical context for the G-1 and ground measurements.

137 The DOE CARES campaign overlapped temporally with the CalNex campaign in the Central
138 Valley and Southern California regions in May and June 2010. CalNex was sponsored by the
139 National Oceanic and Atmospheric Administration (NOAA) and the California Air Resources Board
140 (CARB), and it focused on the atmospheric chemistry and meteorological processes that affect air
141 quality and climate change issues both in California and nationally. The CalNex sampling platforms
142 included the NOAA WP-3D and Twin Otter aircraft, the NOAA R/V Atlantis, and two ground sites in
143 Southern California – one in Bakersfield and another in Los Angeles. The NOAA Twin Otter aircraft
144 moved its operation from Southern California to Sacramento (McClellan Airfield) to collaborate
145 with CARES from June 14–28. It carried a combination of downward-looking ozone/aerosol and
146 Doppler wind lidars and the scanning University of Colorado Airborne Multi-Axis DOAS (CU AMAX-
147 DOAS) system to investigate NO_x emission inventories and the 3-dimensional distribution and
148 transport processes of ozone and aerosols in the Central Valley.

149 The goal of this overview paper is to provide a coherent description of the project
150 objectives, a campaign summary, and a context for mature scientific results that will be reported
151 in future publications. We begin in section 2 with a brief review of previous research related to the
152 CARES science questions. In section 3, we describe the campaign venue, sampling platforms
153 (ground sites, aircraft), and the associated instruments and measurements. In section 4, we
154 present an overview of the key observations from the various airborne and ground-based
155 instruments. In section 5, we conclude with a summary of main initial findings and a roadmap for
156 future work.

157

158 **2. Brief Review of Previous Research Related to CARES Objectives**

159 **2.1 SOA Formation and Interactions between Anthropogenic and Biogenic Emissions**

160 Several field studies have shown that SOA forms rapidly in urban plumes, with most of the
161 SOA mass forming within the first 12 hours (Volkamer et al., 2006; Kleinman et al., 2007; de Gouw
162 et al., 2008). In contrast, modeling studies using Raoult's-Law-based schemes, parameterized using
163 laboratory chamber SOA yield data, significantly under-predict SOA formation in the ambient
164 urban atmosphere as well as in the upper troposphere (de Gouw et al., 2005; Heald et al., 2005;
165 Johnson et al., 2006; Volkamer et al., 2006). In a more recent study, de Gouw et al. (2009)
166 demonstrated that the growth of SOA at a suburban site in Mexico City could not be explained in
167 terms of the measured volatile organic compounds (VOCs) and their chamber-based particulate
168 mass yields and formation kinetics. Robinson et al. (2007) have suggested that some SOA mass at
169 urban to regional scales may be produced by volatilization of high molecular weight semi-volatile
170 and intermediate volatility organic compounds (SVOCs and IVOCs) from diesel exhaust primary
171 organic aerosols (POA), followed by condensation of their oxidation products. Recent modeling
172 efforts incorporating these and other previously missing SOA sources have begun to close the gap
173 between predicted and measured SOA levels (Dzepina et al., 2009; Hodzic et al., 2010; Slowik et
174 al., 2010; Lee-Taylor et al., 2011). However, comparisons of higher-order modeling endpoints to
175 measurements, such as organic aerosol (OA) oxygen-to-carbon ratio (O:C), OA volatility, and

176 ageing kinetics continue to indicate discrepancies in our understanding of SOA formation and
177 atmospheric ageing (Dzepina et al., 2009; Hodzic et al., 2010; Lee-Taylor et al., 2011).

178 In addition to these discrepancies, results from field studies suggest that anthropogenic
179 and biogenic emissions may somehow interact, resulting in increased overall yields of SOA. Weber
180 et al. (2007) found that fine-particle water soluble organic carbon (WSOC) in aged urban plumes in
181 the eastern United States was highly correlated with anthropogenic emissions from fossil fuel
182 combustion. However, the carbon isotope (^{14}C) analysis of the WSOC samples indicated that
183 roughly 70–80% of the carbon was of biogenic (modern) origin. Formation of organosulfate and
184 organic nitrate compounds as a result of interactions between anthropogenic pollutants (e.g.,
185 sulfate, NO_x) and biogenic hydrocarbons (e.g., isoprene) has been suggested to contribute to SOA
186 mass (Bruns et al., 2010; Farmer et al., 2010; Surratt et al., 2008, 2010; Zaveri et al., 2010a). In
187 contrast, hydrophobic POA formed from fossil fuel combustion may not readily absorb oxidized
188 (polar) biogenic hydrocarbons, as was previously assumed in many models, to enhance the overall
189 SOA yields (Song et al., 2007). Many laboratory studies have implicated heterogeneous chemistry
190 of semi-volatile and volatile organic vapors within aqueous inorganic aerosols as a potential route
191 for SOA formation from biogenic precursors (Jang et al., 2003; Kroll et al., 2005; Liggio et al., 2005,
192 2007; Limbeck et al., 2003). Also, accretion reactions, including aldol condensation, acid
193 dehydration, and gem-diol condensation can transform volatile organic species into oligomeric
194 products of low volatility (Gao et al., 2004; Jang et al., 2003; Kalberer et al., 2004; Tolocka et al.,
195 2004), potentially increasing SOA mass beyond that predicted by Raoult's Law alone. Recent
196 laboratory and field studies (including CARES) indicate that biogenic SOA particles may exist in
197 amorphous solid form, in which case Raoult's Law may not even be applicable to calculate gas-
198 particle partitioning of organic species on atmospherically relevant timescales (Vaden et al. 2011a;
199 Virtanen et al. 2010).

200 One of the key instruments deployed during this and many previous campaigns for
201 characterizing aerosol chemistry is the Aerodyne Aerosol Mass Spectrometer (AMS). The AMS
202 provides real-time, quantitative, and size-resolved data on submicron aerosol composition with a
203 time resolution of a few minutes or faster (Canagaratna et al., 2007). The HR-ToF-AMS, i.e., AMS
204 built with a high-resolution time-of-flight mass spectrometer, is further able to determine the
205 elemental ratios (e.g., oxygen-to-carbon, hydrogen-to-carbon, and nitrogen-to-carbon ratios) of
206 aerosol-phase organics (Aiken et al., 2008). In addition, multivariate statistical analysis of AMS
207 mass spectra is able to effectively determine organic aerosol factors representative of distinct
208 sources and atmospheric processes (Zhang et al., 2005; Ulbrich et al., 2009). Recent studies have
209 shown that comprehensive analyses of the mass spectra (i.e., chemical information) and temporal
210 variation profiles of the OA factors, in conjunction with measurements of aerosol physics, tracer
211 compounds, secondary aerosol precursors, and meteorological conditions, may reveal insights into
212 organic aerosol lifecycle processes, such as SOA formation and evolution (Zhang et al., 2011).

213 While significant progress has been made on this topic, the physical and chemical
214 interactions between anthropogenic and biogenic emissions leading to enhanced SOA formation
215 remain poorly understood and are not represented well in regional and global atmospheric
216 models. The CARES campaign observational strategy was designed to examine SOA formation at
217 the urban (source) and rural (receptor) sites when the Sacramento urban plume mixed with
218 biogenic emissions and when it did not. The comprehensive observations of precursor gases,

219 aerosol composition, size distribution, etc. at the two sites and aboard the G-1 aircraft will be
220 useful in constraining and evaluating SOA models designed to investigate the various possible
221 physical and chemical interactions between anthropogenic and biogenic SOA precursors.

222 **2.2 Evolution of Aerosol Mixing State**

223 Amongst all the different types of primary and secondary aerosols present in the
224 troposphere, BC (the refractory component of soot particles) is the most efficient and significant
225 particulate absorber of solar radiation, and plays an important role in both regional- and global-
226 scale climate forcing (Ramanathan et al., 2001; Jacobson, 2002, 2006; Bond, 2007; Levy et al.,
227 2008). Freshly emitted soot particles consist of fractal-like chain agglomerates of primary soot
228 spherules of 10 to 30 nm diameter (Wentzel et al., 2003). Ageing of soot particles by condensation
229 of hygroscopic species such as sulfate, nitrate, and SOA typically leads to a compaction of the
230 initially non-spherical chain agglomerate structures (Zhang et al., 2008; Tritscher et al., 2011),
231 although coated yet non-compacted BC particles have also been observed in urban plumes (Adachi
232 and Buseck, 2008). The mixing state and morphology of BC-containing particles is of particular
233 interest from a climate change perspective, as a non-light-absorbing coating on BC particles can
234 increase the ensemble averaged absorption cross section of the BC core by up to a factor of 2 due
235 to the focusing of light by the coating to the BC core (Lesins et al., 2002; Saathoff et al., 2003;
236 Schnaiter et al., 2005; Bond et al., 2006; Adachi et al., 2010; Cross et al., 2010). The coating on BC
237 particles also greatly increases their scattering cross sections, and the resulting single scattering
238 albedo (i.e., the ratio of scattering cross section to the sum of scattering and absorption cross
239 sections) is a function of the BC core size and the coating thickness. Hygroscopic coatings also
240 dramatically affect the CCN activation properties and atmospheric lifetime of BC particles (Cantrell
241 et al., 2001; Mochida et al., 2006; Kuwata et al., 2007; Medina et al., 2007; Cubison et al., 2008;
242 Furutani et al., 2008; Tritscher et al., 2011).

243 Field studies of BC mixing state evolution with single particle soot photometer (SP2,
244 Baumgardner et al., 2004; Schwarz et al., 2006; Moteki et al., 2007) reveal that BC particles tend to
245 be thinly coated in urban areas, and become “thickly” coated as the urban plume undergoes
246 photochemical ageing (Schwarz et al., 2008b; Subramanian et al., 2010). Several modeling studies
247 have examined the roles of condensation and coagulation in transforming externally-mixed BC
248 aerosols into internal mixtures (Fassi-Fihri et al., 1997; Jacobson, 2001, 2002; Jacobson et al., 1994;
249 Strom et al., 1992). Recently, Riemer et al. (2008) developed and applied a stochastic particle-
250 resolved aerosol box-model, PartMC-MOSAIC, to an idealized urban plume scenario based on Los
251 Angeles emissions, and the results indicate that BC particles have a wide range of mixing states
252 after 12 to 24 hours of processing. In a follow-on study, Zaveri et al. (2010b) found that aerosol
253 optical, hygroscopic, and cloud activation properties can be sensitive to the aerosol mixing state
254 even after 1 to 2 days of ageing. While field observations of evolution of BC mixing state are
255 qualitatively consistent with the results from particle-resolved modeling studies, a quantitative
256 validation of the detailed theoretical picture of aerosol mixing state evolution is necessary before
257 a reliable, computationally efficient mixing state framework can be developed for use in regional
258 and global climate models.

259 The SP2 instrument, when combined with the state-of-the-art single particle mass
260 spectrometer (SP-MS) instruments such as the single particle mass spectrometer (SPLAT II,
261 Zelenyuk et al., 2009), Particle Analysis by Laser Mass Spectrometry (PALMS, Murphy and

262 Thomson, 1997; Cziczo et al., 2006), and Aircraft-Aerosol Time-of-Flight Mass Spectrometer (A-
263 ATOFMS, Pratt et al., 2009; Pratt and Prather, 2010), can provide a more complete picture of the
264 different particle types and mixing states present in a population of aerosols. Recent advances in
265 single particle characterizations have made it possible to extend the analysis of data to determine
266 aerosol density, optical properties, shape, number concentrations, and size distributions (Murphy
267 et al., 2004; Moffet and Prather, 2005; Spencer et al., 2007; Zelenyuk et al., 2008; Zelenyuk and
268 Imre, 2009a; Vaden et al., 2011b) as well as combining data from other sources (or acquired while
269 within clouds) to determine composition as a function of hygroscopicity and CCN activity (Buzorius
270 et al. 2002; Herich et al., 2009; Kamphus et al., 2010; Zelenyuk et al., 2010; Hiranuma et al., 2011).
271 Furthermore, offline analyses of field-collected aerosol samples can provide additional details on
272 the composition, mixing state, and morphology of individual particles. These offline analytical
273 techniques range from scanning electron microscopy (SEM) and micro-spectroscopy
274 (STXM/NEXAFS) studies of individual particles (Laskin, 2010, Moffet et al., 2010a) to ultra-high
275 resolution mass spectrometry analysis of individual components in OA material (Nizkorodov et al.,
276 2011).

277 The CARES campaign included SP2 and SP-MS instruments as well as particle samplers (for
278 offline analyses) at both ground sites and onboard the G-1 to characterize the evolution of aerosol
279 mixing states in the Sacramento plume. The resulting composite picture of different particle types,
280 size, composition, and morphology will be useful for constraining the particle-resolved aerosol
281 model to evaluating the roles of condensation and coagulation in the evolution of aerosol mixing
282 state, with a focus on BC-containing particles.

283 **2.3 Aerosol Optical Properties**

284 As already discussed, the optical properties of freshly emitted and aged BC-containing
285 particles can differ significantly. The mass absorption cross-section (MAC) of uncoated, pure BC is
286 estimated to be $7.5 \pm 1.2 \text{ m}^2 \text{ g}^{-1}$ for radiation of wavelength $\lambda = 550 \text{ nm}$ (Bond and Bergstrom,
287 2006). Laboratory studies and the “core-shell” Mie theory calculations show that ensemble
288 average MAC of coated BC particles is amplified by up to a factor of ~ 2 (Schnaiter et al., 2005;
289 Bond et al., 2006; Bueno et al., 2011). In addition to BC, organic compounds such as humic-like
290 substances (HULIS) present in biomass burning aerosols also contribute to light absorption in the
291 atmosphere (Mukai and Ambe, 1986; Havers et al., 1998; Hoffer et al., 2006; Lukacs et al., 2007).
292 While light absorption by BC particles from diesel and motor vehicle soot typically displays an
293 inverse dependence on wavelength, light absorbing organic carbon (LAOC) typically displays much
294 stronger wavelength dependence. This increased absorption of light at wavelengths shorter than
295 600 nm causes the LAOC particles to appear brown (or yellow) (Bergstrom et al., 2002; Kirchstetter
296 et al., 2004; Andreae and Gelencsér, 2006; Barnard et al., 2008; Gyawali et al., 2012). Furthermore,
297 biomass burning particles composed of a small BC core ($\sim 50 \text{ nm}$) and a thick coating of LAOC
298 species may experience even larger enhancements in the absorption of light at wavelengths
299 shorter than 600 nm (Gyawali et al., 2009).

300 Recent field measurements also indicate secondary sources of LAOC particulate matter
301 that exhibit some chemical similarities to HULIS (Duarte et al., 2005; Marley et al., 2009; Hecobian
302 et al., 2010). While the exact mechanisms for secondary LAOC formation in the ambient
303 atmosphere are not fully understood, laboratory studies show that chromophores (components of
304 molecules that absorb light) can form via a variety of heterogeneous chemical reactions, including

305 ozonolysis of terpenes in the presence of ammonium ions (Bones et al., 2010) and isoprene
306 oxidation in the presence of acidic solutions (Limbeck et al., 2003). Carbonyls such as glyoxal and
307 methylglyoxal, produced from gas-phase photooxidation of many anthropogenic and biogenic
308 VOCs, can also lead to the formation of LAOC material via heterogeneous reactions in acidic
309 solutions (Noziere et al., 2007; Noziere and Esteve, 2005; Sareen et al., 2010), with amino acids (de
310 Haan et al., 2009a; Noziere et al., 2007), methyl amines (de Haan et al., 2009b), and ammonium
311 salts (Noziere et al., 2009; Sareen et al., 2010; Shapiro et al., 2009).

312 Thus, along with investigating SOA formation and aerosol mixing state evolution in the
313 Sacramento urban plume, a major objective of CARES was to observe the evolution of aerosol light
314 absorption and scattering in the near-UV and visible spectral regions as SOA of both anthropogenic
315 and biogenic origin condensed (or formed via heterogeneous reactions) on urban BC particles and
316 other, non-BC containing particles. Recent studies (Lack et al., 2008; Cappa et al., 2008) suggest
317 that absorption measurements from filter-based instruments such as the Particle/Soot Absorption
318 Photometer (PSAP) are suspect in the presence of OA. Photoacoustic and cavity ring-down
319 spectroscopy instruments that bypass the filter problems and are useful for determining
320 absorption coefficients in the visible region (Lewis et al., 2008; Radney et al., 2009). During CARES,
321 the spectral ranges of these instruments were extended down to $\lambda = 355$ nm to specifically
322 examine the absorption and scattering properties of OA.

323

324 **3. Design and Measurements**

325 **3.1 Campaign Venue and Geography**

326 The CARES campaign was based in Sacramento, CA, and took place from June 2nd through
327 28th, 2010. Sacramento is located in California's expansive Central Valley, and is the sixth most
328 populous city in California with a 2009 estimated population of 490,000. The seven-county
329 Sacramento Metropolitan Area is the largest in the Central Valley, with an estimated population of
330 2.46 million. The western half of Greater Sacramento is agricultural area while the eastern portion
331 of the region consists of the Sierra Nevada and its foothills, which are dominated by coniferous
332 and oak forests. Figure 2 shows the spatial distribution of total anthropogenic VOCs and biogenic
333 isoprene emissions in central California along with the locations of the T0 and T1 measurement
334 supersites. The anthropogenic VOC emissions are from California Air Resources Board (CARB)
335 emission inventory and the biogenic emissions are calculated online using MEGAN (Model of
336 Emissions of Gases and Aerosols from Nature; Guenther et al., 2006).

337 The climate in Sacramento and the valley area is characterized by damp to wet, cool
338 winters (October through April) and hot, dry summers (June through August). Summer heat is
339 often moderated by a sea breeze, locally known as the "delta breeze," which comes from the San
340 Francisco Bay through the Carquinez Strait (a narrow gap in the Coast Range) into the Sacramento-
341 San Joaquin River Delta. While transport processes over the entire Central Valley can be complex
342 (Bao et al., 2008), the local transport of the Sacramento urban plume during the summer is
343 controlled by consistent, thermally-driven upslope winds that draw polluted air northeast over oak
344 and pine trees in the Blodgett Forest area in the Sierra Nevada Mountains by late afternoon. The
345 Sacramento-Blodgett Forest corridor effectively serves as a mesoscale flow reactor where the daily
346 evolution of the Sacramento urban plume can be characterized as a Lagrangian air mass

347 transported from the urban core into the sparsely populated Sierra Nevada Mountains (Dillon et
348 al., 2002; Murphy et al., 2007). The CARES campaign observational strategy was designed to take
349 advantage of this natural flow pattern by setting up the two observation sites – one located within
350 the Sacramento urban area (site T0) and another located about 40 km to the northeast in Cool
351 (site T1), a small town in the forested foothills of the Sierra Nevada Mountains.

352 **3.2 Ground Sites and Instruments**

353 The T0 site (latitude: 38.6483, longitude: -121.3493, altitude: ~30 m MSL) was located in
354 the campus of American River College, about 14 km northeast of the Sacramento downtown area.
355 The T1 site (latitude: 38.8711, longitude: -121.0228, altitude: ~450 m MSL) was located on the
356 property of the Northside School in Cool, California, situated amidst a forested area rich in
357 biogenic emissions. The aged urban plume typically arrived at the T1 site around mid- to late-
358 afternoon when ozone and SOA from urban and biogenic precursors were near their peak
359 concentrations. The T0 and T1 ground sites thus characterized the diurnal evolution of
360 meteorological variables, trace gases, aerosol precursors, and aerosol composition and properties
361 in freshly polluted and aged urban air, respectively.

362 Nearly identical sets of measurements were made at both ground sites. Key measurements
363 included trace gases, aerosol precursor gases, size-resolved particle concentration and chemical
364 composition, particle physical properties (morphology, density, optical properties, hygroscopicity,
365 and CCN activation), solar radiation measurements, and meteorological measurements. The
366 measurement techniques, uncertainties, and time resolutions are summarized in Table 1. Two 40 X
367 10 ft trailers were set up at each site to house the instruments. The trailers were placed side by
368 side, with the aerosol stack (~8 m high) erected between them, and inlet lines going into both
369 trailers from the same stack. The trailer aerosol inlet system was based on the NOAA Global
370 Monitoring Division (GMD) Aerosol Observing System (AOS) tower and inlet design (Delene and
371 Ogren, 2002). The sample air was pulled through the stack and split into 2 components – an overall
372 stack flow of ~1000 L min⁻¹ and an aerosol flow (~120 L min⁻¹) through an internal concentric
373 stainless steel tube (~5 cm OD). The lower end of the 5-cm tube terminated in a 5-port manifold,
374 four of which were ¾ -in stainless tubes and the fifth a ½-in tube (central flow for temperature and
375 relative humidity measurements, as well as an auxiliary aerosol port for an Aerosol Particle Sizer,
376 APS). Flow through the system was provided by a stand-alone pump box external to the trailers.
377 Separate inlet lines were provided for trace gas and particle instruments. The trace gas inlet lines
378 were Teflon and the particle inlet lines were made of stainless steel. One of the ports was
379 connected to the AOS rack in one of the trailers. Two of the ports were used to provide aerosol
380 flow to each of the trailers, respectively. Each inlet line coming into the trailer was further split (by
381 a ¾-in “Y”) into lines that were wrapped around the internal walls of the trailer with ¼-in pick-off
382 ports strategically placed for the instrument configuration of each trailer. The return lines from
383 these sampling manifolds were also attached to the pump box. The AOS rack had special return
384 lines going to a carbon-vane pump and a diaphragm pump, respectively (also contained in the
385 pump box).

386 The Washington State University mobile laboratory was also deployed at the T0 site and
387 contained instruments for gas phase measurements. The inlet consisted of ½” PFA tubing that was
388 mounted to a 10-m telescoping meteorology tower attached to the trailer. A Vaisala WXT-510
389 weather station was mounted on the top of the meteorology tower. Approximately 0.5 m below

390 the weather station was the main inlet. Approximately 32 L min⁻¹ of air was pulled through the
391 inlet by a diaphragm pump with the flow measured by a TSI inline flow meter. Each instrument
392 inside the trailer subsampled from this main inlet line. The NO_{xy} instrument had a dedicated NO_y
393 converter inlet that was mounted about 1 m below the main inlet line.

394 The trace gas measurements included carbon monoxide (CO), nitric oxide (NO), total
395 reactive odd nitrogen species (NO_y), and ozone (O₃). Nitrogen dioxide (NO₂) and sulfur dioxide
396 (SO₂) analyzers were deployed at the T0 site (and on the G-1). Near surface NO₂ mixing ratios and
397 partial vertical column densities (VCD, integral over boundary layer height) were measured at T1
398 by the University of Colorado Ground Multi AXis DOAS instrument (CU GMAX-DOAS, Volkamer et
399 al., 2009). Proton-Transfer Reaction Mass Spectrometers (PTR-MS) were used to measure mixing
400 ratios of selected volatile organic compounds (VOC) of both anthropogenic and biogenic origin.
401 The PTR-MS at T0 was modified to also characterize the total concentration of semi-volatile long
402 chain alkanes (>C₁₀) and heavier monoaromatics associated with diesel exhaust vapor emissions.
403 The modification was to add a second inlet to the PTR-MS to allow in-situ thermal desorption
404 sampling from a dedicated heat traced inlet. PTR-MS sampling alternated between thermal
405 desorption analysis for diesel exhaust species and continuous de-humidified VOC sampling as
406 described in Erickson et al. (2012). In addition, a gas chromatograph ion trap mass spectrometer
407 (GC-ITMS) was used at T0 to measure selected C₆-C₁₀ VOCs to determine the abundance of SOA
408 precursors such as monoaromatics emitted in vehicle exhaust and monoterpene compounds
409 emitted from biogenic sources. Finally, near-surface concentrations of formaldehyde and glyoxal
410 and VCDs were measured by CU GMAX-DOAS at T1 (Sinreich et al., 2010).

411 Condensation particle counters (CPC) were used to measure total particle number
412 concentrations for particles larger than 10 nm diameter, and scanning mobility particle sizers
413 (SMPS) and aerosol particle sizers (APS) were used to measure particle size distributions from 10
414 to 20,000 nm. The APS was placed directly below the inlet (i.e., at the bottom of the vertical
415 column) where it drew air at a flow rate of 5 L min⁻¹ of the 120 total L min⁻¹. This placement
416 prevented any bends in the tubing and thus minimized any inertial impaction losses of coarse
417 particles. The “rain hat” on the top of the inlet stack is estimated to allow particles of at least
418 30,000 nm, although we did not actually characterize the inlet system on site for particle losses. An
419 Aerodyne High Resolution Time-of-Flight Aerosol Mass Spectrometer (HR-ToF-AMS), coupled to a
420 thermal denuder (Fierz et al., 2007), was deployed at each ground site to measure aerosol
421 composition and volatility distributions of submicron inorganic and organic aerosols. The HR-ToF-
422 AMS uses an aerodynamic lens to sample submicron particles (~50-1000 nm) into vacuum where
423 they are aerodynamically sized, thermally vaporized on a heated surface (~600 °C), and chemically
424 analyzed via 70 eV electron impact ionization time-of-flight mass spectrometry (Canagaratna et al.,
425 2007). Since aerosol species must be vaporized to be detected, the HR-ToF-AMS does not
426 measure refractory materials such as elemental carbon and dust particles. However, non-
427 refractory (NR) materials internally mixed with refractory substances can be determined by the
428 AMS and the presence of significant quantities of refractory particles can be detected via
429 comparison between aerosol size distributions (from the SMPS or the AMS) and total mass
430 detected, with appropriate assumptions about the particle density.

431 A Particle-Into-Liquid Sampler (PILS, Sooroshian et al., 2006) with an autosampler was
432 deployed at each site to collect vials every hour for offline analysis of water soluble aerosol

433 species. A PM₁ impactor (BMI) was used upstream of the PILS, CCN, and HR-ToF-AMS. Droplet
434 Measurement Technologies (DMT) Single Particle Soot Photometers (SP2, Stephens et al., 2003;
435 Schwarz et al., 2006) were used to measure single particle and ensemble black carbon mass
436 loadings along with information on the amount of the particles' coatings and cores. Single particle
437 mass spectrometers SPLAT II (Zelenyuk et al., 2009) and PALMS (Murphy and Thomson, 1997;
438 Cizco et al., 2006) were deployed at the T0 and T1 sites, respectively. A number of different
439 impactors were also deployed at both sites to collect aerosol samples for offline analysis of
440 particulate matter, ranging from electron microscopy and micro-spectroscopy studies of individual
441 particles (Laskin, 2010, Moffet et al., 2010a) to ultra high resolution mass spectrometry analysis of
442 individual components in OA material (Nizkorodov et al., 2011).

443 High-volume samplers (using brushless motors) equipped with slotted impactors were used
444 at the T1 site to obtain sub-micron samples for carbon isotopic characterization using quartz fiber
445 filters as described previously (Marley, et al., 2009). Another high-volume semi-volatile aerosol
446 sampler was deployed at the T0 site from June 2 to 15 and at the T1 site from June 16 to June 28
447 to collect particles of aerodynamic diameter $\leq 2.5 \mu\text{m}$ (PM_{2.5}) to study distribution of organic
448 reactive species, particularly acids and aldehydes with respect to total organic carbon. Samples
449 were collected for 12 hour periods, from 8 AM to 8 PM, and from 8 PM to 8 AM. Half of each filter
450 was spiked with recovery standards consisting of deuterated acids and aldehyde, derivatized using
451 pentafluorobenzyl hydroxyl amine (PFBHA) in methanol to stabilize aldehydes, and stored at -20 °C
452 in vials closed with Teflon stopper until the analysis. The other half of the filter was also stored at -
453 20 °C without any modifications.

454 Aerosol optical properties were measured at multiple wavelengths with several techniques,
455 including cavity ring-down spectroscopy for light extinction (CRDS, Smith and Atkinson, 2001;
456 Radney et al., 2009; Langridge et al., 2011), photoacoustic spectroscopy for light absorption (PAS,
457 Arnott et al., 1999; Lack et al., 2006), nephelometer for light scattering (Anderson et al., 1996), and
458 particle soot absorption photometer (PSAP, Ogren, 2010). These measurements provide the
459 absorption, scattering, and extinction coefficients as well as intensive (not dependent on aerosol
460 concentration) properties such as the single scattering albedo and Ångström exponents, and
461 depending on the particular operating procedures, their response to heating and changes in
462 relative humidity. Additionally, enhancements in light absorption by aged BC were directly
463 determined at the T0 site (from 15-29 June 2010) by measuring the absolute particulate
464 absorption with the UC Davis PAS before and after passing the particles through a thermodenuder
465 (TD). Similar measurements were also made onboard the R/V Atlantis from mid-May to mid-June
466 2010 as part of the CalNex campaign. The extent of evaporation of semi-volatile species (internally
467 mixed with BC) depends on the TD temperature and the specific composition of the particles.
468 Thus, if the coating on the BC particles causes an increase in the absorption, then thermally
469 denuded BC particles would absorb less light than non-denuded BC particles, and the absorption
470 enhancement (E_{abs}) can be calculated as the ratio of absorption measured before TD to that
471 measured after TD.

472 Radiation observations at the ground sites included broadband solar fluxes as well as Multi-
473 Filter Rotating Shadowband Radiometer (MFRSR, Harrison et al., 1994) measurements of
474 downwelling visible and near-IR solar irradiance at six discrete wavelengths, which provide
475 information needed to estimate aerosol optical depth and intensive properties. Partial column

476 integrals over boundary layer height of aerosol extinction were observed at three wavelengths
477 (360nm, 477nm, 630nm) as inferred from solar stray light column observations of oxygen dimer by
478 CU GMAX-DOAS (Volkamer et al., 2009; Sinreich et al., 2010).

479 Concentrations of CCN were measured at multiple supersaturations (0.07 to 0.5%) at both
480 sites using Droplet Measurement Technologies CCN Counters (Model 200-013 and 100-081). The
481 T1 site also included measurement of size-resolved CCN (SCCN) concentrations and variable
482 relative humidity nephelometry (commonly referred to as $f(\text{RH})$ measurement). Finally,
483 atmospheric state observations were made at the surface and aloft including wind speed and
484 direction, pressure, temperature, and relative humidity at both sites using several instruments.

485 **3.3 Aircraft Payloads**

486 The aircraft component of the CARES field campaign was based out of McClellan Airfield,
487 located about 4 km northwest of the T0 ground site. The trace gas and aerosol measurements
488 onboard the G-1 aircraft were similar to those deployed at the ground sites. The techniques,
489 uncertainties, and time resolutions of all the G-1 measurements are summarized in Table 2. Trace
490 gas measurements included CO (Kleinman et al., 2007), NO, NO₂, NO_y, O₃, and SO₂ (Springston et
491 al., 2005). An Ionicon high-sensitivity quadrupole PTR-MS was used to measure VOCs.
492 Condensation particle counters CPC-3025 and CPC-3010 (Sem et al., 2002) were deployed to
493 measure particle number concentrations for optical diameter (D_p) greater than 3 and 10 nm,
494 respectively. A combination of Fast Integrating Mobility Spectrometer (FIMS) (Kulkarni and Wang,
495 2006; Olfert et al., 2008), Ultra-High Sensitivity Aerosol Spectrometer-Airborne (UHSAS-A, Cai et
496 al., 2008), and the Cloud Aerosol Spectrometer (CAS) portion of the Cloud Aerosol Precipitation
497 Spectrometer (CAPS) probe (Baumgardner et al., 2001) were used to measure the particle size
498 distribution for mobility diameters (D_m) between 30 and 70 nm, and geometric diameters (D_g)
499 between 60 and 1000 nm, and 500 and 50,000 nm, respectively.

500 An Aerodyne HR-ToF-AMS was deployed to measure non-refractory aerosol components, a
501 DMT SP2 was used to measure BC number and mass concentrations, and the A-ATOFMS was used
502 to measure single-particle composition and mixing state. A PILS with an autosampler was deployed
503 to collect vials every 3 minutes for offline analysis of water soluble aerosol species. Automated
504 sampling of aerosol particles for microscopy and spectromicroscopy analyses was carried out using
505 a Time-Resolved Aerosol Collector (TRAC, Laskin et al., 2006). Aerosol optical properties (scattering
506 and absorption) at three wavelengths (405, 532, and 781 nm) were measured with an integrated
507 PAS/nephelometer instrument (DMT PASS3) (Flowers et al., 2010), a TSI 3563 nephelometer
508 (Anderson et al., 1996), and a Radiance Research PSAP (Ogren, 2010). The aerosol inlet on the G-1
509 allowed particles up to 5 μm aerodynamic diameter with close to 100% transmission efficiency.
510 Meteorological measurements included temperature, dew point, static pressure, and wind speed
511 and direction.

512 The NASA B-200 King Air (B-200) aircraft deployed a High Spectral Resolution Lidar (HSRL)
513 (Hair et al., 2008; Rogers et al., 2009) that measures aerosol backscatter ratio, backscatter and
514 extinction coefficients, and depolarization. It also carried a digital camera and the GISS Research
515 Scanning Polarimeter (RSP). The latter instrument measures total and polarized reflectances in
516 nine spectral bands across the visible and short-wave infrared portion of the electromagnetic
517 spectrum. From these measurements, column-averaged aerosol optical (e.g. optical depth) and
518 microphysical (e.g. refractive index and size distribution) parameters can be derived. The HSRL and

519 RSP have been deployed together in several major field campaigns since 2008, in an effort to
520 assess the potential of the synergistic exploitation of active and passive sensors in aerosol research
521 (Waquet et al., 2009; Knobelspiesse et al., 2011, Ottaviani et al., 2011). The uncertainties and time
522 resolutions of the B-200 measurements are summarized in Table 3.

523 As part of the CalNex field program, the NOAA Twin Otter aircraft moved its operation
524 from Southern California to Sacramento (McClellan Airfield) to collaborate with CARES from June
525 14–28. The NOAA Twin Otter was configured as a remote sensing platform carrying an
526 ozone/aerosol lidar, a Doppler wind lidar, a scanning DOAS system, and several radiometers. The
527 nadir-pointing Tunable Ozone Profiler for Aerosol and oZone (TOPAZ) lidar (Alvarez et al, 2011;
528 Langford et al., 2011) measured ozone and aerosol backscatter profiles below the aircraft while
529 the downward-looking, conically-scanned Doppler lidar (Pearson et al., 2009) provided
530 measurements of horizontal and vertical winds. The zenith-to-nadir scanning University of
531 Colorado Airborne Multi-AXis DOAS (CU AMAX-DOAS; Volkamer et al., 2009) instrument provided
532 reactive trace gas column observations (i.e., nitrogen dioxide, aerosol extinction, formaldehyde
533 and glyoxal) and the radiometers were used to measure surface albedo and surface skin
534 temperature. These remote sensors were complemented by in situ measurements of ozone mixing
535 ratio and temperature at flight level. The specifications for all instruments onboard the NOAA Twin
536 Otter are listed in Table 4. This unique instrument package enabled the characterization of the
537 horizontal and vertical structure of chemically and radiatively important trace gases and
538 particulates within the boundary layer and lower free troposphere. The primary objectives of the
539 NOAA Twin Otter deployment during CARES were the investigation of NO_x emission inventories,
540 and the mapping of the 3D distribution and transport processes of ozone and aerosols in the
541 Central Valley.

542 **3.4 Aircraft Flights**

543 The Weather Research and Forecasting (WRF) model (Grell et al., 2005) was run daily at
544 PNNL to provide 72-hour forecasts of tracer plumes, which were used to guide aircraft operations
545 and flight planning. The tracer plumes were based on CO emissions as well as meteorological
546 parameters, using a horizontal grid spacing of 4 km. The tracers were categorized into 20 sub-
547 regions based on anthropogenic emissions source region that could impact the CARES sampling
548 domain. Each forecast was made using the National Centers for Environmental Prediction's 00 UTC
549 North American Mesoscale analysis and corresponding forecasts as initial and boundary
550 conditions. Tracers were initialized with the previous day's forecasted tracer fields at 00 UTC. After
551 the WRF forecast was completed, graphics depicting tracer positions at the surface and at select
552 altitudes were generated automatically and made available on the CARES website
553 (<http://campaign.arm.gov/cares/forecast>). Figure 3 shows examples of tracer forecasts (at 16:00
554 PDT) under southwesterly and northwesterly flows, which respectively occurred for 15 and 9 days
555 out of the total 27 days from June 2 through 28. More detailed analysis of the CO tracer forecasts
556 and an analysis of them to categorize dominant transport scenarios during CARES can be found in
557 Fast et al. (2011).

558 Table 5 summarizes pertinent details of all the aircraft flights carried out during CARES. The
559 G-1 and B-200 aircraft performed a total of 22 (67.5 hours) and 23 (68 hours) research flights,
560 respectively, while the NOAA Twin Otter performed 17 flights (60 hours). The G-1 flight plans
561 included several patterns that were designed for a specific purpose or the given wind flow

562 condition. These patterns can be grouped into 3 basic types of missions: 1) morning or afternoon
563 flight plan designed to characterize the inflow from the Bay Area under southwesterly flow; 2)
564 morning and afternoon flight plans designed to characterize the evolution of the Sacramento
565 urban plume under southwesterly flow; 3) morning and afternoon flight plans designed to
566 characterize the evolution of the Sacramento urban plume under northwesterly flow. A late
567 morning flight was also conducted on June 27 to characterize isoprene emission flux over the
568 Sierra Nevada foothills region.

569 The B-200 flew at an altitude of approximately 7 km above ground, with most flights
570 coordinated with the G-1 to characterize the vertical and horizontal distribution of aerosol optical
571 properties and provide the vertical context for the G-1 and ground measurements. B-200 also
572 sampled over a larger area than the G-1 so that the G-1 observations could be interpreted within
573 the larger spatial context. Figure 4 shows the G-1 and B-200 flight tracks grouped according to the
574 type of the mission based on the expected transport scenario from WRF tracer forecast. Additional
575 missions flown by the G-1 and B-200, not shown here, included coordination with R/V Atlantis that
576 moved along the Sacramento Deep Water Channel from San Francisco Bay on June 3 and an
577 intercomparison flight with the NOAA WP-3D on June 18 in the San Joaquin Valley, from Fresno to
578 Bakersfield, CA.

579 While the NOAA Twin Otter flights were not closely coordinated with the G-1 or the B-200,
580 they were mostly in the same general area, with some flights extending over a larger domain
581 (Figure 4). The main objective was to sample the greater Sacramento area extensively, including
582 regular overpasses over the T1 site. The Twin Otter flew morning and afternoon missions, typically
583 lasting 3 – 4 hours. The morning flights were generally focused on investigating NO_x emissions
584 whereas the afternoon flights were designed to characterize ozone distribution and transport
585 downwind of Sacramento and the Bay Area. Flight altitudes varied from 600 to 5000 m MSL.
586 Another objective was the detection and characterization of pollution plumes transported from
587 Asia.

588

589 **4. Overview of Observations**

590 **4.1 Meteorological Context of CARES**

591 An overview of meteorology during CARES is provided by Fast et al. (2011). Here we give a
592 brief summary of the meteorological conditions that prevailed during the study period. During late
593 May the Central Valley experienced strong northwesterly flow and precipitation events, which
594 were likely due to the lingering effects of the moderate El Nino that occurred in early 2010. The
595 campaign thus began with cooler than normal temperatures and intermittent cloudiness through
596 June 6, followed by mostly sunny days for the remainder of the campaign. Figure 5 displays the
597 time series of wind direction, wind speed, temperature (T), and relative humidity (RH) at the T0
598 and T1 sites. The wind direction at both sites during the daytime was typically southwesterly to
599 westerly, favoring transport of the Sacramento urban plume to the T1 site area by late afternoon
600 or early evening. For the days labeled SW, the wind direction at T0 typically shifted to southerly by
601 18:00 PDT and to southeasterly by midnight, bringing relatively cleaner background air into the
602 urban area. In contrast, the wind direction at the T1 site typically experienced a reversal from
603 westerly (upslope) in the afternoon to easterly or northeasterly (downslope) at night, gradually

604 recirculating the air mass in the foothills region back into the valley in the residual layer by next
605 morning.

606 Days with synoptic southwesterly (SW) flow were generally favorable for transporting the
607 urban plume from Sacramento to the T1 site and vicinity. These days include: June 2-4, 6-9, 14-15,
608 17-19, and 23-28. The period from June 22 to 28 also experienced a steady buildup of aged
609 pollutants (particularly of organic aerosols as shown in section 4.3) due to more pronounced
610 recirculation of pollutants coupled with warmer temperatures toward the end of June. These
611 conditions resulted in the highest pollution days (June 25 through 28) at the end of the campaign.
612 Observations across the cleaner periods in the beginning of the campaign and the relatively more
613 polluted periods towards the end will thus provide an exceptional opportunity to examine aerosol
614 formation and evolution processes in the same region under a range of environmental conditions.

615 The SW wind pattern was interrupted by northwesterly (NW) flows three times during the
616 campaign: June 10-13, 16, and 20-21. During these NW flow events the Sacramento urban plume
617 was transported to the southeast along San Joaquin Valley, with relatively less mixing with
618 biogenic emissions when compared to SW flow events. Conversely, the biogenic emissions at and
619 around the T1 site were not significantly influenced by urban emissions during the NW flow
620 periods. This contrasting feature between the SW and NW flow events will be valuable in
621 investigating the role of anthropogenic-biogenic interactions in SOA formation from each source
622 type. The SW and NW flow periods are respectively identified with green and orange bars at the
623 top in Figure 5 (and subsequent figures showing time series of other variables), with semi-
624 transparent orange shading shown through all the plots for the NW flow periods.

625 The wind speeds at both T0 and T1 sites were generally small ($<4 \text{ m s}^{-1}$), with large values
626 occurring around noon and the smallest values around midnight. Diurnal variations in surface
627 temperatures at the T0 and T1 sites were similar, with highs between 25 and 35 °C occurring
628 around 18:00 PDT and lows between 10 and 15 °C occurring around 06:00 PDT. Due to the higher
629 elevation of the T1 site, the air was usually a few degrees (0 to 5 °C) cooler at T1 than at T0. The
630 last three days (June 26-28) were the warmest of the entire campaign, with temperatures at T0
631 reaching a maximum of 39 °C on June 27. Relative humidity displayed an opposite diurnal behavior
632 compared to temperature, with highs between 70 and 90% occurring at 06:00 PDT and lows of
633 about 20% occurring around 18:00 PDT.

634 **4.2 Trace Gases Observations**

635 Figure 6 shows comparisons of the time series of key trace gases (SO_2 , CO, NO_y , O_3 ,
636 toluene, and isoprene) observed at the T0 and T1 sites (SO_2 was not measured at T1). The plots
637 also show the same observations made on the G-1 aircraft when it flew over or within 2 km
638 (horizontally) of the T0 and T1 sites. Major sources SO_2 from oil refineries are located around the
639 Carquinez Strait and in San Francisco Air Basin (total SO_x emissions were about 14000 tons per
640 year for 2008). As a result, SO_2 was routinely transported to the Sacramento area and into the
641 Central Valley during SW flow and SO_2 mixing ratios of 1.5 to 2 ppbv were observed at T0 during
642 the daytime under these conditions. In contrast, SO_2 mixing ratios were nearly zero at the T0 site
643 at night or during NW flow. SO_2 mixing ratios measured onboard the G-1 during overpasses at T0
644 were typically equal to or up to 50% higher than those measured at the T0 site. Such differences
645 between ground and airborne observations could be expected as the SO_2 plumes were quite
646 narrow with sharp gradients.

647 As expected, the T0 urban site experienced significantly higher CO mixing ratios compared
648 to the T1 site in the rural foothills area. The minimum values at T0 were generally around 100
649 ppbv while they were as low as 80 ppbv at the T1 site. The highs at T0 were typically about 400
650 ppbv around noon, with occasional spikes reaching up to 1000 ppbv, likely due to local vehicular
651 traffic at the site. During the NW flow periods CO mixing ratios ranging from 400 to 1000 ppbv
652 were observed around midnight, likely due to transport of pollution from Interstate I-80 just 2
653 miles north of the T0 site. The highs at T1 were typically around 200 ppbv, which occurred in the
654 evening after 18:00 PDT when the diluted Sacramento plume was transported to the site under
655 SW winds. CO mixing ratios measured onboard the G-1 were in very good agreement with those
656 measured at the respective ground sites during the overpasses, except when the ground sites
657 experienced spikes due to local emissions. Diurnal behavior of NO_y mixing ratios at T0 was similar
658 to that of CO, with lows around 3 ppbv and highs ranging between 20 and 40 ppbv. During the NW
659 flow periods, NO_y mixing ratios ranged between 40 and 80 ppbv at midnight. The G-1 based NO_y
660 observations were also in good agreement with the ground sites.

661 The diurnal behavior of O₃ mixing ratios at the T0 and T1 sites were quite similar despite
662 the marked differences in the precursor trace gas composition and concentrations between the
663 two sites. The highs ranged between 60 and 80 ppbv, except for a peak of nearly 120 ppbv on June
664 28. The daily O₃ peaks at T0 typically occurred around 15:00 PDT while it was often delayed by ~3
665 hours at T1 on days when the urban plume was transported to the site during the SW flow periods.
666 The lows were typically around 20 ppbv at night and early morning at both sites throughout the
667 campaign, except during the NW flow periods when O₃ mixing ratios at T0 were nearly zero at
668 midnight due to titration by increased NO emissions reaching the site. O₃ measured aloft during
669 the G-1 overpasses were in excellent agreement with the respective ground sites.

670 The toluene time series is shown here as representative of primary urban VOC emissions.
671 As expected, its diurnal behavior at both sites was similar to that of CO. The highs at T0 ranged
672 from about 0.5 to 1 ppbv under SW flow and from 1.5 to 3 ppbv during NW flow conditions. In
673 contrast, the diurnal behavior of biogenic isoprene mixing ratios at both the sites followed that of
674 the surface temperatures. The highs ranged between 2 and 12 ppbv around 14:00 PDT while the
675 lows were nearly zero from midnight until dawn. Since the T1 site was located amidst biogenic
676 emissions, isoprene mixing ratios at T1 were generally about 0.5 to 3 ppbv higher than at T0. Also,
677 since both toluene and isoprene are primary species (emitted at the surface) and chemically
678 reactive, their mixing ratios observed aloft onboard the G-1 were typically about 20 to 50% lower
679 than at the ground sites during overpasses.

680 **4.3 Aerosol Observations**

681 **4.3.1 Aerosol Composition**

682 Figure 7 shows comparisons of time series of non-refractory aerosol species concentrations
683 observed with the HR-ToF-AMS instruments and black carbon mass observed with SP2 instruments
684 at the T0 and T1 sites. The plots also show the same observations made on the G-1 aircraft during
685 overpasses at the ground sites. Non-refractory aerosol composition at both the ground sites and
686 aboard the G-1 was dominated by organics, followed by sulfate, followed by nitrate and
687 ammonium, while chloride was negligibly small (not shown). Organic aerosol (OA) displayed a
688 diurnal cycle that was similar to that of O₃ at both sites. Comparisons of the estimated and
689 measured aerosol volumes for all three platforms are shown in Figure S1 (in Supplementary

690 Material). The estimated volumes were calculated from the AMS species and BC masses using
691 density of 1.75 g cm^{-3} for sulfate, nitrate, and ammonium, 1.53 g cm^{-3} for chloride, and 1.8 g cm^{-3}
692 for BC. While some day-to-day variations in the agreement between the estimated and measured
693 volumes were observed, especially for the G-1 on June 27 and 28, the overall agreements were
694 reasonably good with regression fit slopes of 0.91 for T0, 1.0 for T1 and 1.32 for G-1. Further
695 analysis is needed to determine the source of discrepancy in the G-1 data for June 27 and 28.

696 The peak OA mass concentrations at the T0 site ranged from 2 to $10 \mu\text{g m}^{-3}$ STP (i.e., at
697 standard temperature and pressure of 273.15 K and 1 atm, respectively) around 15:00 PDT when
698 O_3 mixing ratio also reached its daily maximum, which is consistent with SOA production from
699 photochemical oxidation of anthropogenic and biogenic VOCs. Minimum OA mass concentrations
700 of less than $0.5 \mu\text{g m}^{-3}$ STP typically occurred at or after midnight as the wind direction shifted to
701 southeasterly, which brought relatively cleaner background air into the urban area. While the OA
702 mass concentrations remained low during the daytime under NW flow conditions, they were often
703 found to peak around midnight at the T0 site. CO, NO_y , toluene, and BC concentrations also
704 peaked during these events, suggesting that this was primary OA emitted along I-80 (possibly from
705 the road work being performed at night during the campaign period) and brought to the site with
706 NW winds.

707 In contrast, OA mass concentration at the T1 site peaked at 18:00 PDT or later as the urban
708 plume was transported to the site during the SW flow periods. Note that the peak concentrations
709 at T1 were similar to or slightly higher than those observed at the T0 site even though the urban
710 plume experienced significant dilution as it was transported to the T1 site. During this transit the
711 urban plume mixed with increased biogenic emissions, which could have potentially contributed
712 the additional SOA mass that was observed at T1. Furthermore, the OA mass concentrations at the
713 T1 site often remained high at night and experienced a minimum of $\sim 2 \mu\text{g m}^{-3}$ STP in the morning.
714 Preliminary WRF simulation results suggest that the aged OA accumulating in the foothills area at
715 night were frequently recirculated to the Sacramento urban area within the residual layer the next
716 morning. Evidence of enriched organic aerosol mass in the residual layer is presented at the end of
717 this subsection. As mentioned earlier, the period from June 22nd to 28th experienced a steady
718 buildup of OA, with mass concentrations aloft reaching more than $25 \mu\text{g m}^{-3}$ STP at the end, due to
719 more pronounced recirculation of pollutants in the area coupled with possibly more SOA
720 formation from increased biogenic emissions due to warmer temperatures. The OA mass
721 concentrations observed onboard the G-1 were in good agreement with the ground sites values
722 during the overpasses, although they were a factor of 1.5 to 2.5 higher than observed at T1 during
723 the June 27 and 28 flights, likely due to strong spatial gradients of OA in the air in the vicinity of
724 that site on those days.

725 Sulfate (SO_4) mass concentrations typically ranged from 0 to $2 \mu\text{g m}^{-3}$ STP at both the
726 ground sites, with highs occurring early afternoon and lows around midnight. Ammonium (NH_4)
727 mass concentrations followed SO_4 , suggesting it was mostly in the form of ammonium sulfate or
728 bisulfate. In contrast, nitrate (NO_3) mass concentrations tended to peak later in the afternoon and
729 appeared to follow OA mass. SO_4 and NH_4 mass concentrations observed onboard the G-1 were in
730 fairly good agreement with the corresponding values at both the ground sites during the
731 overpasses, although the G-1 based SO_4 concentrations were sometimes found to be up to 50%

732 lower than the ground sites values. In comparison, NO₃ mass concentrations aloft were found to
733 be 50% higher than the ground sites values during overpasses.

734 Lastly, as expected, the T0 site experienced significantly higher BC mass concentrations
735 than the rural T1 site. The BC mass concentrations tended to follow the CO mixing ratios in time.
736 During the SW flow periods, the nighttime minimum values at both the sites were about 0.02 μg
737 m⁻³ STP or lower while the daytime maximum values were up to about 0.3 μg m⁻³ STP.
738 Interestingly, after June 22, the daily minimum BC mass concentrations ranged between 0.05 and
739 0.07 μg m⁻³ STP as there was increased recirculation of aged aerosols and a steady buildup of OA
740 mass concentrations in the region. The pre- and post-June 22 periods thus provide opportunities
741 to examine SOA formation and BC mixing state evolution in the same region under significantly
742 different ageing time scales. BC mass concentrations measured onboard the G-1 were in very good
743 agreement with those measured at the respective ground sites during the overpasses. As
744 discussed earlier, during the NW flow periods BC mass concentrations usually peaked at the T0 site
745 at midnight, with values ranging from 0.5 to 1 μg m⁻³ STP. These events provide opportunities to
746 characterize the size distribution, composition, mixing state, and the associated optical and CCN
747 activation properties of freshly emitted BC and OA particles. It is worth noting here that the SP2-
748 reported BC mass is dependent on the BC surrogate used to calibrate the incandescent signal from
749 SP2 (Laborde et al., 2012). The SP2 BC mass concentrations reported here for the T0, T1 and G-1
750 datasets are based on a calibration with Acheson Aquadag. Kondo et al. (2011) suggest that
751 fullerene soot may be a better proxy for urban BC; using a fullerene soot calibration could increase
752 our reported BC mass concentrations by approximately 67%.

753 Enhanced concentrations of aged organic aerosols, likely recirculated from the previous
754 day, were often observed in the residual layer (Stull, 1988) during the morning flights over the
755 Sacramento urban area. Figure 8 illustrates such an occurrence during the morning flight on June
756 15. The top panel shows a map with the G-1 flight tracks (solid lines) color coded by altitude. The
757 flight started at 08:56 PDT and consisted of several legs crisscrossing over the T0 site at ~360 and
758 ~660 m MSL altitudes. A spiral up to about 1300 m MSL was performed at about 09:30 PDT over a
759 location between the T0 and T1 sites. The G-1 then flew back and forth along the foothills from
760 11:00 PDT to 11:50 PDT, passing over the T1 site three times. The left portion of the bottom panel
761 shows the vertical profile of potential temperature obtained during the spiral. Based on the
762 inflections in this profile, the boundary layer height was estimated at about 590 m MSL and the
763 residual layer height was estimated to extend up to about 950 m MSL, which implies that the G-1
764 legs at 360 m MSL were within the boundary layer while the legs at 660 m MSL were in the
765 residual layer. The right portion of the bottom panel shows the G-1 flight altitude plotted against
766 local time, with the approximate locations of the T0 and T1 sites noted at the bottom of the plot
767 along the time axis. The plot also includes OA and NO₃ mass concentrations and NO_x/NO_y ratio
768 along the flight as a function of local time. NO_x/NO_y ratios were as high as 0.8 (right over the urban
769 center) within the boundary layer due to fresh emissions of NO_x in the morning. NO_x/NO_y ratios
770 were between 0.2 and 0.3 in the residual layer, which is indicative of aged pollution. Interestingly,
771 OA mass concentrations in the boundary layer were only about 2 μg m⁻³ STP while they were
772 about 6 μg m⁻³ STP in the aged residual layer. Similarly, NO₃ concentrations were about 0.5 μg m⁻³
773 STP in the boundary layer and about 1.5 μg m⁻³ STP in the residual layer.

774 The dotted white and pink lines in the top panel of Figure 8 represent forward trajectories
775 (computed using WRF forecasts) of air parcels that originated over the ocean (at surface level) off
776 the coast of San Francisco on June 14 at 19:00 PDT and June 15 at 02:00 PDT, respectively, such
777 that both air parcels arrived over the T0 site on June 15 at 10:00 PDT (i.e., during the time period
778 when G-1 was sampling in the area). The filled circles along the trajectories mark the locations of
779 the air parcels at hourly intervals. The air parcel along the pink trajectory was present within the
780 boundary layer and had passed over the Sacramento downtown area at about 08:00 PDT before
781 reaching T0 at 10:00 PDT. In contrast, the air parcel along the white trajectory was present in the
782 residual layer, and it had undergone a recirculation in the Sacramento Valley at night before
783 arriving over the T0 site at 10:00 PDT. These results are consistent with the aerosol composition
784 and NO_x/NO_y ratio observed in the boundary and residual layers as discussed above. Detailed
785 analyses of the chemical composition of the aerosols in the boundary and residual layers will be
786 conducted, and the potential contributions of the Bay Area and Sacramento emissions and the
787 ensuing daytime as well as nighttime chemistry in the formation of these aerosols will be
788 examined in subsequent studies.

789 **4.3.2 Aerosol Number Concentration and Size Distribution**

790 Figure 9 shows time series of aerosol number concentrations above 10 nm diameter
791 (denoted as $N_{>10}$) measured by the CPC-3010 instruments at the T0 and T1 sites along with the
792 CPC-3010 observations onboard the G-1 during the overpasses above these sites. These number
793 concentrations are put in context with the time series of SO_2 mixing ratio at the T0 site along with
794 the G-1 overpasses at T0. During SW flow periods, the T0 site experienced significant increases in
795 aerosol number concentrations from the nighttime lows of $\sim 5000 \text{ cm}^{-3}$ to about $35,000 \text{ cm}^{-3}$
796 (maximum of $45,000 \text{ cm}^{-3}$) between 08:00 and 13:00 PDT. These rapid increases in number
797 concentrations coincided with increases in SO_2 mixing ratios from below detection limit at night to
798 about 1-2 ppbv, suggesting that these particles were either nucleated at the T0 site via H_2SO_4
799 formation from SO_2 photooxidation, followed by growth to 10 nm and larger sizes, or they were
800 transported to the T0 site shortly after nucleating elsewhere, with continued growth during
801 transit. The increases in the number concentrations at the T1 site occurred almost simultaneously
802 with the T0 site or were sometimes delayed by 1-3 hours, and the daily maximum values reached
803 up to $20,000 \text{ cm}^{-3}$ (i.e., about a factor of 2 lower than at T0). Unfortunately, SO_2 was not measured
804 at the T1 site, so a similar comparison could not be made. As the SO_2 mixing ratios were small and
805 mostly below detection limit during the NW flow periods, the daytime increases in $N_{>10}$ values
806 were also significantly reduced at both the sites, with highs reaching less than 20,000 and 10,000
807 cm^{-3} at T0 and T1, respectively. The daily increases in $N_{>10}$ values at T0 and T1 were also greatly
808 reduced during the period from June 25 through 28 despite the high SO_2 mixing ratios observed
809 aboard the G-1 during overpasses. This reduction in $N_{>10}$ was likely due to the steady buildup of
810 aged aerosols of larger sizes, which effectively suppressed new particle formation and survival of
811 newly formed particles by providing large pre-existing surface area for H_2SO_4 condensation and
812 coagulation. The CPC-3010 number concentrations observed aboard the G-1 were in excellent
813 agreement with those measured at both ground sites during the overpasses through the entire
814 campaign.

815 The G-1 also carried a CPC-3025 which measured the total number concentrations of
816 particles larger than 3 nm, denoted as $N_{>3}$. Figure 10a shows a scatter plot of all the CPC-3025

817 versus CPC-3010 number concentrations observed aboard the G-1, with points colored by SO₂
818 mixing ratio that was also observed aboard the G-1. Note that values of both $N_{>3}$ and $N_{>10}$ were
819 generally found to increase with increasing SO₂ mixing ratios, and while the $N_{>3}/N_{>10}$ ratios
820 reached as high as 4, the high values generally did not coincide with enhanced SO₂ mixing ratios,
821 with some of the highest ratios corresponding to the lowest SO₂ mixing ratios. This result is
822 reasonable if the increased sulfate formation (and SOA) caused the large number of newly formed
823 particles to more rapidly grow larger than 10 nm. Figure 10b shows the same scatter plot, with
824 points colored by isoprene mixing ratio observed aboard the G-1. Points with isoprene mixing
825 ratios less than 1 ppbv were removed from the plot for clarity. Note that the highest $N_{>3}/N_{>10}$
826 ratios corresponded to the highest isoprene mixing ratios (and the lowest SO₂ mixing ratios),
827 suggesting that biogenic species may have played an important role (in the absence of appreciable
828 amounts of SO₂) in new particle formation and their initial growth to detectable sizes.

829 Figure 11 shows the time series of aerosol number size distributions at the T0 and T1 sites.
830 The plot for each site consists of size distribution data from the Scanning Mobility Particle Sizer
831 (SMPS) and Aerosol Particle Sizer (APS) instruments. The SMPS measures particle mobility
832 diameter (D_m) ranging from 0.01 to ~0.7 μm while the APS measures particle aerodynamic
833 diameter (D_a) ranging from 0.5 to 20 μm . Note that the size distribution data from both the
834 instruments are plotted using the same color scheme but with instrument-specific color scales that
835 differ by three orders of magnitudes. Comparison of the number size distributions measured by
836 the SMPS and APS in the overlap region is illustrated in Figure S2. Aerodynamic diameter from APS
837 was converted to geometric diameter by assuming a density of 2.25 g cm⁻³ for coarse mode
838 particles, which were found to be sea salt aerosols as discussed below. Number concentrations
839 from the two instruments appear to agree very well around 0.56 μm geometric diameter.

840 The APS data at both ground sites show the appearance of coarse mode particles on
841 several days (e.g., June 8, 14, 15, 18) when the wind direction was predominantly southwesterly.
842 As discussed in the previous section and shown in Figure 8 for June 15, WRF tracer forecast
843 simulations for these periods indicated appreciable transport of air from the Pacific Ocean into
844 Sacramento through the Carquinez Strait, suggesting that the coarse particles were composed of
845 sea salt, with some dust particles mixed into the air mass along the way. Indeed, the single particle
846 mass spectrometer data (discussed in the next subsection) support this hypothesis. The coarse
847 particles were mostly absent during the NW flow periods.

848 Consistent with the $N_{>10}$ time series shown previously in Figure 9, the SMPS data at both
849 ground sites show the appearance of ~10 nm diameter particles in large concentrations between
850 08:00 to 10:00 PDT. These particles were then found to rapidly grow until mid-afternoon, with the
851 particle composition data indicating this was largely due to condensation of secondary organics
852 and to a lesser extent due to condensation of sulfuric acid, nitric acid, and ammonia as shown
853 previously in Figure 7. More detailed analysis of carefully selected aerosol growth events should
854 provide valuable information for constraining aerosol chemistry and microphysics models to
855 evaluate and test SOA formation and BC ageing mechanisms under different conditions. Such
856 studies will be the subject of subsequent papers.

857 4.3.3 Aerosol Mixing State from SP-MS Instruments

858 A state-of-the-art single particle mass spectrometer (SP-MS) instrument was deployed at
859 each site and on the G-1 to obtain a more complete picture of the different particle types and

860 evolution of aerosol mixing states. SPLAT II was located at the T0 site to continuously measure the
861 size, composition, and density of individual particles with diameters between 50 to 2,000 nm. Each
862 day, SPLAT II characterized the size of ~7 million and composition of ~350,000 particles. It also
863 measured the aerosol size distribution and number concentrations of particles with diameters
864 larger than 85 nm (Vaden et al., 2011b,c). Simultaneous measurements of individual particle size,
865 density and composition were conducted for 121,000 individual particles. These measurements
866 were performed 2-3 times per day. In addition, SPLAT II was used to conduct the first
867 measurements of the kinetics of evaporation, phase, and morphology for size-selected ambient
868 SOA particles at ambient temperature (Vaden et al., 2011a).

869 PALMS was located at the T1 site to sample the relatively aged urban aerosols. PALMS
870 measured the same quantities as SPLAT II (i.e., particle size, composition, and density) on a single
871 particle basis. PALMS is not an automated instrument and therefore could not be run unattended.
872 Data were nonetheless acquired on most field days, with a particular emphasis on acquisition
873 during aircraft flights and afternoon periods when the Sacramento plume had transited to the T1
874 site. PALMS detected individual particles from ~125 to 3000 nm, although it is noteworthy that
875 transmission rate rapidly dropped at sizes lower than ~200 nm and greater than ~2000 nm. In total
876 ~100,000 particles were analyzed. Particular emphasis was placed on collecting PALMS data
877 simultaneously with f(RH) measurements to determine the effect of chemical composition on
878 particle hygroscopicity. An f(RH) measurement was also made at the T0 site during the second half
879 of the campaign.

880 An A-ATOFMS was flown on the G-1 to measure the size-resolved mixing state of individual
881 particles with diameters ranging from 70 to 1,200 nm. Dual polarity mass spectra were acquired
882 which allows for the identification of the source and the extent of atmospheric processing of the
883 particles. Over all flights, ~60,000 particles were analyzed. Due to particle transmission
884 efficiencies, most particles that were sampled ranged from 100 to 1,000 nm diameters, with a
885 mode centered at ~360 nm during most flights. These airborne measurements will be particularly
886 useful in understanding how the mixing state of different types of particles evolved in the
887 Sacramento urban plume as it was advected downwind.

888 Analysis of individual particle mass spectra at all locations indicates that at any given time
889 there were always a number of different types of particles with different compositions and size
890 distributions present. Figure 12 shows the average fraction of particles observed by A-ATOFMS for
891 each G-1 flight and 12-minute averaged fraction of particles observed by PALMS at the T1 site
892 classified into specific particle types. The vast majority of aerosol particles characterized during the
893 study were composed of oxygenated organics mixed with various amounts of sulfates: from
894 sulfate-dominated particles to those containing mostly organic species. In addition, fresh and
895 processed soot particles, biomass burning aerosol, amines, sea salt (both fresh and processed),
896 and a small number of mineral dust and other inorganic particles were present. The relatively
897 larger number fraction of sea salt particles observed aloft by the G-1 and at both ground sites on
898 June 8 and 15 is consistent with the APS size distribution data shown previously in Figure 11.

899 SPLAT II data for June 6 are shown in Figure 13 to illustrate a more detailed view of the
900 evolution of relative fractions of different particle types in a single day. Early in the morning
901 aerosol mass loadings and number concentrations were low and most particles were composed of
902 organics mixed with a significant fraction of sulfate. Larger particles containing a higher fraction of

903 sulfate were evident from the size-dependence of particle density. An example of size-dependent
904 particle density data measured by SPLAT II is illustrated in Figure 14. In general, density tended to
905 increase with particle size. For example, during the morning of June 6, 80 nm particles had a
906 density of $\sim 1.3 \text{ g cm}^{-3}$ while the density of 200 nm particles was $\sim 1.6 \text{ g cm}^{-3}$.

907 By around 09:00 PDT, the number concentrations of particles smaller than 14 nm
908 (measured by SMPS) began to increase, which indicated the growth of newly formed particles by
909 SOA condensation. As the day progressed and the emitted VOCs were oxidized, SOA-containing
910 particles increased in size, making it possible to characterize their size, composition, and density
911 with SPLAT II. By early afternoon aerosol composition was dominated by oxygenated organics
912 mixed with small amount of amines and sulfate ($\sim 10\%$ volume fraction), and the density of 80 nm
913 to 150 nm particles was $\sim 1.3 \text{ g cm}^{-3}$. These SOA-dominated particles were then used to study
914 evaporation kinetics at room temperature (Vaden et al. 2011a). The results of this study show that
915 evaporation of these size- and composition selected ambient organic particles was extremely slow
916 and size-independent, suggesting that the particles were in a quasi-solid state.

917 While the single particle data described above provide valuable information, they are
918 particularly useful when used in combination with other instruments. Three examples are
919 noteworthy and are listed among the analyses envisioned in the next subsection. First, BC
920 concentration, size and coating state can be obtained by the SP2 instrument which was deployed
921 at both ground sites and aboard the G-1 during CARES. The SP-MS data complement the SP2 data
922 by providing a qualitative measure of the chemical composition of the coating material internally
923 mixed with the BC. Second, biomass burning aerosol was episodically present during CARES,
924 particularly during the warmer and drier period later in the field study. Gas-phase acetonitrile can
925 be used as a tracer to detect the presence of biomass burning aerosol and the resulting
926 perturbations to SOA when biomass burning aerosol was present can be investigated. Finally, SP-
927 MS data can be used to determine periods of particular interest for off-line analyses of collected
928 and archived TRAC, DRUM, and SEM samples to further probe the chemical composition, mixing
929 state, and morphology of particles.

930 **4.3.4 BC Mixing State from SP2 Instruments**

931 The single particle soot photometer (SP2) measures BC via laser-induced incandescence
932 and can obtain some useful information about particle size, relative coating thickness and mixing-
933 state based on the scattering signal from the both BC and non-BC containing particles (Stephens et
934 al., 2003, Schwarz et al., 2006; Subramanian et al, 2010). The heart of the SP2 is the laser-induced
935 (1064 nm, Nd:YAG) incandescence signal from BC. Incorporation of narrowband and broadband
936 filters enables the SP2 to be highly selective towards BC. The incandescence intensity is linearly
937 proportional to the BC: more mass leads to stronger incandescence. In addition to providing data
938 on the BC number density and mass concentration, since the SP2 is inherently a particle-by-
939 particle instrument, individual incandescence signals can be collected and binned to provide a
940 mass equivalent diameter (MED) size distribution ($dN_{BC}/d\text{Log}D_{MED}$) and mass distribution,
941 ($dM_{BC}/d\text{Log}D_{MED}$). The nominal BC mass detection range for the SP2 units deployed at CARES was
942 from $\sim 0.2 \text{ fg/particle}$ to $\sim 250 \text{ fg/particle}$ – 60 nm to 650 nm MED, for an assumed particle density
943 of 1.9 g cm^{-3} .

944 The SP2 is also outfitted with a scattering channel that, when combined with the
945 incandescence signal, allows the BC mixing-state to be probed (Moteki and Kondo 2008;

946 Subramanian et al., 2010). The cornerstone of this technique is that a fully coated BC particle must
947 first boil-off its coating *before* the BC will incandesce. The time necessary to vaporize this coating is
948 referred to as the lagtime ($\Delta\tau$), which is the temporal lag of the incandescence signal relative to
949 the scattering signal – the larger the lagtime the thicker the coating, although the relationship
950 between these two quantities is complex. By plotting the observed lagtimes versus the BC MED, a
951 semi-quantitative picture of the BC mixing-state can be rendered enabling the evolution of the
952 mixing-state to be directly probed. As advocated by Moteki and Kondo (2008) and more recently
953 by Subramanian et al., (2010), due to instrument limitations, a demarcation between “thinly”
954 coated (nascent) BC and “thickly” coated BC is strongly encouraged when using the lagtime
955 analysis. For the current study, this dividing line between thinly and thickly coated BC particles is
956 1.25 μsec ; that is, $\Delta\tau > 1.25 \mu\text{sec}$ indicates the presence of thickly coated BC particles while shorter
957 lagtimes designate the presence of thinly coated BC particles. In addition to the lagtime analysis,
958 the complementary analysis technique of estimating the coating thickness through examination of
959 the difference between calculated BC core mass equivalent diameter and an estimate of the
960 coated BC particle diameter determined from the scattering signal amplitude, was also conducted
961 (Gao et al., 2007; Moteki and Kondo 2006).

962 An example of the incandescence-scattering lagtime analysis as a function of BC mass
963 equivalent diameter is shown in Figure 15 for the June 28th morning and afternoon flights.
964 Contours are normalized number concentrations in an effort to highlight the differences between
965 the two flights (red = 0.9/blue = 0.2). Using the linear relationship between lagtime and coating
966 thickness shown by Subramanian et al., (2010), the right axis is the estimated coating thickness
967 outlined above. It is important to note that an SP2-based analysis of the BC mixing state requires
968 usable signals from both the scattering and incandescence channels. Despite the fact that the
969 incandescence signal can probe BC mass equivalent diameter ranging from nominally 60 - 600 nm,
970 the limited range of the scattering channel (~175 nm to 350 nm) limits this analysis to only those
971 coated BC particles that fall into the latter range. Examination of the morning flight lagtime data
972 (top trace in Figure 15) reveals that the observed distribution is dominated by thinly coated BC
973 particles while the June 28 afternoon flight reveals an increase in the number of thickly coated BC
974 cores, consistent with BC ageing. Preliminary analysis of the BC mass distributions for the two
975 flights reveal that the mean mass diameter (MMD) increases from 137 (± 1.2) with a geometric
976 standard deviation (GSD) of 1.4 (± 0.03) for the morning flight to 142 (± 1.1) nm with a (GSD) of 1.4
977 (± 0.03), where the error is 1- σ . Whether this MMD shift (or alternatively, loss of smaller diameter,
978 thickly coated BC particles) is due to instrument limitation(s) or advection will be the subject of the
979 ensuing analysis on this G-1 dataset. Additional lines of analysis will include better quantification
980 of the BC mixing-state (coating thickness) by correcting the estimated coating thicknesses for host
981 material loss due to heat transfer from the light absorbing core (Gao et al., 2007; Moteki and
982 Kondo 2006) and estimating the ratio of the coating mass/BC mass as well as examining the light
983 absorbing properties in the core-shell limit. Towards this end, preliminary analysis indicates an
984 increase in the coating mass to BC ratio between the morning and afternoon flights.

985 **4.3.5 Offline Analyses of Particle Samples**

986 Comprehensive analyses of particle samples collected at T0 and T1 ground sites and
987 onboard the G-1 can be performed using an array of modern, state-of-the-art analytical
988 techniques available at two DOE scientific user facilities (Environmental Molecular Sciences

989 Laboratory at Pacific Northwest National Laboratory and Advanced Light Source at Lawrence
990 Berkeley National Laboratory) and at Michigan Technological University (Applied Chemical and
991 Morphological Analysis Laboratory). The primary techniques for analysis are Computer Controlled
992 Scanning Electron Microscopy with Energy Dispersed analysis of X-rays (CCSEM/EDX) (Li et al.,
993 2003; Laskin et al., 2006) and Scanning Transmission X-ray Microscopy with Near Edge X-ray
994 Absorption Fine Structure spectroscopy (STXM/NEXAFS) (Moffet et al., 2010b). These techniques
995 provide information on particle morphology, elemental composition, mixing states, and
996 partitioning of oxidation states, which yield deeper insights into atmospheric ageing of different
997 types of aerosols. Although particle samples were collected continuously at the ground sites and
998 on many G-1 flights, only a small subset will be chosen for detailed analysis. The periods of interest
999 are chosen based on observations from other collocated instruments and meteorological
1000 considerations.

1001 Figure 16 shows examples of SEM images of aerosol particles collected at the T0 site. The
1002 low magnification image (a) includes (i) a large dust particle, (ii) relatively small spherical particles,
1003 (iii) fractal-like soot particles, and (iv) an irregularly shaped particle. Image (b) shows a close-up
1004 view of a fractal-like BC particle with an open structure (i) without substantial coating and (ii) with
1005 coating. Since SEM imaging is operated under vacuum, volatile aerosol components typically
1006 evaporate from the filter. An example of an evaporated liquid particle is visible in the lower right
1007 corner of image (b). Image (c) shows a compacted, internally mixed BC particle, and image (d)
1008 shows a particle with BC inclusion. These micrographs highlight the morphological complexities of
1009 freshly emitted and aged BC particles as well as of the underlying ageing mechanisms that produce
1010 the variation in coating thickness. From these images it is also evident that coated and compacted
1011 internally mixed BC monomers are larger in size and have higher polydispersity than monomer
1012 distributions in nascent BC. For example, the geometric mean diameter for thickly coated BC is 68
1013 nm with a standard deviation of 10 nm (Figure 16b-(ii)), whereas for compacted internally mixed
1014 soot the geometric mean diameter of the monomers is 42.1 nm and the standard deviation is 10.2
1015 nm (Figure 16-c), versus a geometric mean diameter of 39.8 nm and a standard deviation of 5.6
1016 nm for nascent soot (Figure 16b-(i)). The polydispersity in various mixing states affects the fractal
1017 and optical properties of soot. Future studies will focus on the analysis of the aerosol mixing state
1018 and association with optical properties, the diurnal variation of fractal properties of soot, the
1019 relation between particle morphology type and optical properties, and the elemental composition
1020 of single particles using EDX analysis.

1021 In addition to information on carbonaceous particle ageing, composition, organic coatings,
1022 and size resolved mixing state, spectromicroscopy studies can also provide information on sulfur
1023 bonding (Hopkins et al., 2008), organic coatings on sea salt (Pratt et al., 2010), and Fe oxidation
1024 states (Moffet et al., 2012). Figure 17 shows characteristic SEM images and STXM/NEXAFS
1025 chemical maps for particles collected during the photochemical aerosol buildup period at the end
1026 of the field campaign (June 27-29). Particles sampled on the morning of June 27 at T0 were
1027 primarily composed of inorganic cores surrounded by varying amounts of organics, whereas
1028 particles sampled at T1 on the afternoon of June 28 were primarily composed of a homogenous
1029 inorganic/organic mixed phase. This evidence of photochemical aging is analogous to observations
1030 in Mexico City during the MILAGRO campaign (Moffet et al., 2010c).

1031 CCSEM/EDX and STXM/NEXAFS analyses of TRAC-collected particles onboard the G-1 on
1032 June 15 (a strong SW flow event) showed the presence of sea salt particles over Sacramento.
1033 Forward trajectories simulated by WRF (Fast et al., 2012) coupled with Lagrangian particle
1034 dispersion model (Doran et al., 2008) analysis confirmed that the sea salt particles were
1035 transported from the Pacific Ocean/Bay Area. Interestingly, these particles were found to be
1036 internally mixed with organics, which were likely SOA species formed in these particles during the
1037 transit from the Bay Area. Surprisingly, these particles had experienced substantial chloride
1038 depletion that could not be explained by the known reactivity of sea salt with nitric and sulfuric
1039 acids. This study, recently published by Laskin et al. (2012), is the first field evidence that SOA,
1040 consisting of weak organic acids, may effectively react with sea salt particles and displace HCl gas,
1041 leaving behind particles depleted in chloride and enriched in the corresponding organic salts.

1042 The microscopy and spectromicroscopy methods discussed above help visualize particle
1043 morphology and internal structure at the nanometer scale (Laskin, 2010; Moffet et al., 2010a) and
1044 provide valuable chemical information on elemental composition (SEM/EDX) and organic group
1045 functionalities present in particles (STXM/NEXAFS). High resolution Nanospray Desorption
1046 Electrospray Ionization (Nano-DESI) mass spectrometry on field-collected particles can provide
1047 additional detailed information on the molecular structures of organic aerosol species, but this
1048 method acquires integrated signal from an ensemble of particles and therefore eliminates
1049 knowledge of individual particle composition (Roach et al., 2010). Thus, analyses of the various
1050 particle samples collected during CARES will include complementary analytical methods that
1051 provide comprehensive information ranging from microscopic details of individual particles to
1052 advanced molecular characterization of complex molecules comprising particulate matter.

1053 Other types of offline chemical and radio isotopic analyses of ambient aerosol require large
1054 amounts of samples, which were obtained during CARES using several high-volume samplers.
1055 Carbon levels in the submicron particle samples taken at the T1 site with high-volume samplers
1056 were found to be quite low, and visual examination indicated little BC present for most of the
1057 study. This result is qualitatively consistent with the measurements of BC mass by the SP2 at the
1058 T1 site. Carbon-14 analysis of four samples collected over 12 and 24 hour periods at the beginning
1059 and end of the CARES campaign show that 74 ± 0.6 % of the carbon was modern, suggesting that
1060 there was a significant biogenic component in the carbonaceous aerosols. Furthermore, stable
1061 carbon isotopic content ($\delta^{13}\text{C}$) for these samples was found to be -27.5 ± 3.5 ‰ relative to the Pee
1062 Dee Belemnite standard. This is equal to the global average $\delta^{13}\text{C}$ for C3 plants such as Ponderosa
1063 Pines, which dominate the region (Ehleringer and Monson, 1993; Cerling and Harris, 1999). The
1064 combined data indicate that a significant amount of the carbonaceous aerosols at this site were
1065 from secondary organic carbonaceous aerosols, likely produced from oxidation of isoprene,
1066 monoterpenes, and sesquiterpenes by ozone and OH radicals. Further work on these quartz filter
1067 samples is planned, including examination of natural radionuclides (^7Be and ^{210}Pb) as well as use of
1068 integrating sphere methods to examine the UV-Visible absorption of the terpene-dominated SOA
1069 (Gaffney, et al, 2004; Marley, et al., 2009).

1070 Another high-volume PM_{2.5} sampler was deployed at the T0 site from June 2 to 15 and at
1071 the T1 site from June 16 to June 28. Detailed chemical analysis of these samples is also planned,
1072 with a focus on studying the distribution of organic acids and aldehydes with respect to total
1073 organic carbon (Jaoui et al., 2004).

1074 **4.4 Optical Properties and Radiation Observations**

1075 **4.4.1 In situ Aerosol Optical Properties**

1076 In situ aerosol optical properties were measured at multiple wavelengths at each site with
1077 several instruments, including nephelometer, PSAP, PAS, and CRDS. The flow to the nephelometer
1078 and PSAP instruments at each site was subjected to alternating size cutoffs of 1 and 10 μm
1079 aerodynamic diameters for 6 minutes each; the difference between the two gives the scattering
1080 and absorption by super-micron particles. Such variable size cutoffs were not applied to flows on
1081 other instruments. Nephelometer, PSAP, and PAS instruments were also deployed aboard the G-1.
1082 As mentioned earlier, the aerosol inlet on the G-1 allowed transmission of particles up to 5 μm
1083 aerodynamic diameters, and no additional cutoffs were applied to the flows to the optical
1084 instruments. In this report we limit the discussion to the nephelometer, PSAP, and PAS
1085 observations at green wavelength to illustrate the behavior and consistency of the scattering and
1086 absorption coefficients observed on the three different platforms through the entire campaign.
1087 Detailed analyses of the optical properties at different wavelengths from each instrument and a
1088 comparison of observations from all three instruments will be presented in separate papers.

1089 Figure 18 shows the time series of scattering coefficients (B_{sp}) measured at $\lambda = 550 \text{ nm}$ by
1090 the nephelometers along with the surface area size distribution derived from APS measurements
1091 at both sites. Also shown are the scattering coefficients observed aboard the G-1 during
1092 overpasses at each site. Coarse mode particles were largely absent at both sites during the first
1093 week of June and later again during the NW flow periods. During these periods, scattering
1094 coefficients for the 1 μm cutoff channel were rather low and ranged between 2 and 15 Mm^{-1} while
1095 scattering coefficients for the 10 μm cutoff channel were only about 2 to 5 Mm^{-1} higher. On days
1096 when the surface area size distributions indicate increased presence of coarse mode particles,
1097 scattering coefficients for the 10 μm cutoff channels reached as high as 40 to 75 Mm^{-1} and 20 to
1098 50 Mm^{-1} at the T0 and T1 sites, respectively, and were about 2 to 4 times higher than the values
1099 for the 1 μm cutoff channel at each site. Scattering for both channels at both sites shows a steady
1100 increase after June 22, which is consistent with the steady buildup of submicron size aged aerosols
1101 in the region as discussed previously. During this period, the increase in the scattering in the 10
1102 μm channel was largely driven by the increase in scattering in the 1 μm channel. According to the
1103 surface area size distribution data at both sites, about 95% of the total surface area was present
1104 below 5 μm aerodynamic diameter when a significant coarse mode was present. Consequently,
1105 the scattering coefficients observed aboard the G-1 were in very good agreement with or only
1106 slightly smaller than the 10 μm cutoff values at both the ground sites during the overpasses,
1107 through all periods of low and high concentrations of coarse mode particles.

1108 Figure 19 shows time series of absorption coefficients (B_{ap}) measured by PSAP ($D_a < 1 \mu\text{m}$)
1109 and PAS instruments at $\lambda = 532 \text{ nm}$ at both the sites. Also shown are absorption coefficients
1110 measured with the PSAP ($\lambda = 522 \text{ nm}$) aboard the G-1 during overpasses at each site. The ground
1111 sites PSAP data are 1-min averages, the G-1 PSAP data are 10-sec averages, and the PAS data are
1112 30-min averages. Through the entire campaign, PSAP absorption coefficients for the 10 μm cutoff
1113 channel (not shown) were nearly identical to the 1 μm cutoff values, indicating that the coarse
1114 mode particles were largely non-absorbing at $\lambda = 532 \text{ nm}$. The ground sites PSAP and PAS
1115 absorption coefficients are in good agreement. The PSAP absorption coefficients observed aboard

1116 the G-1 are also in very good agreement with the PSAP and PAS based values at both ground sites
1117 during the overpasses.

1118 As described in section 3.2, BC absorption enhancement (E_{abs}) was directly determined at
1119 the T0 site (and onboard R/V Atlantis) as the ratio of the absolute particulate absorption measured
1120 with a PAS before passing through a thermodenuder to that measured after passing through the
1121 thermodenuder. Surprisingly, the observed E_{abs} was small, about 6% on average at 532 nm, and
1122 increased weakly with photochemical ageing. In sharp contrast, the E_{abs} predicted from
1123 observationally-constrained core-shell Mie theory calculations for the R/V Atlantis data was nearly
1124 100%. A slightly larger E_{abs} at 405 nm was observed, which suggests absorption by LAOC species at
1125 shorter wavelengths. This work, recently published by Cappa et al. (2012), is the first direct
1126 determination of BC absorption enhancement in ambient atmospheric aerosol samples.

1127 **4.4.2 Ground-based Remote Sensing Observations**

1128 A Multi-Filter Rotating Shadowband Radiometer (MFRSR) was deployed at each ground site
1129 to measure the total all-sky surface downwelling irradiance, and its diffuse and direct components.
1130 These were measured at six narrowband (10 nm, FWHM) wavelengths centered at 415, 500, 615,
1131 673, 870, and 940 nm (visible and near-IR spectral region) with 20-sec temporal resolution. The
1132 measured irradiances were used to obtain column aerosol microphysical and optical properties,
1133 such as aerosol optical depth (AOD), single scattering albedo (SSA), and asymmetry parameter, g .
1134 The high-temporal resolution MFRSR observations at the two sites provided the diurnal, day-to-
1135 day, and site-by-site variations of AOD (Figure 20). For example, the AOD values (at $\lambda = 500$ nm)
1136 were observed to range from about 0.025 (which represents very clean air) at the start of the
1137 campaign to about 0.12 towards the end of the campaign. Note that there were several cloudy-sky
1138 periods when AOD values are not available.

1139 In addition to the AOD values, the MFRSR observations were used to retrieve aerosol
1140 microphysical (e.g., size distribution, including fine and coarse size modes) and the intensive
1141 optical properties (SSA and g) using spectrally resolved direct and diffuse irradiances (Kassianov et
1142 al., 2007). The original version of this technique has been developed for clear sky conditions. Its
1143 updated version (Kassianov et al., 2011) extends the clear-sky aerosol retrievals to partly cloudy
1144 conditions, so that aerosol properties can be determined for some cloudy sky conditions. Similar
1145 to the AOD, the aerosol size distributions and intensive properties have significant variations over
1146 the course of the campaign. To illustrate this we show temporal changes in the aerosol size
1147 distribution (a bimodal distribution consisting of fine and coarse modes) retrieved at the two sites
1148 (Figure 21). It is notable that the coarse mode was substantial for several time periods (e.g., during
1149 June 16). In general, the existence of a large coarse mode in the column, as retrieved from the
1150 MFRSR measurements, is consistent with measurements of the coarse mode made by the APS
1151 instruments at the T0 and T1 sites (shown previously in Figure 18).

1152 **4.4.3 Airborne Remote Sensing Observations**

1153 Consistent with the ground sites and G-1 observations, the HSRL measurements aboard the
1154 B-200 showed that aerosol extinction and AOD (532 nm) were generally quite low during CARES;
1155 average AOD values (for the layer between 0.1 to 7 km) in and around the Sacramento area were
1156 generally between 0.05 and 0.1. Smaller values were found earlier during the mission (e.g. June 3
1157 and 6); larger (>0.1) AOD values were measured later during the mission (e.g. June 28). The HSRL

1158 measurements also showed that much (30-70%) of the AOD was above the top of the planetary
1159 boundary layer (PBL).

1160 The HSRL measurements of aerosol intensive parameters and aerosol optical depth have
1161 also been used to identify aerosol types and apportion aerosol optical thickness to the various
1162 aerosol types (Burton et al., 2011). Eight distinct types with different aerosol intensive properties
1163 were identified. The identification of these types were guided by the analyses of Cattrall et al.
1164 (2005) and Müller et al. (2007) that provide values of a set of lidar-observed aerosol intensive
1165 parameters corresponding to various aerosol types. The HSRL aerosol classification results were
1166 used to identify smoke aerosols during the ARCTAS mission (Warneke et al., 2010) and urban
1167 aerosols during the MILAGRO mission (Molina et al., 2010).

1168 The HSRL data indicate significant variability in the vertical and horizontal distributions of
1169 aerosols during CARES. An example of such aerosol variability is illustrated in Figure 22 which
1170 shows HSRL measurements acquired between 17:45 UT and 18:12 UT on June 19 when the B200
1171 flew from the Sacramento region northeast over the mountains. Aerosol backscatter and AOD
1172 decreased as the aircraft flew northeast along the track. The variability of the aerosol intensive
1173 parameters (i.e. aerosol depolarization, depolarization spectral ratio, and backscatter wavelength
1174 dependence) is indicative of changes in aerosol type. Over Sacramento, lower depolarization and
1175 higher backscatter wavelength dependence is consistent with smaller, spherical particles typically
1176 seen over urban areas; in contrast, over the mountains east of Sacramento, higher depolarization
1177 and smaller backscatter wavelength dependence is consistent with larger, more non-spherical
1178 particles often associated with dust.

1179 The HSRL data showed a difference in the backscatter color ratio (532/1064 nm) and
1180 aerosol depolarization (532 nm) between the SW and NW flow regimes discussed in sections 4.1
1181 and 4.3.2. These parameters were used to qualitatively classify the HSRL aerosol measurements
1182 into several aerosol types. The NW flow suggests larger, more non-spherical particles that, based
1183 on the prior observations and the classification scheme, appear like a dusty mix. The SW flow
1184 regime suggests, smaller, more spherical particles that are more consistent with urban and
1185 occasionally maritime conditions.

1186 **4.5. Aircraft Observations of Sacramento Plume Evolution**

1187 To complement the extensive observations at the T0 and T1 sites, the G-1 was deployed on
1188 selected days during both SW and NW flow periods to sample upwind of, within, and outside the
1189 evolving Sacramento urban plume as it was advected downwind. Other flight plans included
1190 sampling the inflow from the Bay Area into the Central Valley and characterizing isoprene emission
1191 flux over the forested areas in the Sierra Nevada foothills. An intercomparison flight with the
1192 NOAA WP-3 was also carried on June 18 in the San Joaquin Valley, from Fresno to Bakersfield, CA.
1193 The G-1 flew at a similar altitude as the WP-3 while the B-200 and NOAA Twin Otter flew above
1194 both aircraft. Full analysis of all the aircraft data will be reported in the future. Here we briefly
1195 show an example of the G-1, B-200, and NOAA Twin Otter observations in the Sacramento urban
1196 plume on June 28th as it was transported under light westerly winds to the foothills area by late
1197 afternoon. Figure 23 shows semi-Lagrangian tracks of the G-1 flight in the afternoon, with the
1198 points color coded by CO and (isoprene + methyl vinyl ketone + methacrolein) mixing ratios in the
1199 top panels, organic aerosol and BC mass concentrations in the middle panels, and scattering and
1200 absorption coefficients in the bottom panels. While the flight began at 14:20 PDT and ended at

1201 17:42 PDT, only the portion of the flight between 15:51 and 16:51 PDT is shown here for clarity. All
1202 flight legs in the valley were performed at an altitude of ~340 m MSL while the leg over the
1203 foothills area (passing over the T1 site) was performed at ~850 m MSL due to the higher elevation
1204 of the terrain.

1205 The Sacramento urban plume is clearly noticeable from the enhanced CO mixing ratios,
1206 with highs above 250 ppbv in the plume and lows around 120 ppbv in the surrounding air. Sum of
1207 isoprene and its first generation photooxidation products – methyl vinyl ketone (MVK) and
1208 methacrolein (MACR) – were around 1 ppbv or less west of T0 and gradually increased to the east,
1209 with values between 4 and 8 ppbv over the foothills. Organics constituted more than 90% of the
1210 total observed submicron aerosol mass and was significantly enhanced in the urban plume, with
1211 highs over $25 \mu\text{g m}^{-3}$ STP and lows $\sim 10 \mu\text{g m}^{-3}$ STP in the surrounding air. BC mass concentrations
1212 in the Sacramento plume ranged between 0.1 and $0.2 \mu\text{g m}^{-3}$ STP and were between 0.03 and 0.07
1213 $\mu\text{g m}^{-3}$ STP in the surrounding air. High BC mass concentrations were also observed in the western-
1214 most portion of the flight track, which coincides with Woodland, a relatively small town
1215 (population $\sim 50,000$) located about 25 km northwest of Sacramento. The nephelometer scattering
1216 coefficient in the plume was as high as 54 Mm^{-1} STP and the lows were $\sim 20 \text{ Mm}^{-1}$ STP in the
1217 surrounding air. Finally, PSAP absorption coefficient tracked with BC mass concentration and was
1218 as high as $\sim 8 \text{ Mm}^{-1}$ STP; the values in the surrounding air ranged from ~ 1 to 3 Mm^{-1} STP.

1219 Figure 24 shows HSRL measurements of aerosol extinction profiles and AOD values (at $\lambda =$
1220 532 nm) acquired along a portion of the B200 flight track over the Sacramento region during the
1221 afternoon of June 28 (15:56 PDT to 17:28 PDT). This portion of the B-200 flight track matched that
1222 of the G-1, which acquired comprehensive in situ observations within these lidar “curtains”. The
1223 height of the boundary layer derived from the HSRL data varied between about 1200-2000 m
1224 above ground level. The B-200 aerosol extinction and AOD values were enhanced east of the T0
1225 site and were largest just south of the T1 site, consistent with the location of the plume as
1226 identified from in situ G-1 observations. While the aerosol extinction derived from HSRL
1227 measurements appears to be comparable to the estimated in situ extinction values (sum of
1228 scattering and absorption), a detailed comparison of the two will be the topic of a separate study.

1229 Figure 25 depicts ozone profiles observed with the TOPAZ lidar (Figure 25a) and NO₂
1230 vertical column densities (VCD) measured with the CU AMAX DOAS (Figure 25 b) along the NOAA
1231 Twin Otter flight track over the Sacramento area on June 28 for two flight segments from 11:28 –
1232 12:03 and 13:04 – 13:52 PDT. The TOPAZ lidar data clearly show the elevated ozone
1233 concentrations in the Sacramento plume downwind to the east of the city. Peak ozone
1234 concentrations in the plume approach 125 ppbv and were measured about 30 km to the east of
1235 Sacramento at about 13:40 PDT. Mixing heights were generally between 800 and 1100 m MSL,
1236 except 1500 m MSL or higher within the core of the Sacramento plume. The Twin Otter data were
1237 taken about three hour prior to the G-1 and B-200 observations shown in Figures 23 and 24. The
1238 Sacramento plume had not yet progressed as far east as shown by the G-1 and B-200
1239 measurements and was just approaching the base of the Sierra Nevada Foothills south of the T1
1240 site. Mixing heights were lower by several hundred meters compared to the B-200 observations,
1241 which is consistent with a midday convective boundary layer that is still growing. The CU AMAX-
1242 DOAS data showed significant variability in the NO₂ VCD below the aircraft. The boundary
1243 conditions upwind of Sacramento are characterized by an elevated yet variable NO₂ VCD in the

1244 range 3 to 4 X 10¹⁵ molecule cm⁻², or 1.2 and 1.7 ppb NO₂ averaged over the mixed air column.
1245 Along the west to east transect passing over the Sacramento urban core, a distinct increase in the
1246 NO₂ VCD is observed near the city center, indicating NO_x emissions most likely from mobile
1247 sources. The NO₂ VCD reaches peak values above 1 X 10¹⁶ molecule cm⁻² over the urban core, and
1248 decreases to about half that value about 15 km to the east of Sacramento. No significant
1249 suppression of O₃ is observed over the city center. Rather, in the area of peak NO₂ also O₃
1250 increases simultaneously and immediately, reflecting hydrocarbon to NO_x ratios that are favorable
1251 for fast photochemical O₃ production in the Sacramento plume. The O₃ background levels upwind
1252 (50 ppb) increase along this flight track to 80 ppb near the NO₂ maximum, and peak O₃ exceeds
1253 100 ppb only about 15 km to the east of Sacramento. The NO₂ VCDs measured by CU AMAX-DOAS
1254 provide unique column integral data over mixing height that are insensitive to model errors in
1255 predicting mixing height. The column data facilitate a direct comparison to model predicted NO₂
1256 VCDs, and enable more direct testing of the NO_x emission inventory in the Sacramento area.
1257 Accurate NO_x emissions are prerequisite for predicting photochemical O₃ production by chemical
1258 transport models. In principle, the combination of the TOPAZ lidar and CU AMAX-DOAS can also be
1259 used to constrain O_x (sum of O₃ + NO₂), which is a useful metric for characterizing photochemical
1260 formation of SOA.

1261

1262 **5. Summary and Future Directions**

1263 The CARES field campaign was designed to examine the interaction between
1264 anthropogenic and biogenic emissions in SOA formation, black carbon ageing, and their effects on
1265 the associated optical and CCN activation properties. The campaign was carried out from June 2nd
1266 through 28th, 2010, in Central Valley, California, centered on the Sacramento urban area. Two
1267 heavily-instrumented ground sites – one within the Sacramento urban area (site T0) and another
1268 in Cool, CA, a small town about 40 km to the northeast in the foothills area (site T1) – were set up
1269 to characterize the evolution of meteorological variables, trace gases, aerosol precursors, aerosol
1270 size, composition, and optical and CCN activation properties in freshly polluted and aged urban air.
1271 On selected days, the DOE G-1 aircraft was deployed to make similar measurements upwind and
1272 across the evolving Sacramento plume in the morning and again in the afternoon. The NASA B-200
1273 aircraft, carrying remote sensing instruments (HSRL and RSP), was also deployed to characterize
1274 the vertical and horizontal distribution of aerosols and aerosol optical properties within and
1275 around the plume. The CARES campaign overlapped temporally with the CalNex campaign in the
1276 Central Valley and Southern California regions in May and June 2010. As part of CalNex, the NOAA
1277 Twin Otter aircraft, carrying a combination of downward-looking ozone/aerosol and Doppler wind
1278 lidars and a multi-axis DOAS system, moved its operation from Southern California to Sacramento
1279 to collaborate with CARES from June 14th to 28th. The main initial findings from the CARES
1280 campaign are summarized below:

- 1281 – On approximately 20 days out of a total of 27, the Sacramento urban plume transport was
1282 largely controlled by southwesterly winds that drew the polluted air to the northeast over the
1283 forested areas in the Sierra Nevada foothills where it mixed with biogenic emissions by late
1284 afternoon or early evening. On the remaining ~7 days (June 10-13, 16, and 20-21), the
1285 southwesterly wind pattern was interrupted by northwesterly flows, which transported the

1286 Sacramento plume to the southeast into the San Joaquin Valley, where there was relatively
1287 much less mixing with biogenic emissions.

1288 – The period from June 22nd through 28th also experienced a steady buildup of aged aerosols due
1289 to recirculation of air in the region, coupled with warmer temperatures toward the end of
1290 June. These conditions resulted in the highest pollution days at the end of the campaign, from
1291 June 25th through 28th. Observations across the relatively cleaner and more polluted periods as
1292 well as across the SW and NW flow regimes thus provide an exceptional opportunity to
1293 examine aerosol formation and evolution processes in the same region under a range of
1294 environmental conditions.

1295 – The urban site T0 experienced significantly higher mixing ratios of the primary emission species
1296 such as CO, NO_y, and anthropogenic VOCs compared to the rural foothills site T1, and the
1297 diurnal behaviors of these species were also similar to each other, as expected. In contrast, the
1298 diurnal behavior of biogenic isoprene mixing ratios at both the sites followed that of the
1299 surface temperatures. The peak mixing ratios ranged between 2 and 12 ppbv around 14:00
1300 PDT while the minimum mixing ratios were nearly zero from midnight until dawn. Since the T1
1301 site was located amidst biogenic emissions, isoprene mixing ratios there were generally about
1302 0.5 to 3 ppbv higher than at T0. The diurnal behavior of photochemically produced O₃ at the T0
1303 and T1 sites were quite similar despite the marked differences in the precursor trace gas
1304 composition and concentrations between the two sites. The highs ranged between 60 and 80
1305 ppbv, except for a peak of nearly 120 ppbv on June 28th. The daily O₃ peaks at T0 typically
1306 occurred around 15:00 PDT while it was often delayed by ~3 h at T1 on days when the urban
1307 plume was transported to the site during the SW flow periods.

1308 – Sub-micron non-refractory aerosol composition observed at both the ground sites and aboard
1309 the G-1 aircraft was dominated by organics, followed by sulfate, followed by nitrate and
1310 ammonium, while chloride was negligibly small. OA concentrations at the ground sites ranged
1311 between <0.5 and 10 μg m⁻³ STP and displayed a diurnal cycle that was similar to that of O₃ at
1312 both sites, which is consistent with photochemical production of SOA from anthropogenic and
1313 biogenic VOCs. OA concentrations typically peaked at the T0 site around 15:00 PDT while it
1314 peaked around 18:00 PDT or later at the T1 site as the urban plume was transported to the
1315 foothills area during the SW flow periods. Enhanced concentrations of aged organic aerosols,
1316 likely recirculated from the foothills area the previous day, were often observed in the residual
1317 layer during the morning flights over the Sacramento urban area, which is consistent with
1318 preliminary WRF simulation results presented in Fast et al. (2012). The period from June 22nd
1319 to 28th experienced a steady buildup of OA, with concentrations reaching more than 25 μg m⁻³
1320 STP aloft in the urban plume as it was transported east to the foothills area on the afternoon
1321 of the 28th.

1322 – On selected days during both SW and NW flow periods, the daytime evolution of key trace
1323 gases, aerosol composition, mixing state, size distribution, and optical properties in the
1324 Sacramento urban plume was observed by the G-1 as it sampled upwind of, across, and
1325 downwind of the drifting plume in the morning and afternoon. These semi-Lagrangian in situ
1326 observations were complemented by NASA B-200 observations of vertical profiles of aerosol
1327 optical properties, which provided a more complete picture of the 3-dimensional structure of
1328 the evolving urban plume and the surrounding air. In the latter half of the campaign, this

1329 picture was further enhanced by NOAA Twin Otter observations of vertical profiles of O₃, NO₂,
1330 HCHO, CHOCHO, and wind speed in Sacramento and surrounding areas.

1331 – Single particle mass spectrometers (SP-MS) deployed on the G-1 (A-ATOFMS), at T0 (SPLAT II),
1332 and at T1 (PALMS) also showed that the vast majority of aerosol particles characterized during
1333 the study were composed of oxygenated organics mixed with various amounts of sulfates:
1334 from sulfate-dominated particles to those containing mostly organic species. In addition, fresh
1335 and processed soot particles, biomass burning aerosol, amines, sea salt (both fresh and
1336 processed), and a small number of mineral dust and other inorganic particles were observed.
1337 The A-ATOFMS provided semi-Lagrangian aerial snapshots of particle mixing states in the
1338 evolving urban plume. In contrast, the SPLAT II, which was operated almost continuously for
1339 the entire campaign period, provided a detailed view of the evolution of relative fractions of
1340 different primary and secondary particle types in a single day, albeit at a fixed urban site. Size-
1341 and composition-selected SOA-dominated particles were also analyzed using SPLAT II to study
1342 evaporation kinetics at room temperature (Vaden et al., 2011a). This study is the first to
1343 present field evidence that evaporation of these ambient organic particles was extremely slow
1344 and size-independent, suggesting that the particles were in a quasi-solid state.

1345 – SP2 instruments (outfitted with a scattering channel) deployed on the G-1 and at both the
1346 ground sites provided data on BC number and mass concentrations for particles between 60
1347 and 600 nm BC mass equivalent diameters as well as coating state data for particles between
1348 ~175 and 350 nm. Preliminary analysis of G-1 SP2 data for June 28th showed an increase in the
1349 coating mass to BC mass ratio in the urban plume between the morning and afternoon flights.
1350 Particles were also collected using TRAC and DRUM samplers on all three platforms for offline
1351 analyses to further probe the chemical composition, mixing state, and morphology.

1352 – SO₂ emitted from oil refineries in the Bay Area appears to have been routinely transported to
1353 the Sacramento area during the SW flow periods. These SO₂ plumes were associated with
1354 increased number concentrations of ultrafine and Aitken mode particles, which were likely
1355 nucleated via H₂SO₄ formation from SO₂ photooxidation, followed by growth to the observed
1356 sizes during transit. The Aitken mode was typically observed at both the ground sites in the
1357 morning around 09:30 PDT, followed by continued growth to accumulation mode sizes until
1358 mid-afternoon, likely due to condensation of photochemically formed SOA species. In contrast,
1359 SO₂ mixing ratios were negligibly small and the Aitken mode aerosol number concentrations
1360 were also significantly lower in the sampling domain during the NW flow periods.

1361 – Coarse mode aerosols, mostly consisting of sea salt, were found to be transported from the
1362 Pacific Ocean/Bay Area to the Sacramento area on several occasions during the SW flow
1363 periods. Electron microscopy and X-ray spectro-microscopy analysis of TRAC collected particles
1364 onboard the G-1 over Sacramento on June 15 (a strong SW flow event) revealed that the sea
1365 salt particles were internally mixed with organics, which are likely SOA species formed in these
1366 particles during transit from the Bay Area. Surprisingly, these particles had experienced
1367 substantial chloride depletion that could not be explained by the known reactivity of sea salt
1368 with nitric and sulfuric acids (Laskin et al., 2012). This study is the first to present field evidence
1369 that SOA, consisting of weak organic acids, may effectively react with sea salt particles and
1370 displace HCl gas, leaving behind particles depleted in chloride and enriched in the
1371 corresponding organic salts.

- 1372 – In situ aerosol optical properties were measured at near-UV and visible spectral regions
1373 onboard the G-1 and at T0 and T1 ground sites with several instruments, including
1374 nephelometer, PSAP, and PAS. A CRDS instrument was also deployed at the ground sites.
1375 When the coarse mode particles were present, the scattering coefficients ($\lambda = 550$ nm)
1376 reached as high as 40 to 75 Mm^{-1} and 20 to 50 Mm^{-1} at the T0 and T1 sites, respectively, and
1377 were about 2 to 4 times higher than the scattering coefficients of submicron particles. In
1378 contrast, the scattering coefficients ranged between 4 and 20 Mm^{-1} when the coarse mode
1379 particles were largely absent during first week of June and later again during the NW flow
1380 periods. MFRSR observations at each ground site provided the diurnal, day-to-day, and site-by-
1381 site variations in column aerosol microphysical and optical properties, such as aerosol optical
1382 depth, single scattering albedo, and asymmetry parameter. Consistent with the in situ optical
1383 properties measurements, MFRSR AOD values were observed to range from about 0.025
1384 (representing very clean air) at the start of the campaign to about 0.12 towards the end of the
1385 campaign. Additionally, coarse aerosol mode size distributions derived from MFRSR data were
1386 also found to be consistent with the in situ size distribution measurements at both ground
1387 sites.
- 1388 – BC absorption enhancement (E_{abs}) was directly determined at the T0 site (and onboard R/V
1389 Atlantis) as the ratio of the absolute particulate absorption before passing the particles
1390 through a thermodenuder to that measured after passing through the thermodenuder. The
1391 observed E_{abs} was small (about 6% on average at 532 nm), and increased weakly with
1392 photochemical ageing. In sharp contrast, observationally-constrained core-shell Mie theory
1393 calculations for the R/V Atlantis data predicted E_{abs} values close to 100% (Cappa et al., 2012).
1394 This study is the first direct determination of BC absorption enhancement in ambient
1395 atmospheric aerosol samples.
- 1396 – Observations of CCN concentrations are also available at multiple supersaturations (0.07 to 0.5
1397 %) at both ground sites. The T1 site also included measurement of size-resolved CCN
1398 concentrations and variable relative humidity nephelometry (commonly referred to as $f(\text{RH})$
1399 measurement).

1400 The CARES measurements have been processed and uploaded into the final ARM data
1401 archive (<http://campaign.arm.gov/cares>). These measurements comprise a rich data set for: 1)
1402 investigating SOA formation from anthropogenic and biogenic precursors and the potential
1403 interactions between them; 2) characterizing the time scales of BC ageing and evolution of its
1404 mixing state; and 3) quantifying the roles of BC mixing state, organics, and coarse mode aerosols
1405 on the observed optical and CCN activation properties. As mentioned throughout this paper,
1406 several detailed studies using various CARES data are planned or presently underway and will be
1407 reported via subsequent publications in this special issue and elsewhere as appropriate. Here we
1408 briefly summarize some of the key science questions that can be investigated using CARES data.

1409 **Secondary Organic Aerosols**

- 1410 a) Can we reliably infer IVOC (and SVOC) concentrations in the urban air, how they varied
1411 diurnally and scaled with VOC and CO concentrations, and how did these aerosol precursor
1412 gases correlate with organic aerosol number and mass concentrations in freshly polluted urban
1413 air?

- 1414 b) What were the chemical composition, volatility spectrum, and hygroscopicity of OA, and how
1415 did they evolve as a function of atmospheric processing time and photochemical age?
- 1416 c) Is there evidence for enhanced SOA formation in the urban plume when it mixed with biogenic
1417 emissions (e.g., during southwesterly flow conditions) compared to instances when the urban
1418 plume did not mix with biogenic emissions (e.g., during northwesterly flow conditions)? Can
1419 the observed SOA in the aged urban plume be separated into anthropogenic and biogenic
1420 fractions using carbon isotope analyses and other methods based on PTRMS observations and
1421 positive matrix factorization of AMS mass spectra?
- 1422 d) How did the size distribution of aerosols evolve with SOA formation in the urban plume? Does
1423 the SOA condensation kinetics appear to be driven by Raoult's Law type gas absorption
1424 thermodynamics or is it similar to that of a condensing non-volatile species?
- 1425 e) What was the role of organic species in the observed growth of ultrafine particles to CCN and
1426 optically active sizes?

1427 **Aerosol Mixing State**

- 1428 a) What was the distribution of BC mass fraction (BC mixing state) as a function of particle size in
1429 fresh and aged urban plumes? How rapidly did POA, BC, SOA, and inorganics become internally
1430 mixed?
- 1431 b) What were the relative roles of condensation and coagulation processes in shaping the aerosol
1432 composition and size distribution?
- 1433 c) What were the contributions and mixing states of other primary emissions such as biomass
1434 burning aerosol, mineral dust and sea salt, and how did these aerosols evolve?
- 1435 d) What were the effects of aerosol mixing state on the ensemble aerosol optical properties,
1436 hygroscopicity, and CCN activity?

1437 **Aerosol Optical Properties**

- 1438 a) What was the role of changes in BC mixing state and morphology on enhanced light
1439 absorption?
- 1440 b) Was there increased (by OA over BC) near-UV absorption? Did OA absorption extend into the
1441 visible part of the spectrum? If so, how did it relate to OA composition?
- 1442 c) What were the absolute and relative contributions of sub-micron and super-micron aerosols to
1443 the total aerosol direct radiative forcing?
- 1444 d) Which compounds or particle types have the strongest radiative impacts, and can these be
1445 related to specific emission sources or atmospheric formation processes?

1446 The resulting detailed picture for the evolution of different types of carbonaceous aerosols
1447 and their optical and CCN activation properties will then help improve the key aerosol process and
1448 property modules that are used in regional and global climate models. Specific modeling studies
1449 that are planned by CARES participants include:

- 1450 – Local closures for optical and CCN activation properties.

- 1451 – Constrained Lagrangian modeling of SOA formation and interactions between anthropogenic
1452 and biogenic emissions.
- 1453 – Constrained Lagrangian modeling of black carbon mixing state evolution.
- 1454 – Regional simulations of SOA formation that include long-range transport of trace gases and
1455 aerosols
- 1456 – Assessments of new treatments of SOA and aerosol mixing state on aerosol optical and
1457 hygroscopic properties and their impact on radiative forcing over California and surrounding
1458 regions.

1459 In closing, it is reiterated that the purpose of this early overview paper is to summarize the
1460 scientific objectives, the platforms and instrumentation, the sampling strategies, and the key
1461 observations collected during the campaign, and develop an initial list of specific science questions
1462 that could be investigated with the CARES data set. It is hoped that this paper will facilitate further
1463 analyses of this remarkably rich data set as well as stimulate ideas for novel, collaborative studies.
1464

1465 **Acknowledgements:** The authors thank the DOE G-1, NASA Langley B-200 King Air, and NOAA
1466 Twin Otter flight crew and numerous staff from all the involved institutions for their outstanding
1467 work in support of the CARES field mission. The contributions and cooperation of the following in
1468 this research effort are gratefully acknowledged: Dr. Eileen McCauley, Dr. Ajith Kaduwela, Dr.
1469 James Pederson, Dr. Leon Dolislager, and colleagues at California Air Resources Board (CARB) for
1470 their assistance in planning this study; Dr. Anthony Wexler (UC Davis), Dr. Ron Cohen (UC
1471 Berkeley), and Dr. Allen Goldstein (UC Berkeley) for helpful discussions during the planning stages
1472 of the study; Dr. John Ogren and his group at NOAA for their assistance with aerosol rack and data
1473 collection during the campaign; Ms. Wendy Westsmith and the staff at Northside School in Cool,
1474 Mr. Laduan Smedley and the staff at American River College in Sacramento, and staff at McClellan
1475 Airfield for the use of their facilities. Funding for data collection onboard the G-1 aircraft and at
1476 the ground sites was provided by the Atmospheric Radiation Measurement (ARM) Program
1477 sponsored by the U.S. Department of Energy (DOE), Office of Biological and Environmental
1478 Research (OBER). Partial support was also provided by the Environmental Molecular Sciences
1479 Laboratory (EMSL), a national scientific user facility sponsored by the DOE's OBER at Pacific
1480 Northwest National Laboratory (PNNL). Funding for the B-200/HSRL/RSP deployment and
1481 investigations came from the NASA HQ Science Mission Directorate Radiation Sciences Program,
1482 the NASA CALIPSO project, and the DOE ARM Program, Interagency Agreement No. DE-AI02-
1483 05ER63985. Funding for data collection and analysis of the measurements taken onboard the
1484 NOAA Twin Otter was provided by the NOAA Health of the Atmosphere Program. Participation of
1485 R. Volkamer, S. Baidar, H. Oetjen, and I. Ortega (University of Colorado, Boulder) was made
1486 possible by the California Air Resources Board contract 09-317, and NSF-CAREER award AGS-
1487 0847793. Participation of A. Kubátová and H. Jeong (University of North Dakota) was made
1488 possible by funding from ND EPSCoR through NSF grant #EPS-814442. Participation of C.D Cappa
1489 and K.R. Kolesar (University of California, Davis) was made possible by funding from NOAA and U.S.
1490 EPA. This research was also supported by the U.S. DOE's Atmospheric System Research (ASR)
1491 Program under Contract DE-AC06-76RLO 1830 at PNNL. PNNL is operated for the U.S. DOE by
1492 Battelle Memorial Institute.

1493
1494 **References**

1495 Adachi, K. and Buseck, P. R.: Internally mixed soot, sulfates, and organic matter in aerosol particles
1496 from Mexico City, *Atmos. Chem. Phys.*, 8, 6469-6481, 2008.

1497 Adachi, K., Chung, S. H., and Buseck, P. R.: Shapes of soot aerosol particles and implications for
1498 their effects on climate, *J. Geophys. Res.*, 115, D15206, doi:10.1029/2009JD012868, 2010.

1499 Aiken, A. C. et al.: O/C and OM/OC Ratios of Primary, Secondary, and Ambient Organic Aerosols
1500 with a High Resolution Time-of-Flight Aerosol Mass Spectrometer, *Environ. Sci. and Technol.*,
1501 42(12), 4478-4485, doi:4410.1021/es703009q, 2008.

1502 Alvarez II, R. J., Senff, C. J., Langford, A. O., Weickmann, A. M., Law, D. C., Machol, J. L., Merritt, D.
1503 A., Marchbanks, R. D., Sandberg, S. P., Brewer, W. A., Hardesty, R. M., Banta, R. M.: Development
1504 and application of a compact, tunable, solid-state airborne ozone lidar system for boundary layer
1505 profiling, *J. Atmos. Oceanic Technol.*, doi: 10.1175/JTECH-D-10-05044.1, 2011.

1506 Anderson, T. L., Covert, D. S., Marshall, S. F., Laucks, M. L., Charlson, R. J., Waggoner, A. P., Ogren,
1507 J. A., Caldow, R., Holm, R. L., Quant, F. R., Sem, G. J., Wiedensohler, A., Ahlquist, N. A., and Bates,
1508 T. S.: Performance characteristics of a high-sensitivity, three-wavelength total scatter/backscatter
1509 nephelometer, *J. Atmos. Oceanic Technol.*, 13, 967-986, 1996.

1510 Andreae, M. O. and Gelencsér, A.: Black carbon or brown carbon? The nature of light-absorbing
1511 carbonaceous aerosols, *Atmos. Chem. Phys.*, 6, 3131-3148, 2006.

1512 Arnott, W. P., Moosmuller, H., Rogers, C. F., Jin, T. F. and Bruch, R.: Photoacoustic spectrometer
1513 for measuring light absorption by aerosol: instrument description, *Atmos. Environ.*, 33, 2845-2852,
1514 1999.

1515 Barsanti, K. C., and Pankow, J. F.: Thermodynamics of the formation of atmospheric organic
1516 particulate matter by accretion reactions - 2. Dialdehydes, methylglyoxal, and diketones, *Atmos.*
1517 *Environ.*, 39(35), 6597-6607, 2005.

1518 Bauer, S. E., Wright, D. L., Koch, D., Lewis, E. R., McGraw, R., Chang, L. S., Schwartz, S. E., and Rued,
1519 R.: MATRIX (Multiconfiguration Aerosol TRacker of mIXing state): An aerosol microphysical
1520 module for global atmospheric models, *Atmos. Chem. Phys.*, 8, 6003-6035, doi:10.5194/acp-8-
1521 6003-2008, 2008.

1522 Baumgardner, D., Jonsson, H., Dawson, W., O'Connor, D., Newton, R.: The cloud, aerosol and
1523 precipitation spectrometer: a new instrument for cloud investigations, *Atmospheric Research*, Vol.
1524 59-60, 251-264, doi:10.1016/S0169-8095(01)00119-3, 2001.

1525 Bergstrom, R. W., Russell, P. B., and Hignett, P.: Wavelength dependence of the absorption of
1526 black carbon particles: Predictions and results from the TARFOX experiment and implications for
1527 the aerosol single scattering albedo, *J. Atmos. Sci.*, 59, 567-577, 2002.

1528 Bond, T. C.: Can warming particles enter global climate discussions?, *Environ. Res. Lett.*, 2, 045030,
1529 doi:10.1088/1748-9326/2/4/045030, 2007.

1530 Bond, T. C., Habib, G., and Bergstrom, R. W.: Limitations in the enhancement of visible light
1531 absorption due to mixing state, *J. Geophys. Res.*, 111, D20211, doi:10.1029/2006JD007315, 2006.

1532 Bones, D. L., Henricksen, D. K., Mang, S. A., Gonsior, M., Bateman, A. P., Nguyen, T. B., Cooper, W.
1533 J., and Nizkorodov, S. A.: Appearance of strong absorbers and fluorophores in limonene-O3

1534 secondary organic aerosol due to NH₄⁺-mediated chemical aging over long time scales, *J.*
1535 *Geophys. Res.*, 115, D05203, doi:10.1029/2009JD012864, 2010.

1536 Bruns, E. A., et al.: Comparison of FTIR and particle mass spectrometry for the measurement of
1537 particulate organic nitrates, *Environ. Sci. Technol.*, 44(3), 1056-1061, 2010.

1538 Bueno, P. A., Havey, D. K., Mulholland, G. W., Hodges, J. T., Gillis, K. A., Dickerson, R. R., and
1539 Zachariah, M. R.: Photoacoustic measurements of amplification of the absorption cross section for
1540 coated soot aerosols, *Aerosol Sci. Technol.* 45, 1217-1230, doi:10.1080/02786826.2011.587477,
1541 2011.

1542 Burton, S. P., Ferrare, R. A., Hostetler, C. A., Hair, J. W., Rogers, R. R., Obland, M. D., Butler, C. F.,
1543 Cook, A. L., Harper, D. B., and Froyd, K. D.: Aerosol classification using airborne High Spectral
1544 Resolution Lidar measurements – methodology and examples, *Atmos. Meas. Tech. Discuss.*, 4,
1545 5631-5688, doi:10.5194/amtd-4-5631-2011, 2011.

1546 Buzorius, G., Zelenyuk, A., Brechtel, F. and Imre, D.: Simultaneous determination of individual
1547 ambient particle size, hygroscopicity and composition, *Geophys. Res. Lett.*, 29, 1974,
1548 doi:10.1029/2001GL014221, 2002.

1549 Cai, Y., Montague, D.C., Mooiweer-Bryan, W., Deshler, T.: Performance characteristics of the ultra
1550 high sensitivity aerosol spectrometer for particles between 55 and 800 nm: Laboratory and field
1551 studies, *J. Aerosol Sci.*, 39(9), 759-769, doi:10.1016/j.jaerosci.2008.04.007, 2008.

1552 Canagaratna, M., Jayne, J., Jimenez, J. L., Allan, J. A., Alfarra, R., Zhang, Q., Onasch, T., Drewnick, F.,
1553 Coe, H., Middlebrook, A., Delia, A., Williams, L., Trimborn, A., Northway, M., DeCarlo, P., Kolb, C.,
1554 Davidovits, P., and Worsnop, D.: Chemical and microphysical characterization of ambient aerosols
1555 with the Aerodyne aerosol mass spectrometer, *Mass Spectrometry Reviews*, 26, 185-222,
1556 doi:10.1002/mas.20115, 2007.

1557 Cantrell, W., Shaw, G., Cass, G. R., Chowdhury, Z., Hughes, L. S., Prather, K. A., Guazzotti, S. A., and
1558 Coffee, K. R.: Closure between aerosol particles and cloud condensation nuclei at Kaashidhoo
1559 Climate Observatory, *J. Geophys. Res.*, 106, 28,711–28,718, doi:10.1029/2000JD900781, 2001.

1560 Cappa, C. D., Lack, D. A., Burkholder, J. B. and Ravishankara, A. R.: Bias in filter-based aerosol light
1561 absorption measurements due to organic aerosol loading: Evidence from laboratory
1562 measurements, *Aerosol Sci. Technol.*, 42, 1022-1032, 2008.

1563 Cappa, C. D., Onasch, T. B., Massoli, P., Worsnop, D. R., Bates, T. S., Cross, E. S., Davidovits, P.,
1564 Gaston, C. J., Hakala, J., Hayden, K., Jobson, B. T., Kolesar, K. R., Lack, D. A., Lerner, B. M., Li, S. -M.,
1565 Mellon, D., Nuaaman, I., Olfert, J., Petäjä, T., Prather, K. A., Quinn, P. K., Song, C., Subramanian, R.,
1566 Vlasenko, A., Williams, E. J., Zaveri, R. A.: Radiative absorption enhancements due to the mixing
1567 state of atmospheric black carbon, *Science*, 2012, accepted.

1568 Cattrall, C., Reagan, J., Thome, K., and Dubovik, O.: Variability of aerosol and spectral lidar and
1569 backscatter and extinction ratios of key aerosol types derived from selected Aerosol Robotic
1570 Network locations, *J. Geophys. Res.*, 110, D10S11, doi:10.1029/2004JD005124, 2005.

1571 Cerling, T. E., Harris, J. M.: Carbon isotope fractionation between diet and bioapatite in ungulate
1572 mammals and implications for ecological and paleoecological studies, *Oecologia*, 120, 347-363,
1573 1999.

1574 Cross, E. et al.: Soot particle studies – Instrument inter-comparison – Project overview, *Aerosol Sci.*
1575 *Technol.*, 44(8), 592-611, 2010.

1576 Cziczo, D. J.; Thomson, D. S.; Thompson, T. L.; DeMott, P. J.; Murphy, D. M.: Particle analysis by
1577 laser mass spectrometry (PALMS) studies of ice nuclei and other low number density particles, *Int.*
1578 *J. Mass Spectrom.*, 2006, 258, 21-29, 2006.

1579 Cubison, M. J., Ervens, B., Feingold, G., Docherty, K. S., Ulbrich, I. M., Shields, L., Prather, K., Hering,
1580 S., and Jimenez, J. L.: The influence of chemical composition and mixing state of Los Angeles urban
1581 aerosol on CCN number and cloud properties, *Atmos. Chem. Phys.*, 8, 5649–5667,
1582 doi:10.5194/acp-8-5649-2008, 2008.

1583 de Haan, D. O., Corrigan, A. L., Smith, K.W., Stroik, D. R., Turley, J. J., Lee, F. E., Tolbert, M. A.,
1584 Jimenez, J. L., Cordova, K. E., and Ferrell, G. R.: Secondary organic aerosol-forming reactions of
1585 glyoxal with amino acids, *Environ. Sci. Tech.*, 43, 2818–2824, 2009a.

1586 de Haan, D. O., Tolbert, M. A., and Jimenez, J. L.: Atmospheric condensed-phase reactions of
1587 glyoxal with methylamine, *Geophys. Res. Lett.*, 36, L11819, doi:11810.11029/12009GL037441,
1588 2009b.

1589 Delene, D. J. and Ogren, J. A.: Variability of Aerosol Optical Properties at Four North American
1590 Surface Monitoring Sites, *J. Atmos. Sci.*, 59(6), 1135-1150, 2002.

1591 Doran, J. C., Fast, J. D., Barnard, J. C., Laskin, A., Desyaterik, Y., and Gilles M. K.: Applications of
1592 Lagrangian dispersion modeling to the analysis of changes in the specific absorption of elemental
1593 carbon, *Atmos. Chem. Phys.*, 8, 1377-1389, 2008.

1594 Dzepina, K., Volkamer, R. M., Madronich, S., Tulet, P., Ulbrich, I. M., Zhang, Q., Cappa, C. D.,
1595 Ziemann, P. J., and Jimenez, J. L.: Evaluation of recently-proposed secondary organic aerosol
1596 models for a Case study in Mexico City, *Atmos. Chem. Phys.*, 9, 5681–5709, doi:10.5194/acp-9-
1597 5681-2009, 2009.

1598 Duarte, R. M. B. O., Pio, C. A., and Duarte, A. C.: Spectroscopic study of the water-soluble organic
1599 matter isolated from atmospheric aerosols collected under different atmospheric conditions,
1600 *Analytica Chimica Acta*, 530, 7–14, 2005.

1601 Ehleringer, J.R., Monson, R.K.: Evolutionary and ecological aspects of photosynthetic pathway
1602 variation. *Ann. Rev. Ecol. Syst.*, 24, 411-439, 1993.

1603 Ervens, B. and Kreidenweis, S. M.: SOA formation by biogenic and carbonyl compounds: Data
1604 evaluation and application, *Environ. Sci. Technol.*, 41(11), 3904-3910, 2007.

1605 Erickson, M. H., Wallace, H. W., and Jobson, B. T.: Quantification of diesel exhaust intermediate
1606 volatile organic compounds by a thermal desorption proton transfer reaction mass spectrometer,
1607 *Atmos. Chem. Phys. Discuss.*, 12, 5389-5423, 2012.

1608 Farmer, D. K., Matsunaga, A., Docherty, K. S., Surratt, J. D., Seinfeld, J. H., Ziemann, P. J., and
1609 Jimenez, J. L.: Response of an aerosol mass spectrometer to organonitrates and organosulfates
1610 and implications for atmospheric chemistry, *Proc. Natl. Acad. Sci. U. S. A.*, 107(15), 6670-6675,
1611 2010.

1612 Fast, J. D., W. I. Gustafson Jr., R. C. Easter, R. A. Zaveri, J. C. Barnard, E. G. Chapman, G. A. Grell,
1613 and S. E. Peckham (2006), Evolution of ozone, particulates, and aerosol direct radiative forcing in
1614 the vicinity of Houston using a fully coupled meteorology-chemistry-aerosol model, *J. Geophys.*
1615 *Res.*, 111, D21305, doi:10.1029/2005JD006721.

1616 Fast, J. D., Gustafson Jr., W. I., Berg, L. K., Shaw, W. J., Pekour, M., Shrivastava, M., Barnard, J. C.,
1617 Ferrare, R. A., Hostetler, C. A., Hair, J. A., Erickson, M., Jobson, B. T., Flowers, B., Dubey, M. K.,
1618 Springston, S., Pierce, R. B., Dolislager, L., Pederson, J., and Zaveri, R. A.: Transport and mixing
1619 patterns over Central California during the carbonaceous aerosol and radiative effects study
1620 (CARES), *Atmos. Chem. Phys.*, 12, 1759-1783, doi:10.5194/acp-12-1759-2012, 2012.

1621 Flowers, B. A., Dubey, M. K., Mazzoleni, C., Stone, E. A., Schauer, J. J., Kim, S.-W., and Yoon, S. C.:
1622 Optical-chemical-microphysical relationships and closure studies for mixed carbonaceous aerosols
1623 observed at Jeju Island; 3-laser photoacoustic spectrometer, particle sizing, and filter analysis.
1624 *Atmos. Chem. Phys.*, 10, 10387–10398, 2010.

1625 Fierz, M., Vernooij, M. G. C., and Burtscher, H.: An improved low-flow thermodenuder, *J. Aerosol*
1626 *Sci.*, 38, 1163-1168, 2007.

1627 Forster, P. V., et al. (2007), Changes in Atmospheric Constituents and in Radiative Forcing, in
1628 *Climate Change 2007: The Physical Science Basis: Working Group I Contribution to the Fourth*
1629 *Assessment Report of the IPCC*, edited by S. Solomon, et al., pp. 129–234, Cambridge Univ. Press,
1630 New York.

1631 Fuller, K. A., Malm, W. C., and Kriedenweis, S. M.: Effects of mixing on extinction by carbonaceous
1632 particles, *J. Geophys. Res.*, 104(D13), 15,941-15,954, 1999.

1633 Furutani, H., Dall’osto, M., Roberts, G. C., and Prather, K. A.: Assessment of the relative importance
1634 of atmospheric aging on CCN activity derived from field observations, *Atmos. Environ.*, 42, 3130–
1635 3142, doi:10.1016/j.atmosenv.2007.09.024, 2008.

1636 Gaffney, J. S., Marley, N. A., and Cunningham, M. M.: Natural radionuclides in fine aerosols in the
1637 Pittsburgh area, *Atmos. Environ.*, 38, 3191-3200, 2004.

1638 Gao, R. S., Schwarz, J. P., Kelly, K. K., Fahey, D. W., Watts, L. A., Thompson, T. L., Spackman, J. R.,
1639 Slowik, J. G., Cross, E. S., Han, J.-H., Davidovits, P., Onasch, T. B., and Worsnop, D. R.: A novel
1640 method for estimating light-scattering properties of soot aerosols using a modified single-particle
1641 soot photometer, *Aerosol Sci. Tech.*, 41 125-135, 2007.

1642 Ghan, S. J. and Schwartz, S. E.: Aerosol properties and processes: A Path from field and laboratory
1643 measurements to global climate models, *Bull. Amer. Met. Soc.*, 1059-1083, 2007.

1644 Grell, G. A., Peckham, S. E., Schmitz, R., McKeen, S. A., Frost, G., Skamarock, W. C., and Eder, B.:
1645 Fully coupled “online” chemistry within the WRF model, *Atmos. Environ.*, 39, 6957-6975, 2005.

1646 Guenther, A., Karl, T., Harley, P., Wiedinmyer, C., Palmer, P. I., and Geron, C.: Estimates of global
1647 terrestrial isoprene emissions using MEGAN (Model of Emissions of Gases and Aerosols from
1648 Nature), *Atmos. Chem. Phys.*, 6, 3181-3210, 2006.

1649 Gyawali, M., Arnott, W. P., Lewis, K., and Moosmüller, H.: In situ aerosol optics in Reno, NV, USA
1650 during and after the summer 2008 California wildfires and the influence of absorbing and non-

1651 absorbing organic coatings on spectral light absorption, *Atmos. Chem. Phys.*, 9, 8007-8015,
1652 doi:10.5194/acp-9-8007-2009, 2009.

1653 Gyawali, M., Arnott, W. P., Zaveri, R. A., Song, C., Moosmüller, H., Liu, L., Mishchenko, M. I.,
1654 Chen, L.-W. A., Green, M. C., Watson, J. G., and Chow, J. C.: Photoacoustic optical properties at UV,
1655 VIS, and near IR wavelengths for laboratory generated and winter time ambient urban aerosols,
1656 *Atmos. Chem. Phys.*, 12, 2587-2601, doi:10.5194/acp-12-2587-2012, 2012.

1657 Hair, J. W., Hostetler, C. A., Cook, A. L., Harper, D. B., Ferrare, R. A., Mack, T. L., Welch, W.,
1658 Izquierdo, L. R., and Hovis, F. E.: Airborne High Spectral Resolution Lidar for profiling aerosol
1659 optical properties, *Appl. Optics*, 47(36), 6734-6752, 2008.

1660 Harrison, L., Michalsky, J., and Berndt, J.: Automated Multifilter Rotating Shadow-Band
1661 Radiometer: An instrument for optical depth and radiation measurements, *Appl. Optics*, 33, 5118-
1662 5125, 1994.

1663 Hasegawa, S. and Ohta, S.: Some measurements of the mixing state of soot-containing particles at
1664 urban and non-urban sites, *Atmos. Environ.*, 36, 3899–3908, 2002.

1665 Hastings, W. P., Koehler, C. A., Bailey, E. L., De Haan, D. O.: Secondary organic aerosol formation by
1666 glyoxal hydration and oligomer formation: Humidity effects and equilibrium shifts during analysis,
1667 *Environ. Sci. Technol.*, 39(22), 8728-8735, 2005.

1668 Havers, N., Burba, P., Lambert, J., and Klockow, D.: Spectroscopic characterization of humic-like
1669 substances in airborne particulate matter, *J. Atmos. Chem.*, 29, 45–54, 1998.

1670 Hecobian, A., Zhang, X., Zheng, M., Frank, N., Edgerton E. S., and Weber, R. J.: Water-soluble
1671 organic aerosol material and the light-absorption characteristics of aqueous extracts measured
1672 over the southeastern United States, *Atmos. Chem. Phys.*, 10, 5965-5977, 2010.

1673 Herich, H., Kammermann, L., Friedman, B., Gross, D. S., Weingartner, E., Lohmann, U., Spichtinger,
1674 P., Gysel, M., Baltensperger, U. and Cziczo, D. J.: Subarctic atmospheric aerosol composition: 2.
1675 Hygroscopic growth properties, *J. Geophys. Res.*, 114, D13204, doi:10.1029/2008JD011574, 2009.

1676 Hiranuma, N., Kohn, N., Pekour, M. S., Nelson, D. A., Shilling, J. E., and Cziczo, D. J.: Droplet
1677 activation, separation, and compositional analysis: Laboratory studies and atmospheric
1678 measurements, *Atmos. Meas. Tech. Discuss.*, 4, 691-713, 2011.

1679 Hodzic, A., Jimenez, J. L., Madronich, S., Canagaratna, M. R., DeCarlo, P. F., Kleinman, L., and Fast,
1680 J.: Modeling organic aerosols in a megacity: potential contribution of semi-volatile and
1681 intermediate volatility primary organic compounds to secondary organic aerosol formation,
1682 *Atmos. Chem. Phys.*, 10, 5491–5514, doi:10.5194/acp-10-5491-2010, 2010.

1683 Hoffer, A., Gelencsér, A., Guyon, P., Kiss, G., Schmid, O., Frank, G. P., Artaxo, P., and
1684 Andreae, M. O.: Optical properties of humic-like substances (HULIS) in biomass-burning aerosols,
1685 *Atmos. Chem. Phys.*, 6, 3563-3570, doi:10.5194/acp-6-3563-2006, 2006.

1686 Hopkins, R. J., Desyaterik, Y., Tivanski, A. V., Zaveri, R. A., Berkowitz, C. M., Tylliszczak, T., Gilles, M.
1687 K., and Laskin, A.: Chemical speciation of sulfur in marine cloud droplets and particles: Analysis of
1688 individual particles from the marine boundary layer over the California current, *J. Geophys. Res.*,
1689 113, D04209, doi:10.1029/2007JD008954, 2008.

1690 Jacobson, M. Z.: Strong radiative heating due to the mixing state of black carbon in atmospheric
1691 aerosols, *Nature*, 409, 695-697, 2001.

1692 Jacobson, M. Z.: Control of fossil-fuel particulate black carbon and organic matter, possibly the
1693 most effective method of slowing global warming, *J. Geophys. Res.*, 107, 4410,
1694 doi:10.1029/2001JD001376, 2002.

1695 Jacobson, M. Z.: Effects of externally-through-internally-mixed soot inclusions within clouds and
1696 precipitation on global climate, *J. Phys. Chem. A*, 110(21), 6860-6873, doi:10.1021/jp056391r,
1697 2006.

1698 Jaoui, M., Kleindienst, T. E., Lewandowski, M., Offenberg, J. H., Edney, E. O.: Identification and
1699 quantification of aerosol polar oxygenated compounds bearing carboxylic or hydroxyl groups. 2.
1700 Organic tracer compounds from monoterpenes, *Environ. Sci. Technol.*, 39(15), 5661-5673, 2005.

1701 Johnson, K. S., Zuberi, B., Molina, L. T., Molina, M. J., Iedema, M. J., Cowin, J. P., Gaspar, D. J.,
1702 Wang, C., Laskin, A.: Processing of soot in an urban environment: case study from the Mexico City
1703 Metropolitan Area, *Atmos. Chem. Phys.*, 5, 3033-3043, 2005.

1704 Kamphus, M., Ettner-Mahl, M., Klimach, T., Drewnick, F., Keller, L., Cziczo, D. J., Mertes, S.,
1705 Borrmann, S., and Curtius, J.: Chemical composition of ambient aerosol, ice residues and cloud
1706 droplet residues in mixed-phase clouds: single particle analysis during the Cloud and Aerosol
1707 Characterization Experiment (CLACE 6), *Atmos. Chem. Phys.*, 10, 8077-8095, 2010.

1708 Kanakidou, M., J. H. Seinfeld, S. N. Pandis, et al.: Organic aerosol and global climate modelling: a
1709 review, *Atmos. Chem. Phys.*, 5, 1053-1123, doi:10.5194/acp-1055-1053-2005, 2005.

1710 Kassianov, E., Barnard, J. C., Berg, L. K., Long, C. N., and Flynn, C. J.: Shortwave spectral radiative
1711 forcing of cumulus clouds from surface observations, *Geophys. Res. Lett.*, 38,
1712 L07801, doi:10.1029/2010GL046282, 2011.

1713 Kassianov E. I., Flynn, C. J., Ackerman, T. P., and Barnard, J. C.: Aerosol single-scattering albedo
1714 and asymmetry parameter from MFRSR observations during the ARM Aerosol IOP 2003, *Atmos.*
1715 *Chem. Phys.*, 7(12), 3341-3351, 2007.

1716 Kirchstetter, T. W., Novakov, T., and Hobbs, P. V.: Evidence that the spectral dependence of light
1717 absorption by aerosols is affected by organic carbon, *J. Geophys. Res.*, 109, D21208,
1718 doi:10.1029/22004JD004999, 2004.

1719 Kleinman, L. I., Daum, P. H., Lee, Y.-N., Senum, G., Springston, S. R., Wang, J., Berkowitz, C., Hubbe,
1720 J., Zaveri, R. A., Brechtel, F. J., Jayne, J. T., and Onasch, T. B.: Aircraft observations of aerosol
1721 composition in New England and Mid-Atlantic States during the summer 2002 NEAQS Field
1722 Campaign, *J. Geophys. Res.*, 112, D09310, doi:10.1029/2006JD007786, 2007.

1723 Knobelspiesse, K., Cairns, B., Ottaviani, M., Ferrare, R., Hair, J., Hostetler, C., Obland, M., Rogers,
1724 R., Redemann, J., Shinozuka, Y., Clarke, A., Freitag, S., Howell, S., Kapustin, V., and McNaughton, C.:
1725 Combined retrievals of boreal forest fire aerosol properties with a polarimeter and lidar, *Atmos.*
1726 *Chem. Phys.*, doi:10.5194/acp-11-7045-2011, 2011.

1727 Kondo, Y., Sahu, L., Moteki, N., Khan, F., Takegawa, N., Liu, X., Koike, M., and Miyakawa, T.:
1728 Consistency and traceability of black carbon measurements made by laser-induced incandescence,

1729 thermal-optical transmittance, and filter-based photo-absorption techniques, *Aerosol Sci.*
1730 *Technol.*, 45(2), 295-312. doi: 10.1080/02786826.2010.533215, 2011.

1731 Kroll, J. H., Seinfeld, J. H.: Chemistry of secondary organic aerosol: Formation and evolution of low-
1732 volatility organics in the atmosphere, *Atmos. Environ.*, 42, (16), 3593-3624, 2008.

1733 Kulkarni, P., and Wang, J.: New fast integrated mobility spectrometer for real-time measurement
1734 of aerosol size distribution: II. Design, calibration, and performance characterization, *J. Aerosol*
1735 *Sci.*, 37(10), 1326-1339, 2006.

1736 Kuwata, M., Kondo, Y., Mochida, M., Takegawa, N., and Kawamura, K., Dependence of CCN activity
1737 of less volatile particles on the amount of coating observed in Tokyo, *J. Geophys. Res.*, 112,
1738 D11207, doi:10.1029/2006JD007758, 2007.

1739 Lack, D. A., Lovejoy, E. R., Baynard, T., Pettersson, A., and Ravishankara, A. R.: Aerosol absorption
1740 measurement using photoacoustic spectroscopy: Sensitivity, calibration, and uncertainty
1741 developments, *Aerosol Sci. Technol.*, 40, 697-708, 2006.

1742 Lack, D. A., Cappa, C. D., Covert, D. S., Baynard, T., Massoli, P., Sierau, B., Bates, T. S., Quinn, P. K.,
1743 Lovejoy, E. R., and Ravishankara, A. R.: Bias in filter-based aerosol light absorption measurements
1744 due to organic aerosol loading: Evidence from ambient measurements, *Aerosol Sci. Technol.*, 42,
1745 1033–1041, doi:10.1080/02786820802389277, 2008.

1746 Laborde, M., Schnaiter, M., Linke, C., Saathoff, H., Naumann, K.-H., Möhler, O., Berlenz, S.,
1747 Wagner, U., Taylor, J. W., Liu, D., Flynn, M., Allan, J. D., Coe, H., Heimerl, K., Dahlkötter, F.,
1748 Weinzierl, B., Wollny, A. G., Zanatta, M., Cozic, J., Laj, P., Hitzenberger, R., Schwarz, J. P., and
1749 Gysel, M.: Single Particle Soot Photometer intercomparison at the AIDA chamber, *Atmos. Meas.*
1750 *Technol. Discuss.*, 5, 3519-3573, doi:10.5194/amtd-5-3519-2012, 2012.

1751 Langford, A. O., Senff, C. J., Alvarez II, R. J., Banta, R. M., Hardesty, R. M., Parrish, D. D., Ryerson, T.
1752 B.: Comparison between the TOPAZ airborne ozone lidar and in situ measurements during TexAQS
1753 2006, *J. Atmos. Oceanic Technol.*, doi:10.1175/JTECH-D-10-05043.1, 2011.

1754 Langridge, J. M., Richardson, M. S., Lack, D., Law, D., and Murphy, D. M.: Aircraft instrument for
1755 comprehensive characterization of aerosol optical properties, Part I: Wavelength-dependent
1756 optical extinction and its relative humidity dependence measured using cavity ringdown
1757 spectroscopy, *Aerosol Sci. Technol.*, 45, 1305-1318, 2011.

1758 Laskin, A., Cowin, J. P., and Iedema, M. J.: Analysis of individual environmental particles using
1759 modern methods of electron microscopy and X-ray microanalysis, *J. Electron Spectroscopy*, 150,
1760 260-274, 2006.

1761 Laskin, A.: *Electron Beam Analysis and Microscopy of Individual Particles, Fundamentals and*
1762 *Applications in Aerosol Spectroscopy*, edited by: Signorell, R., and Reid, J. P., CRC Press Taylor and
1763 Francis Group, Boca Raton, 2010.

1764 Laskin, A., Moffet, R. C., Gilles, M. K., Fast, J. D., Zaveri, R. A., Wang, B., Nigge, P., and
1765 Shutthanandan, J.: Tropospheric chemistry of internally mixed sea salt and organic particles:
1766 Surprising reactivity of NaCl with weak organic acids, *J. Geophys. Res.*, doi:10.1029/2012JD017743,
1767 in press, 2012.

1768 Lee-Taylor, J., Madronich, S., Aumont, B., Camredon, M., Hodzic, A., Tyndall, G.S., Apel, E., and
1769 Zaveri, R.A.: Explicit modeling of organic chemistry and secondary organic aerosol partitioning for
1770 Mexico City and its outflow plume, *Atmos. Chem. Phys. Discuss.*, 11, 17013-17070, 2011.

1771 Li, J., M. Pósfai, P. V. Hobbs, and P. R. Buseck, Individual aerosol particles from biomass burning in
1772 southern Africa: 2. Compositions and aging of inorganic particles, *J. Geophys. Res.*, 108(D13), 8484,
1773 doi:10.1029/2002JD002310, 2003.

1774 Liggio, J., Li, S. M., McLaren, R.: Heterogeneous reactions of glyoxal on particulate matter:
1775 Identification of acetals and sulfate esters, *Environ. Sci. Technol.*, 39(6), 1532-1541, 2005.

1776 Lesins, G., Chylek, P., and Lohmann, U.: A study of internal and external mixing scenarios and its
1777 effect on aerosol optical properties and direct radiative forcing, *J. Geophys. Res.*, 107(D10), 4094,
1778 doi:10.1029/2001JD000973, 2002.

1779 Levy, H., Schwarzkopf, M. D., Horowitz, L., Ramaswamy, V., and Findell, K. L.: Strong sensitivity of
1780 late 21st century climate to projected changes in short-lived air pollutants, *J. Geophys. Res.*, 113,
1781 D06102, doi:10.1029/2007JD009176, 2008.

1782 Lewis, K., Arnott, W. P., Moosmuller, H., and Wold, C. E.: Strong spectral variation of biomass
1783 smoke light absorption and single scattering albedo observed with a novel dual wavelength
1784 photoacoustic instrument, *J. Geophys. Res.*, 113, D16203, doi:10.1029/2007JD009699, 2008.

1785 Limbeck, A., Kulmala, M., and Puxbaum, H.: Secondary organic aerosol formation in the
1786 atmosphere via heterogeneous reaction of gaseous isoprene on acidic particles, *Geophys. Res.
1787 Lett.*, 30, 1996, doi:10.1029/2003GL017738, 2003.

1788 Lukacs, H., Gelencser, A., Hammer, S., Puzbaum, H., Pio, C., Legrand, M., Kasper-Giebl, A., Handler,
1789 M., Limbeck, A., Simpson, D., and Preunkert, S.: Seasonal trends and possible sources of brown
1790 carbon based on 2-year aerosol measurements at six sites in Europe, *J. Geophys. Res.*, 112,
1791 D23S18, doi:10.1029/2006JD008151, 2007.

1792 Marley, N. A., Gaffney, J. S., Tackett, M., Sturchio, N. C., Heraty, L., Martinez, N., Hardy, K. D.,
1793 Marchany-Rivera, A., Guilderson, T., MacMillan, A., and Steelman, K.: The impact of biogenic
1794 carbon sources on aerosol absorption in Mexico City, *Atmos. Chem. Phys.*, 9, 1537–1549,
1795 doi:10.5194/acp-9-1537-2009, 2009.

1796 Martins, J. V., Artaxo, P., Liousse, C., Reid, J. S., Hobbs, P. V., and Kaufman, Y. J.: Effects of black
1797 carbon content, particle size, and mixing on light absorption by aerosols from biomass burning in
1798 Brazil, *J. Geophys. Res.*, 103(D4), 32041–32050, 1998.

1799 Medina, J., Nenes, A., Sotiropoulou, R.-E. P., Cottrell, L. D., Ziemba, L. D., Beckman, P. J., and
1800 Griffin, R. J.: Cloud condensation nuclei closure during the International Consortium for
1801 Atmospheric Research on Transport and Transformation 2004 campaign: Effects of size-resolved
1802 composition, *J. Geophys. Res.*, 112, D10S31, doi:10.1029/ 2006JD007588, 2007.

1803 Mochida, M., Kuwata, M., Miyakawa, T., Takegawa, N., Kawamura, K., and Kondo, Y.: Relationship
1804 between hygroscopicity and cloud condensation nuclei activity for urban aerosols in Tokyo, *J.
1805 Geophys. Res.*, 111, D23204, doi:10.1029/2005JD006980, 2006.

1806 Moffet, R. C. and Prather, K. A.: Extending ATOFMS measurements to include refractive index and
1807 density. *Analytical Chemistry* 77:6535-6541, 2005.

1808 Moffet, R. C., Tivanski, A. V., Gilles, M. K.: "Scanning Transmission X-ray Microscopy" in
1809 Fundamentals and Applications in Aerosol Spectroscopy, Eds. R. Signorell and J. Reid, CRC Press
1810 Taylor and Francis Group, Boca Raton, FL, 419–462, 2010a.

1811 Moffet, R. C., Henn, T., Laskin, A., and Gilles, M. K.: Automated chemical analysis of internally
1812 mixed aerosol particles using X-ray spectromicroscopy at the carbon K-edge, *Analytical Chemistry*,
1813 82, 7906–7914, doi:10.1021/ac1012909, 2010b.

1814 Moffet, R. C., Henn, T. R., Tivanski, A. V., Hopkins, R. J., Desyaterik, Y., Kilcoyne, A. L. D., Tyliczszak,
1815 T., Fast, J., Barnard, J., Shutthanandan, V., Cliff, S. S., Perry, K. D., Laskin, A., and Gilles, M. K.:
1816 Microscopic characterization of carbonaceous aerosol particle aging in the outflow from Mexico
1817 City, *Atmos. Chem. Phys.*, 10, 961–976, 2010c.

1818 Moffet, R. C., Furutani, H. F., Rodel, T., Henn, T., Sprau, P. O., Prakash, S., Laskin, A., Uematsu, M.,
1819 and Gilles, M. K.: Iron speciation and mixing in single aerosol particles from the Asian continental
1820 outflow, *J. Geophys. Res.*, 117, D07204, doi:10.1029/2011JD016746, 2012.

1821 Molina, L. T., Madronich, S., Gaffney, J. S., Apel, E., de Foy, B., Fast, J., Ferrare, R., Herndon, S.,
1822 Jimenez, J. L., Lamb, B., Osornio-Vargas, A. R., Russell, P., Schauer, J. J., Stevens, P. S., Volkamer, R.,
1823 and Zavala, M.: An overview of the MILAGRO 2006 Campaign: Mexico City emissions and their
1824 transport and transformation, *Atmos. Chem. Phys.*, 10, 8697–8760, 2010.

1825 Moteki N., and Kondo, Y.: Method to measure time-dependent scattering cross-sections of
1826 particles evaporating in a laser beam, *J. Aerosol Sci.* 39 348–364. doi:10.1029/2006JD007076, 2008.

1827 Mukai, H. and Ambe, Y.: Characterization of a humic acid-like brown substance in airborne
1828 particulate matter and tentative identification of its origin, *Atmos. Environ.*, 20, 813–819, 1986.

1829 Murphy, D. M.: The design of single particle laser mass spectrometers, *Mass Spectrometry*
1830 *Reviews*, 26, 150–165, 2005.

1831 Murphy, D. M., Cziczo, D. J., Hudson, P. K., Schein, M. E., and Thomson, D. S.: Particle density
1832 inferred from simultaneous optical and aerodynamic diameters sorted by composition. *J. Aerosol*
1833 *Sci.*, 35, 135–139, 2004.

1834 Murphy, D. M., Thomson, D. S., Mahoney, T. M. J.: In situ measurements of organics, meteoritic
1835 material, mercury, and other elements in aerosols at 5 to 19 kilometers, *Science*, 282, 1664–1669,
1836 1998.

1837 Nizkorodov, S. A., Laskin, J., and Laskin, A.: Molecular chemistry of organic aerosols through
1838 applications of the high resolution mass spectrometry, *Phys. Chem. Chem. Phys.*, 13, 3612–3629,
1839 doi:10.1039/C0CP02032J, 2011.

1840 Noziere, B., and Esteve, W.: Organic reactions increasing the absorption index of atmospheric
1841 sulfuric acid aerosols, *J. Geophys. Res.*, 32, L03812, doi:10.1029/2004GL021942, 2005.

1842 Noziere, B., Dziedzic, P., and Cordova, A.: Formation of secondary light-absorbing "fulvic-like"
1843 oligomers: A common process in aqueous and ionic atmospheric particles?, *Geophys. Res. Lett.*, 34,
1844 L21812, doi:10.1029/22007GL031300, 2007.

1845 Noziere, B., Dziedzic, P., and Cordova, A.: Products and kinetics of the liquid-phase reaction of
1846 glyoxal catalyzed by ammonium ions (NH₄⁺), *J. Phys. Chem. A*, 113, 231–237, 2009.

1847 Müller, D., Ansmann, A., Mattis, I., Tesche, M., Wandinger, U., Althausen, D., and Pisani, G.:
1848 Aerosol-type-dependent lidar ratios observed with Raman lidar, *J. Geophys. Res.*, 112, D16202,
1849 doi:10.1029/2006JD008292, 2007.

1850 Ogren, J.: Comment on “Calibration and intercomparison of filter-based measurements of visible
1851 light absorption by aerosols,” *Aerosol Sci. Technol.*, 44, 589–591,
1852 doi:10.1080/02786826.2010.482111, 2010.

1853 Olfert, J., Kulkarni, P. S., and Wang, J.: Measurements of particle size distributions using a Fast
1854 Integrated Mobility Spectrometer, *J. Aerosol Sci.*, 39, 940-956, doi:10.1016/j.jaerosci.2008.06.005,
1855 2008.

1856 Ottaviani, M., Cairns, B., Chowdhary, J., Van Diedenhoven, B., Knobelspiesse, K., Hostetler, C.,
1857 Ferrare, R., Burton, S., Hair, J., Obland, M. D., Rogers, R.: Polarimetric retrievals of surface
1858 properties in the region affected by the Deepwater Horizon oil spill, *Remote Sens. Environ.*, 121,
1859 389-403, 2011.

1860 Pearson, G., Davies, F., and Collier, C.: An Analysis of the Performance of the UFAM Pulsed Doppler
1861 Lidar for Observing the Boundary Layer, *J. Atmos. Oceanic Technol.*, 26, 240-250, 2009.

1862 Pratt, K. A., Mayer, J. E., Holecek, J.C., Moffet, R. C., Sanchez, R. O., Rebotier, T. P., Furutani, H.,
1863 Gonin, M., Fuhrer, K., Su, Y., Guazzotti, S., and Prather, K. A.: Development and Characterization of
1864 an Aircraft Aerosol Time-of-Flight_Mass Spectrometer, *Anal. Chem.*, 81, 1792-1800, 2009.

1865 Pratt, K. A., Twohy, C. H., Murphy, S. M., Moffet, R. C., Heymsfield, A. J., Gaston, C. J., DeMott, P. J.,
1866 Field, P. R., Henn, T. R., Rogers, D. C., Gilles, M. K., Seinfeld, J. H., and Prather, K. A.: Observation of
1867 playa salts as nuclei in orographic wave clouds, *J. Geophys. Res.*, 115, D15301, 2010.

1868 Radney, J. G., Bazargan, M. H., Wright, M. E., and Atkinson, D. B.: Laboratory validation of aerosol
1869 extinction coefficient measurements by a field-deployable pulsed cavity ring-down
1870 transmissometer, *Aerosol Sci. Technol.*, 43, 71-80, 10.1080/02786820802482536, 2009.

1871 Ramanathan, V., Crutzen, P. J., Lelieveld, J., Mitra, A. P., Althausen, D., Anderson, J., Andreae, M.
1872 O., Cantrell, W., Cass, G. R., Chung, C. E., Clarke, A. D., Coakley, J. A., Collins, W. D., Conant, W. C.,
1873 Dulac, F., Heintzenberg, J., Heymsfield, A. J., Holben, B., Howell, S., Hudson, J., Jayaraman, A.,
1874 Kiehl, J. T., Krishnamurti, T. N., Lubin, D., McFarquhar, G., Novakov, T., Ogren, J. A., Podgorny, I. A.,
1875 Prather, K., Priestley, K., Prospero, J. M., Quinn, P. K., Rajeev, K., Rasch, P., Rupert, S., Sadourny, R.,
1876 Satheesh, S. K., Shaw, G. E., Sheridan, P., and Valero, F. P. J.: Indian Ocean experiment: An
1877 integrated analysis of the climate forcing and effects of the great Indo-Asian haze, *J. Geophys.*
1878 *Res.*, 106(D22), 28,371-28,398, doi:10.1029/2001JD900133, 2001.

1879 Riemer, N., West, M., Zaveri, R. A., and Easter, R. C.: Simulating the evolution of soot mixing state
1880 with a particle-resolved aerosol model, *J. Geophys. Res.*, 114, D09202, doi:10.1029/2008JD011073,
1881 2009.

1882 Roach, P. J., Laskin, A., and Laskin, J.: Molecular characterization of organic aerosols using
1883 nanospray desorption electrospray ionization mass spectrometry, *Anal. Chem.*, 82, 7979-7986,
1884 2010.

1885 Robinson, A. L., Donahue, N. M., Shrivastava, M. K., Weitkamp, E. A., Sage, A. M., Grieshop, A. P.,
1886 Lane, T. E., Pierce, J. R., and Pandis, S. N.: Rethinking organic aerosols: Semivolatile emissions and
1887 photochemical aging, *Science*, 315, 1259-1262, 2007.

1888 Rogers, R. R., Hair, J. W., Hostetler, C. A., Ferrare, R. A., Obland, M. D., Cook, A. L., Harper, D. B.,
1889 Burton, S. P., Shinzuka, Y., McNaughton, C. S., Clarke, A. D., Redemann, J., Russell, P. B.,
1890 Livingston, J. M., and Kleinman, L. I.: NASA LaRC airborne high spectral resolution lidar aerosol
1891 measurements during MILAGRO: observations and validation, *Atmos. Chem. Phys.*, 9, 4811-4826,
1892 doi:10.5194/acp-9-4811-2009, 2009.

1893 Saathoff, H., Naumann, K. -H., Schnaiter, M., Schöck, W., Möhler, O., Schurath, U., Weingartner, E.,
1894 Gysel, M., Baltensperger, U.: Coating of soot and (NH₄)₂SO₄ particles by ozonolysis products of α-
1895 pinene, *J. Aerosol Sci.*, 34, 1297-1321, 2003.

1896 Sareen, N., Schwier, A. N., Shapiro, E. L., Mitroo, D., and McNeil, V. F.: Secondary organic material
1897 formed by methylglyoxal in aqueous aerosol mimics, *Atmos. Chem. Phys.*, 10, 997–1016,
1898 doi:10.5194/acp-10-997-2010, 2010.

1899 Seinfeld, J. H., and Pandis, S.N.: *Atmospheric Chemistry and Physics: From Air Pollution to Climate*
1900 *Change*, John Wiley, Hoboken, N.J., 1998.

1901 Schnaiter, M., Linke, C., Möhler, O., Naumann, K.-H., Saathoff, H., Wagner, R., Schurath, U., and
1902 Wehner, B.: Absorption amplification of black carbon internally mixed with secondary organic
1903 aerosol, *J. Geophys. Res.*, 110, D19204, doi:10.1029/2005JD006046, 2005.

1904 Schwarz, J. P., et al.: Coatings and their enhancement of black carbon light absorption in the
1905 tropical atmosphere, *J. Geophys. Res.*, 113, D03203, doi:10.1029/2007JD009042, 2008a.

1906 Schwarz, J. P., et al.: Measurement of the mixing state, mass, and optical size of individual black
1907 carbon particles in urban and biomass burning emissions, *Geophys. Res. Lett.*, 35, L13810,
1908 doi:10.1029/2008GL033968, 2008b.

1909 Schwarz, J. P., et al.: Single-particle measurements of midlatitude black carbon and light-scattering
1910 aerosols from the boundary layer to the lower stratosphere, *J. Geophys. Res.* 111:D16207.
1911 doi:10.1029/2006JD007076, 2006.

1912 Shapiro, E. L., Szprengiel, J., Sareen, N., Jen, C. N., Giordano, M. R., and McNeill, V. F.: Light-
1913 absorbing secondary organic material formed by glyoxal in aqueous aerosol mimics, *Atmos. Chem.*
1914 *Phys.*, 9, 2289–2300, doi:10.5194/acp-9-2289-2009, 2009.

1915 Sem, G. J.: Design and performance characteristics of three continuous-flow condensation particle
1916 counters: a summary, *Atmospheric Research*, 62(3-4), 267-294, DOI: 10.1016/S0169-
1917 8095(02)00014-5, 2002.

1918 Sinreich, R., Coburn, S., Dix, B., and Volkamer, R.: Ship-based detection of glyoxal over the remote
1919 tropical Pacific Ocean, *Atmos. Chem. Phys.*, 10, 11359–11371, doi:10.5194/acp-10-11359-2010,
1920 2010.

1921 Slowik, J. G., Stroud, C., Bottenheim, J. W., Brickell, P. C., Chang, R. Y. W., Liggio, J., Makar, P. A.,
1922 Martin, R. V., Moran, M. D., Shantz, N. C., Sjostedt, S. J., van Donkelaar, A., Vlasenko, A., Wiebe, H.
1923 A., Xia, A. G., Zhang, J., Leaitch, W. R., and Abbatt, J. P. D.: Characterization of a large biogenic

1924 secondary organic aerosol event from eastern Canadian forests, *Atmos. Chem. Phys.*, 10, 2825-
1925 2845, doi:2810.5194/acp-2810-2825-2010, 2010.

1926 Smith, J. D., and Atkinson, D. B.: A portable pulsed cavity ring-down transmissometer for
1927 measurement of the optical extinction of the atmospheric aerosol, *Analyst*, 126, 1216-1220, 2001.

1928 Song, C., Zaveri, R. A., Alexander, M. L., Thornton, J. A., Madronich, S., Ortega, J. V., Zelenyuk, A.,
1929 Yu, X.-Y., Laskin, A., and Maughan, D.: Effect of hydrophobic primary organic aerosol on secondary
1930 organic aerosol formation from ozonolysis of α -pinene, *Geophys. Res. Lett.*, 34, L20803,
1931 doi:10.1029/2007GL030720, 2007.

1932 Sorooshian, A. , Brechtel, F. J., Ma, Y., Weber, R. J., Corless, A., Flagan, R. C., and Seinfeld, J. H.:
1933 Modeling and Characterization of a Particle-into-Liquid Sampler (PILS), *Aerosol Sci. Technol.*, 40(6),
1934 396-409, doi:10.1080/02786820600632282, 2006.

1935 Spencer, M. T., Shields, L. G. and Prather, K A.: Simultaneous measurement of the effective density
1936 and chemical composition of ambient aerosol particles, *Environ. Sci. Technol.*, 41, 1303-1309,
1937 2007.

1938 Springston, S. R., Kleinman, L. I., Nunnermacker, L. J., Brechtel, F., Lee, Y. -N., and Wang, J.:
1939 Chemical evolution of an isolated power plant plume during the TexAQs 2000 study. *Atmos.*
1940 *Environ.*, 39, 3431-3443, 2005.

1941 Stephens, M., Turner, N., and Sandberg, J.: Particle identification by laser-induced incandescence
1942 in a solid-state laser cavity, *Applied Optics*. 42(19):3726–3736, 2003.

1943 Steiner, A. L., Cohen, R. C., Harley, R. A., Tonse, S., Millet, D. B., Schade, G. W., Goldstein, A. H.:
1944 VOC reactivity in central California: Comparing an air quality model to ground-based
1945 measurements, *Atmos. Chem. Phys.*, 8(2), 351-368, 2008.

1946 Stull, R. B.: *An Introduction to Boundary Layer Meteorology*, Kluwer, Boston, 1988.

1947 Subramanian, R., Kok, G. L., Baumgardner, D., Clarke, A., Shinozuka, Y., Campos, T. L., Heizer, C. G.,
1948 Stephens, B. B., de Foy, B., Voss, P. B., and Zaveri, R. A.: Black carbon over Mexico: the effect of
1949 atmospheric transport on mixing state, mass absorption cross-section, and BC/CO ratios, *Atmos.*
1950 *Chem. Phys.* 219-237, 2010.

1951 Sugimoto, N., and Lee, C.H.: Characteristics of dust aerosols inferred from lidar depolarization
1952 measurements at two wavelengths, *Appl. Optics*, 45(28), 7468-7474, 2006.

1953 Surratt, J. D., et al.: Organosulfate formation in biogenic secondary organic aerosol, *J. Phys. Chem.*
1954 *A*, 112(36), 8345-8378, 2008.

1955 Surratt, J. D., et al.: Reactive intermediates revealed in secondary organic aerosol formation from
1956 isoprene, *Proc. Natl. Acad. Sci. U. S. A.*, 107(15), 6640-6645, 2010.

1957 Tritscher, T., et al.: Changes of hygroscopicity and morphology during ageing of diesel soot,
1958 *Environ. Res. Lett.*, 6, 034026, doi:10.1088/1748-9326/6/3/034026, 2011.

1959 Warneke, C., et al.: An important contribution to springtime Arctic aerosol from biomass burning
1960 in Russia, *Geophys. Res. Lett.*, 37, Doi 10.1029/2009gl041816, 2010.

1961 Ulbrich, I., Canagratna, M., Zhang, Q., Worsnop, D.R., and Jimenez, J.L.: Interpretation of organic
1962 components from positive matrix factorization of aerosol mass spectrometric data, *Atmos. Chem.*
1963 *Phys.*, 9, 2891-2918, 2009.

1964 Vaden, T. D., Imre, D., Beranek, J., Shrivastava, M. and Zelenyuk, A.: Evaporation kinetics and
1965 phase of laboratory and ambient secondary organic aerosol, *Proc. Natl. Acad. Sci. U. S. A.*
1966 108:2190-2195, 2011a.

1967 Vaden, T. D., Imre, D., Beranek, J. and Zelenyuk, A.: Extending the capabilities of single particle
1968 mass spectrometry: I. Measurements of aerosol number concentration, size distribution, and
1969 asphericity, *Aerosol Sci. Technol.*, 45, 113-124, 2011b.

1970 Vaden, T. D., Imre, D., Beranek, J. and Zelenyuk, A.: Extending the capabilities of single particle
1971 mass spectrometry: II. Measurements of aerosol particle density without DMA, *Aerosol Sci.*
1972 *Technol.*, 45, 125-135, 2011c.

1973 Virtanen, A., Joutsensaari, J., Koop, T., Kannosto, J., Yli-Pirila, P., Leskinen, J., Makela, J. M.,
1974 Holopainen, J. K., Poschl, U., Kulmala, M., Worsnop, D. R. and Laaksonen, A.: An amorphous solid
1975 state of biogenic secondary organic aerosol particles, *Nature*, 467, 824-827, 2010.

1976 Volkamer, R., Jimenez, J. L., San Martini, F., Dzepina, K., Zhang, Q., Salcedo, D., Molina, L. T.,
1977 Worsnop, D. R., and Molina, M. J.: Secondary organic aerosol formation from anthropogenic air
1978 pollution: Rapid and higher than expected, *Geophys. Res. Lett.*, 33, L17811,
1979 doi:10.1029/2006GL026899, 2006.

1980 Volkamer, R., Coburn, S., Dix, B., and Sinreich, R.: MAX-DOAS observations from ground, ship, and
1981 research aircraft: maximizing signal-to-noise to measure "weak" absorbers, in: *SPIE Proceedings*
1982 *Ultraviolet and Visible Ground- and Space-based Measurements, Trace Gases, Aerosols and*
1983 *Effects*, San Diego, 2–9 August 2009, 746203, doi:10.1117/12.826792, 2009.

1984 Waquet, F., B. Cairns, K. Knobelspiesse, J. Chowdhary, L.D. Travis, B. Schmid, and M.I.
1985 Mishchenko,: Polarimetric remote sensing of aerosols over land, *J. Geophys. Res.*, 114, D01206,
1986 doi:10.1029/2008JD010619, 2009.

1987 Warneke, C., et al.: An important contribution to springtime Arctic aerosol from biomass burning
1988 in Russia, *Geophys. Res. Lett.*, 37, L01801, doi:10.1029/2009GL041816, 2010.

1989 Weber, R. J., Sullivan, A. P., Peltier, R. E., Russell, A., Yan, B., Zheng, M., Gouw, J. A. d., Warneke, C.,
1990 Brock, C., Holloway, J. S., Atlas, E. L., and Edgerton, E.: A study of secondary organic aerosol
1991 formation in the anthropogenic influenced southeastern United States, *J. Geophys. Res.*, 112,
1992 D13302, doi:10.1029/12007JD008408, 2007.

1993 Wentzel, M., Gorzawski, H., Naumann, K. H., Saathoff, H., and Weinbruch, S.: Transmission
1994 electron microscopical and aerosol dynamical characterization of soot aerosols, *J. Aerosol Sci.*, 34,
1995 1347–1370, 2003.

1996 Wexler, A. S., and Seinfeld, J.H.: Second-generation inorganic aerosol model, *Atmos. Environ.*, 25A,
1997 2731– 2748, 1991.

1998 Zaveri, R. A., Easter, R. C., Fast, J. D., and Peters, L. K.: Model for Simulating Aerosol Interactions
1999 and Chemistry (MOSAIC), *J. Geophys. Res.*, 113, D13204, doi:10.1029/2007JD008782, 2008.

2000 Zaveri, R. A., Berkowitz, C. M., Brechtel, F. J., Gilles, M. K., Hubbe, J. M., Jayne, J. T., Kleinman, L. I.,
2001 Laskin, A., Madronich, S., Onasch, T. B., Pekour, M., Springston, S. R., Thornton, J. A., Tivanski, A.
2002 V., and Worsnop, D. R.: Nighttime chemical evolution of aerosol and trace gases in a power plant
2003 plume: Implications for secondary organic nitrate and organosulfate aerosol formation, NO₃
2004 radical chemistry, and N₂O₅ heterogeneous hydrolysis, *J. Geophys. Res.*, 115, D12304,
2005 doi:10.1029/2009JD013250, 2010a.

2006 Zaveri, R. A., Barnard, J. C., Easter, R. C., Riemer, N., West, M.: Particle-resolved simulation of
2007 aerosol size, composition, mixing state, and the associated optical and cloud condensation nuclei
2008 activation properties in an evolving urban plume, *J. Geophys. Res.*, 115, D17210,
2009 doi:10.1029/2009JD013616, 2010b.

2010 Zelenyuk, A., and Imre, D.: Single particle laser ablation time-of-flight mass spectrometer: An
2011 introduction to SPLAT, *Aerosol Science and Technology*, 39, 554-568, 2005.

2012 Zelenyuk, A., Imre, D., Han, J. H. and Oatis, S.: Simultaneous measurements of individual ambient
2013 particle size, composition, effective density, and hygroscopicity, *Analytical Chemistry*, 80, 1401-
2014 1407, 2008.

2015 Zelenyuk, A., and Imre, D.: Beyond single particle mass spectrometry: multidimensional
2016 characterisation of individual aerosol particles, *Int. Rev. Phys. Chem.*, 28, 309-358, 2009a.

2017 Zelenyuk, A., Yang, J., Choi, E., and Imre, D.: SPLAT II: An aircraft compatible, ultra-sensitive, high
2018 precision instrument for in-situ characterization of the size and composition of fine and ultrafine
2019 particles, *Aerosol Sci. Technol.*, 43, 411-424, 2009b.

2020 Zelenyuk, A., Imre, D., Earle, M., Easter, R., Korolev, A., Leitch, R., Liu, P., Macdonald, A. M.,
2021 Ovchinnikov, M., and Strapp, W.: In situ characterization of cloud condensation nuclei, interstitial,
2022 and background particles using the single particle mass spectrometer, SPLAT II, *Analytical
2023 Chemistry*, 82, 7943-7951, 2010.

2024 Zhang, Q., Alfarra, M. R., Worsnop, D. R., Allan, J. D., Coe, H., Canagaratna, M. R., and Jimenez, J.
2025 L.: Deconvolution and quantification of hydrocarbon-like and oxygenated organic aerosols based
2026 on aerosol mass spectrometry, *Environ. Sci. Technol.*, 39(13), 4938-4952,
2027 doi:4910.1021/es048568l, 2005.

2028 Zhang, Q., Jimenez, J. L., Canagaratna, M. R., et al.: Ubiquity and dominance of oxygenated species
2029 in organic aerosols in anthropogenically-influenced Northern Hemisphere mid-latitudes, *Geophys.
2030 Res. Lett.*, 34, L13801, doi:10.1029/2007GL029979, 2007.

2031 Zhang, Q., Jimenez, J. L., Canagaratna, M., Ng, N. L., Ulbrich, I., Worsnop, D., and Sun, Y. L.:
2032 Understanding organic aerosols via factor analysis of aerosol mass spectrometry: a review, *Anal.
2033 Bioanal. Chem.*, doi:10.1007/s00216-00011-05355-y, 2011.

2034 Zhang, R., Khalizov, A. F., Pagels, J., Zhang, D., Xue, H., and McMurry, P. H.: Variability in
2035 morphology, hygroscopicity, and optical properties of soot aerosols during atmospheric
2036 processing, *Proc. Natl. Acad. Sci. U. S. A.*, 105(30), 10291-10296, 2008.

2037

Table 1. Measurements and Instruments at the T0 and T1 Ground Sites.

| Measurement | T0 | T1 | Instrument/Technique | Avg. Time | Accuracy | DL | PI (Institution) |
|--|----|----|---|----------------------|----------|--|---|
| Meteorology | | | | | | | |
| Wind profile | | • | Wind Profiler, Sodar | | | | Berg (PNNL) |
| Temperature, RH profile | • | • | Radiosonde | | | | Berg (PNNL) |
| Temperature | | | | | 0.3 °C | | |
| Pressure | | | | | 0.5 mbar | | |
| Relative humidity | • | • | Vaisala WXT-510 | 1 min | 3% | | T0: Jobson (WSU) T1: Berg (PNNL) |
| Wind speed | | | | | 0.3 m/s | | |
| Wind direction | | | | | 3 deg | | |
| Trace Gases | | | | | | | |
| VOCs | • | • | Ionikon PTR-MS | | | | T0: Jobson (WSU) T1: Knighton (MSU) |
| SVOCs | • | | GC-ITMS | | | | Jobson (WSU) |
| Formaldehyde | | • | CU GMAX-DOAS | 15 min | 10% | 2x10 ¹⁵ a 3x10 ¹⁴ a | Volkamer (CU Boulder) |
| Glyoxal | | • | | | | | |
| CO | • | • | T0: VUV fluorescence T1: Teledyne Model 300U | 1 min 1 min | 2% | 5 ppbv | T0: Jobson (WSU) T1: Dubey (LANL) |
| CO ₂ - CH ₄ - H ₂ O | | • | Picarro Cavity Ringdown | | | | Dubey (LANL) |
| O ₃ | • | • | UV absorption | 1 min | 10% | 3 ppbv | T0: Jobson (WSU) T1: Dubey (LANL) |
| NO | • | • | Chemiluminescence | 2 min | 2% | 5 pptv | T0: Jobson (WSU) T1: Dubey (LANL) |
| NO ₂ | • | • | Photolytic conversion CU GMAX-DOAS | 2 min 15 min | 5% 5% | 5 pptv 5x10 ¹⁴ a | T0: Jobson (WSU) T1: Volkamer (CU Boulder) |
| NO _y | • | • | Mo converter | 2 min | 5% | 5 pptv | T0: Jobson (WSU) T1: Dubey (LANL) |
| SO ₂ | • | | Thermo Model 43i | 1 min | 5% | 1 ppbv | Song (PNNL) |
| Aerosol Size & Comp. | | | | | | | |
| Size distribution | • | • | SMPS + CPC: 12.2 nm – 710 nm SMPS + CPC: 8.75 – 858 nm | 2.5 min 5 min | 3% | | T0: Song (PNNL) T1: Zhang (UC Davis) |
| Size distribution | • | • | TSI APS: 520 – 20000 nm | 1 min | | | T0: Jobson (WSU) T1: Pekour (PNNL) |
| Number Concentration | • | • | TSI CPC-3010 | 1 min | | | Pekour (PNNL) |
| Composition, volatility | • | • | HR-ToF-AMS + thermodenuder | 5 min | 30% | Varies by species | T0: Song (PNNL) T1: Zhang (UC Davis) |
| Single particle size, composition, density | • | • | T0: SPLAT II T1: PALMS | | | | T0: Zelenyuk (PNNL) T1: Cziczo (PNNL) |
| Black carbon mass | • | • | DMT SP2 | Particle-by-particle | 35% | 0.3 fg BC | Subramanian (DMT) |
| Water-soluble species | • | • | PILS with autosampler | | | | Zhang (UC Davis) |
| OC/EC | • | • | Sunset OC/EC | 1 h | | | Laulainen (PNNL) |
| Chemical Composition | • | • | TRAC Collector | | | | Laskin (EMSL), Gilles (LBNL) |
| Chemical Composition | • | • | DRUM Sampler | | | | Laskin (EMSL) |
| Aerosol Morphology | • | • | SEM Collector | | | | Mazzoleni (MTU) |
| Aldehydes and polar organics & OC/EC | • | • | Hi-vol Filter | 12 h | 5% | | Kubatova (UND) |
| Radiocarbon | | • | Hi-vol Filter | | | | Gaffney (UArk) |

2039 ^a Vertical Column Density (VCD); detection limit in units of molecule cm⁻².

2040

2041

2042

2043

2044

2045

2046

2047

Table 1. Continued.

| Measurement | T0 | T1 | Instrument/Technique | Avg. Time | Accuracy | DL | PI (Institution) |
|--|----|----|---|-----------|------------------------------------|----------------------|---|
| Radiation | | | | | | | |
| J-NO ₂ | • | | 4 π J-NO ₂ radiometer | 1 s | | | Laulainen (PNNL) |
| Actinic flux | | • | Diode-Array Spectroradiometer | 1 s | | | Laulainen (PNNL) |
| Broadband solar rad flux | • | • | Pyranometer (Eppley PSP) | 1 min | 4% | | Barnard (PNNL) |
| AOD from narrowband solar irradiance | • | • | MFRSR | 20 s | <0.01 | | Barnard (PNNL) |
| Aerosol extinction profiles and AOD from diffuse solar stray light | | • | CU GMAX-DOAS | 15 min | ~ 0.01 | | Volkamer (CU Boulder) |
| Optical Properties | | | | | | | |
| Scattering | • | • | TSI Nephelometer 3563 at 450, 550, 700 nm | 1 min | | 0.3 Mm ⁻¹ | Pekour (PNNL) |
| Absorption | • | • | PSAP at 470, 532, 660 nm | 1 min | | 0.3 Mm ⁻¹ | Pekour (PNNL) |
| Absorption | | • | Athelometer | | | | Sedlacek (BNL) |
| Absorption & scattering | • | • | Photoacoustic instruments T0: 375, 405, 532, 781, 870, 1047 nm T1: 355, 405, 532, 781, 870 nm | | Varies by instrument and λ | | T0, T1: Arnott (UNR) T0, T1: Dubey (LANL) T0: Cappa (UCD) |
| Extinction & scattering | • | • | Cavity Ring-down at 355, 405, 532, 1064 nm | | Varies by instrument and λ | | T0, T1: Atkinson (PSU) T0: Cappa (UCD) |
| Hygroscopic growth | • | • | Humidigraph - f(RH) | | | | T0: Cappa (UCD) T1: Cziczo (PNNL) |
| CCN | • | • | CCN Counter | | | | Cziczo (PNNL) |
| CCN | | • | Size-resolved CCN Counter | | | | Wang (BNL) |

2048

2049

Table 2. Measurements and Instruments aboard the DOE G-1 Aircraft during CARES 2010.

| Measurement | Instrument/Technique | Avg. Time | Accuracy | DL | PI (Institution) |
|--|--|----------------------|-------------------|--|------------------------------|
| Meteorology | | | | | |
| Temperature | Rosemount 102 | 1 s | ±0.5 °C | -50 to 50 °C | Hubbe (PNNL) |
| Dewpoint temperature | General Eastern 1011B chilled-mirror hygrometer | 1 s | ±0.5 °C | -75 to 50 °C | Hubbe (PNNL) |
| Static pressure | Rosemount 1201F1 | 1 s | 3mb | 400 – 1060 mb | Hubbe (PNNL) |
| Gust probe, alpha | All-Sensor 20-inch-G-4V | 0.1 s | 0.125mb | 0 to 50 mb | Senum (BNL) |
| Gust probe, beta | Rosemount 1221S1 | 0.1 s | 0.35mb | 0 to 35 mb | Senum (BNL) |
| Gust probe, dynamic | Rosemount 1221F2 | 1 s | 0.3mb | 0 to 100 mb, -55 to 71 °C | Hubbe (PNNL) |
| Trace Gases | | | | | |
| CO | Resonance Limited VUV-Fluorescence | 1 s | | | Springston (BNL) |
| SO ₂ | TEI 43S | 1 s | | | Springston (BNL) |
| O ₃ | TEI 49-100 | 1 s | | | Springston (BNL) |
| NO, NO ₂ , and NO _y | Research Grade Instruments | 1 s | | | Springston (BNL) |
| VOCs | Ionikon PTR-MS | 3.5 s | Varies by species | Varies by species | Shilling (PNNL) |
| Aerosol Size | | | | | |
| Number conc. > 3 nm | TSI-3025 CPC | 1 s | | 0-10 ⁵ cm ⁻³ | Tomlinson (PNNL) |
| Number conc. > 10 nm | TSI-3010 CPC | 1 s | | 0-10 ⁴ cm ⁻³ | Tomlinson (PNNL) |
| Particle size distribution (PSD): 30 - 70 nm | FIMS | 1 s | | | Wang (BNL) |
| PSD: 60 - 1000 nm | UHSAS-A | 1 s | | 0-7200 cm ⁻³ | Tomlinson (PNNL) |
| PSD: 500 -50,000 nm | CAPS/CAS | 1 s | | | Senum (BNL) |
| Aerosol Composition | | | | | |
| Aerosol composition | HR-ToF-AMS (EMSL) | 13 s | ~30% | 0.1 µg m ⁻³ for org | Shilling (PNNL) |
| Single particle composition and size | ATOFMS | | | | Prather (UCSD) |
| Black carbon mass | DMT SP2 | Particle-by-particle | ~35% | 0.3 fg BC | Sedlacek (BNL) |
| Water soluble aerosol chemical composition | PILS with autosampler | 3 min | Varies by species | 0.02-0.28 µg m ⁻³ background | Zhang (UCD) |
| Aerosol chemical composition | TRAC Collector | | | | Laskin (EMSL), Gilles (LBNL) |
| Optical Properties | | | | | |
| Aerosol light scattering | TSI 3563 Nephelometer at 450, 550, and 700 nm | 1 s | 4-7% | 1–10 ⁴ Mm ⁻¹ | Hubbe (PNNL) |
| Aerosol light absorption | Radiance Research PSAP at 461, 522, and 648 nm | 1 s | 20% | 10 ⁻¹ – 10 ⁴ Mm ⁻¹ (log channel); 0 – 50Mm ⁻¹ (linear channel) | Hubbe (PNNL) |
| Aerosol light absorption and scattering | Photoacoustic spectrometer at 405, 532, and 870 nm | | | | Dubey (LANL) |

2053

Table 3. Measurements and Instruments aboard the NASA B-200 King Air Aircraft during CARES 2010.

| Parameter | Instrument/Technique | Averaging Time | Uncertainty ^a or Accuracy | PI (Institution) |
|---|--------------------------------|------------------------------|--------------------------------------|---------------------------|
| Backscatter ratio (532 nm) | High Spectral Resolution Lidar | 10 s (~1 km) | <5% | Ferrare, Hostetler (NASA) |
| Backscatter coefficient (532 & 1064 nm) | High Spectral Resolution Lidar | 10 s (~1 km) | 0.16 (Mm-sr) ⁻¹ | Ferrare, Hostetler (NASA) |
| Extinction coefficient (532 nm) | High Spectral Resolution Lidar | 1 min (~6 km) | 10 Mm ⁻¹ | Ferrare, Hostetler (NASA) |
| Depolarization | High Spectral Resolution Lidar | 10 s (~1 km) | 0.004 | Ferrare, Hostetler (NASA) |
| Aerosol optical depth | Research Scanning Polarimeter | scene-dependent ^d | 0.02/8% ^b | Cairns (NASA/GISS) |
| Mode effective radius | Research Scanning Polarimeter | scene-dependent ^d | 0.02 μm/10% ^c | Cairns (NASA/GISS) |
| Mode effective variance | Research Scanning Polarimeter | scene-dependent ^d | 0.05/50% ^c | Cairns (NASA/GISS) |
| Real refractive index | Research Scanning Polarimeter | scene-dependent ^d | 0.02 | Cairns (NASA/GISS) |
| Imaginary refractive index | Research Scanning Polarimeter | scene-dependent ^d | 50% | Cairns (NASA/GISS) |

2054 ^aSee [Hair et al. \(2008\)](#) for a description of HSRL aerosol measurement uncertainties.

2055 ^bThe appropriate accuracy is whichever value is larger (i.e. lower accuracy at higher optical depths).

2056 ^cAbsolute accuracy applies to accumulation/fine mode and relative accuracy to coarse.

2057 ^dScan rate is 1.1885 Hz (0.8414 sec), with angular resolution (instrument IFOV) equal to 14 mrad. The time required for
 2058 scene aggregation is defined by the ratio of aircraft speed to target distance (see
 2059 http://data.giss.nasa.gov/rsp_air/specs.html).

2060

2061

Table 4. Measurements and Instruments aboard the NOAA Twin Otter Aircraft during CARES 2010.

| Parameter | Instrument /Technique | Avg. Time | Vertical/Range Resolution | Measurement Precision | Measurement Accuracy | PI (Institution) |
|---|---------------------------------|------------------|----------------------------|---|--|---------------------------|
| Ozone profiles | Differential Absorption Lidar | 10 s (~600 m) | 90 m (smoothed over 450 m) | 5 – 10 % (up to 30% for low SNR) | < 5% (up to 15% for low SNR) | Senff (NOAA / CU Boulder) |
| Aerosol backscatter profiles (300 nm) | Differential Absorption Lidar | 10 s (~600 m) | 6 m | ~ 10 % | < 30 % | Senff (NOAA / CU Boulder) |
| Boundary layer height | Differential Absorption Lidar | 10 s (~600 m) | - | ~ 50 m | ~ 50 m | Senff (NOAA / CU Boulder) |
| Line-of-sight wind speed profiles (at 4 azimuth angles) | Doppler Lidar | 2 - 6 s (~240 m) | 50 m | 0.1 m/s | up to 0.1 m/s | Hardesty (NOAA) |
| Relative aerosol backscatter profiles (1.6 μ m) | Doppler Lidar | 1 s (~ 60 m) | 50 m | Uncalibrated | Uncalibrated | Hardesty (NOAA) |
| NO ₂ vertical column density (VCD) | CU Airborne Multi AXis DOAS | 2 s (~ 1 km) | - | ~ 10 % (up to 30% at high solar zenith angle) | 1.5 x 10 ¹⁵ molec cm ⁻² | Volkamer (CU Boulder) |
| NO ₂ , HCHO, CHOCHO vertical profiles | CU Airborne Multi AXis DOAS | ascent / descent | ~ 150 m | ~ 10 % | Depends on gas and averaging time | Volkamer (CU Boulder) |
| Aerosol extinction profiles (360nm, 477nm, 630nm) | CU Airborne Multi AXis DOAS | ascent / descent | ~ 150 m | - | ~ 0.01 – 0.03 km ⁻¹ (varies at different wavelengths) | Volkamer (CU Boulder) |
| Ozone (at flight level) | UV light absorption | 10 s (~600 m) | - | 1 ppbv / 2% | 1 ppbv / 2% | Langford (NOAA) |
| Temperature (at flight level) | | 1 s (~ 60 m) | - | 0.1 K | 0.1 K | Senff (NOAA / CU Boulder) |
| Surface temperature | IR pyrometer | 1 s (~ 60 m) | - | 0.06 K | 0.5 K | Senff (NOAA / CU Boulder) |
| Surface albedo | 4-channel UV and vis irradiance | 30 s (~1.8km) | - | ~ 5% | ~ 5% | Volkamer (CU Boulder) |

2065 **Table 5:** Summary of DOE G-1, NASA-B200, and NOAA Twin Otter aircraft flights in the CARES domain
 2066 during the month of June 2010.

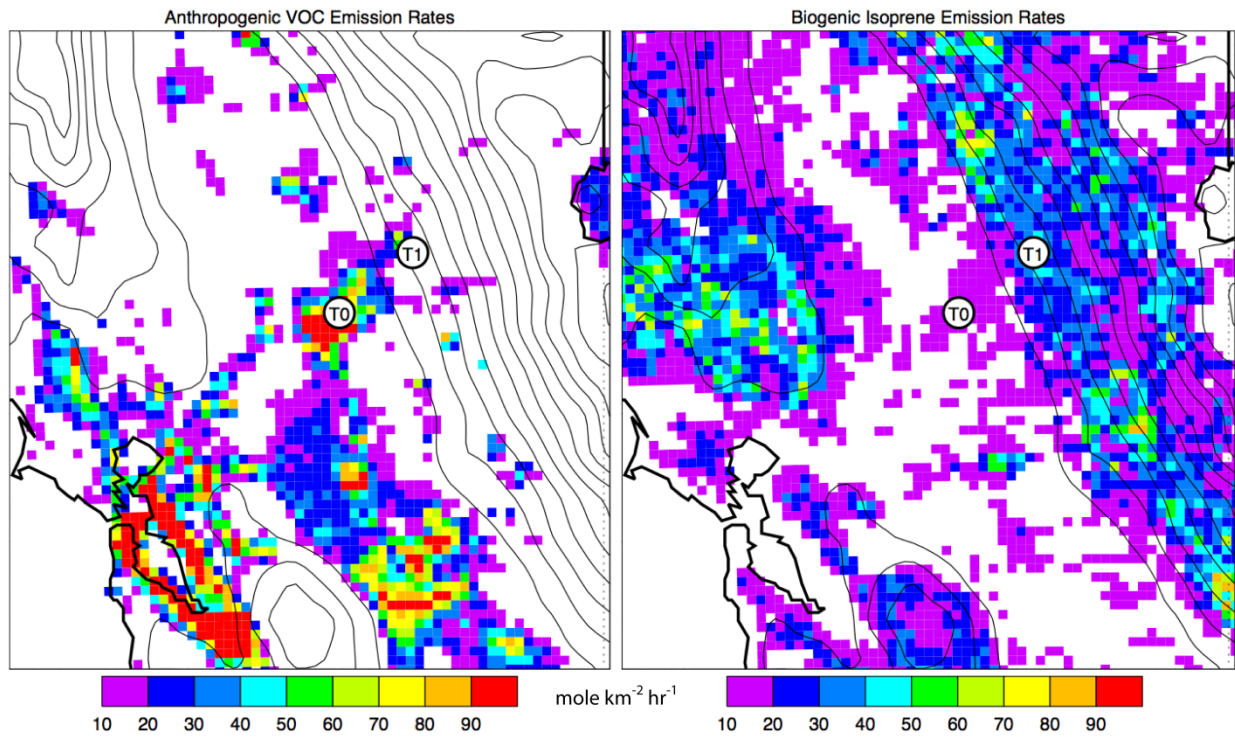
| Date | DOE G-1 Takeoff - Landing PDT | NASA B-200 Takeoff - Landing PDT | NOAA Twin Otter Takeoff - Landing PDT | Wind Dir | Remarks |
|---------|-------------------------------------|--|---|-------------|--|
| June 3 | 12:41 - 15:07 | 12:24 - 15:49 | - | SW | Coordinated with R/V Atlantis; Very low AOD throughout region |
| June 5 | - | 11:29 - 13:43 | - | SW | B-200 flew survey over SAC, northern SJV, and SF/Bay area. |
| June 6 | 10:35 - 13:43 15:35 - 18:20 | 9:26 - 12:24 | - | SW | Very low AOD and shallow PBL. |
| June 8 | 8:55 - 12:12 15:24 - 18:47 | 8:54 - 12:10 14:35 - 17:56 | - | SW | B-200 legs also over Bay area |
| June 10 | 15:36 - 18:31 | 14:31 - 17:56 | - | NW | B-200 flew over SAC and also over Sierra Nevada mountains for RSP snow measurements |
| June 12 | 08:55 - 11:59 15:24 - 18:28 | 9:08 - 12:40 15:05 - 17:50 | - | NW | B-200 legs also over northern SJV and SF/Bay Area. HSRL observed high aerosol depolarization associated with dust. |
| June 14 | 09:56 - 13:10 | 10:09 - 13:42 15:18 - 18:00 | - | SW | Bay Area inflow; B200 flew two flights and covered regions between SF/Bay area and SAC. Second B200 flight flew over NOAA P3 track. |
| June 15 | 08:56 - 12:00 14:51 - 18:07 | 9:09 - 12:23 14:39 - 18:02 | 11:52 – 15:12 16:15 – 19:15 | SW | B-200 legs over SF/Bay area, SAC, and mountains east of SAC. Inflow from SF/Bay area. Highest AOD over SAC. |
| June 18 | 15:38 - 18:48 | 15:19 - 18:53 | 12:36 – 15:39 16:40 – 20:10 | SW | Intercomparison between G-1, NOAA WP-3, B-200, and NOAA TO from Fresno to Bakersfield. |
| June 19 | 15:28 - 18:31 | 9:46 - 11:52 15:32 - 18:33 | - | SW | B-200 also flew over mountains east of SAC. HSRL observed elevated dust layer 5-8 km. |
| June 21 | 09:02 - 12:11 15:25 - 18:44 | 15:32 - 18:52 | 10:05 – 13:50 15:15 – 18:40 | NW | NOAA TO coordinated with OMI satellite ^a |
| June 22 | - | 14:08 - 16:16 | 8:20 – 11:27 13:39 – 17:12 | W | B-200 and NOAA TO flew coordinated flight for long range transport. |
| June 23 | 09:34 - 12:51 14:24 - 18:12 | 9:51 - 12:01 14:52 - 17:09 | 14:40 – 17:55 | SW | HSRL observed elevated layers and clouds over SAC. NOAA TO coordinated with OMI satellite ^a |
| June 24 | 09:00 - 12:16 14:24 - 18:12 | 14:56 - 17:45 | 9:42 – 13:15 15:12 – 18:55 | SW | Bay Area Inflow; HSRL observed considerable midlevel clouds over SAC |
| June 26 | - | - | 15:15 – 19:03 | SW | |
| June 27 | 10:24 - 13:47 | 9:19 - 12:25 | 9:37 – 13:32 15:15 – 19:02 | SW | Isoprene flux flight to the northeast over the foothills area: B-200 had leg over SF/Bay Area. Highest AOD over SAC region. |
| June 28 | 09:23 - 12:33 14:20 - 17:42 | 10:10 - 13:20 15:56 - 18:18 | 10:15 – 14:06 | W | MISR Overpass, highest pollution and AOD day of the campaign. Largest AOD over SAC, observed SAC plume in AOD. NOAA TO coordinated with OMI satellite ^a |
| June 29 | - | - | 8:00 – 11:10 12:29 – 16:17 | | Bakersfield NOx emission inventory, San Francisco, San Joaquin Valley |
| Total | 21 | 23 | 17 | | |

2067 ^aNO₂ tropospheric VCD are measured by the OMI instrument onboard the NASA Aura satellite. Global coverage is
 2068 achieved within one day.



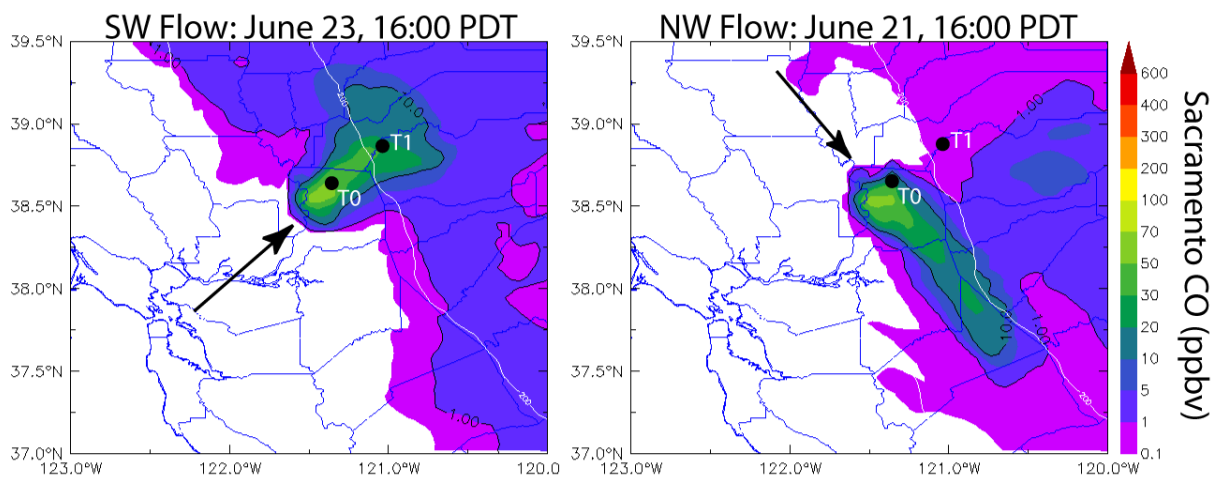
2069
 2070
 2071
 2072
 2073
 2074

Figure 1. Locations of the ground sites “T0” (latitude: 38.6483, longitude: -121.3493, altitude: ~30 m MSL) and “T1” (latitude: 38.8711, longitude: -121.0228, altitude: ~450 m MSL). Light blue arrows indicate typical daytime flow pattern in the region during summer.



2075
2076
2077
2078
2079

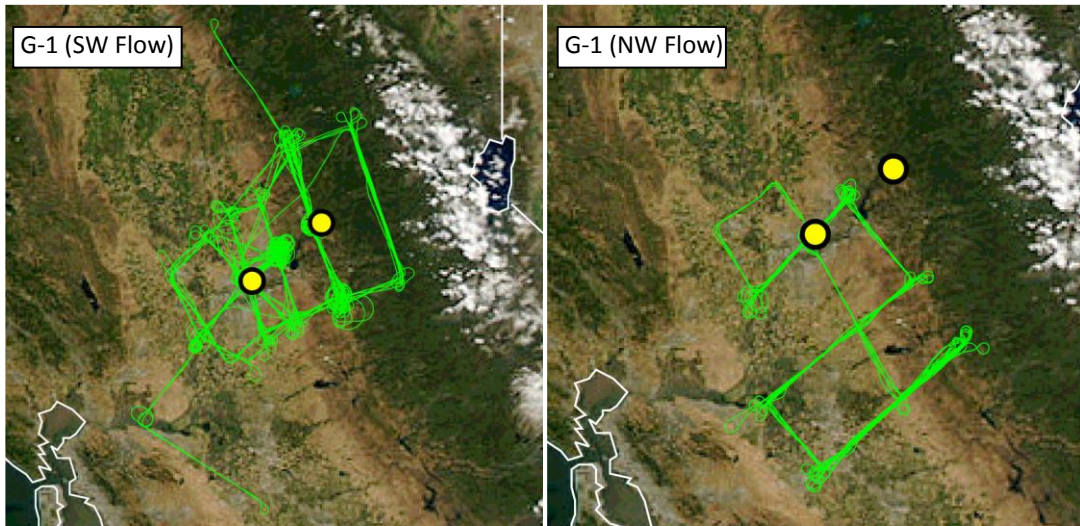
Figure 2. Emission rates in the Central Valley at 11:00 PDT. Left panel: sum of all anthropogenic VOCs. Right panel: biogenic isoprene.



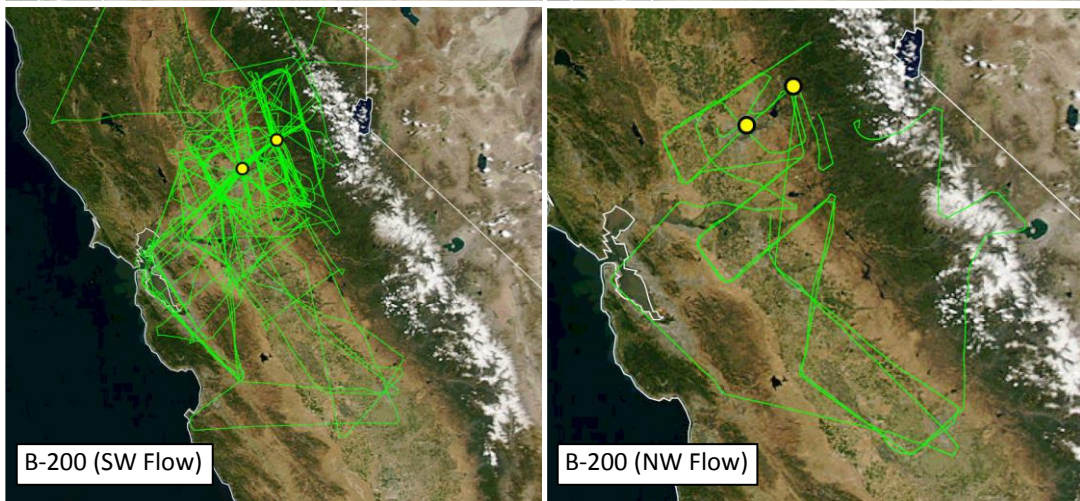
2080
 2081
 2082
 2083
 2084
 2085
 2086

Figure 3. Examples of tracer forecasts, based on CO emitted from Sacramento, shown at 16:00 PDT under southwesterly (left panel) and northwesterly wind (right panel) flow conditions.

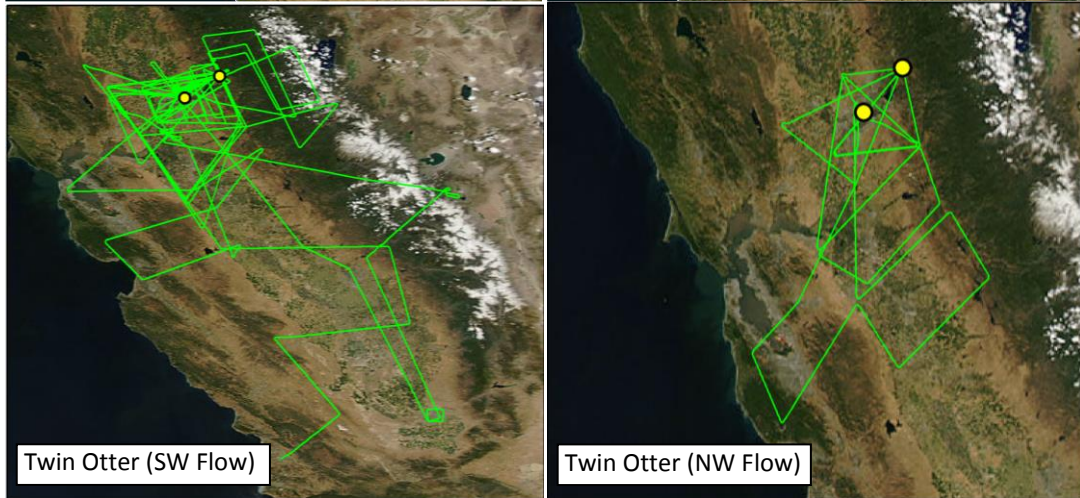
2088



2089



2090

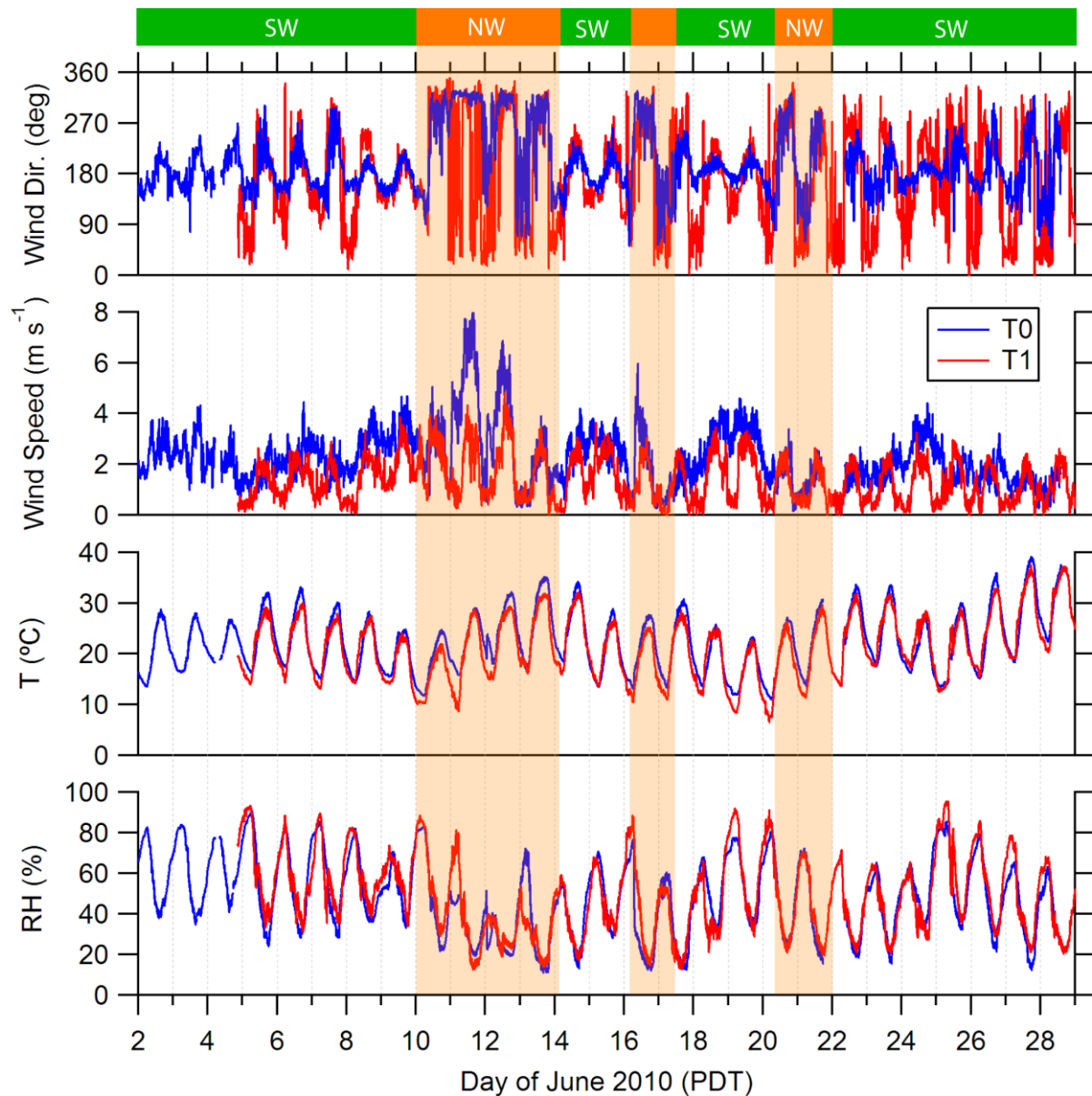


2091

2092

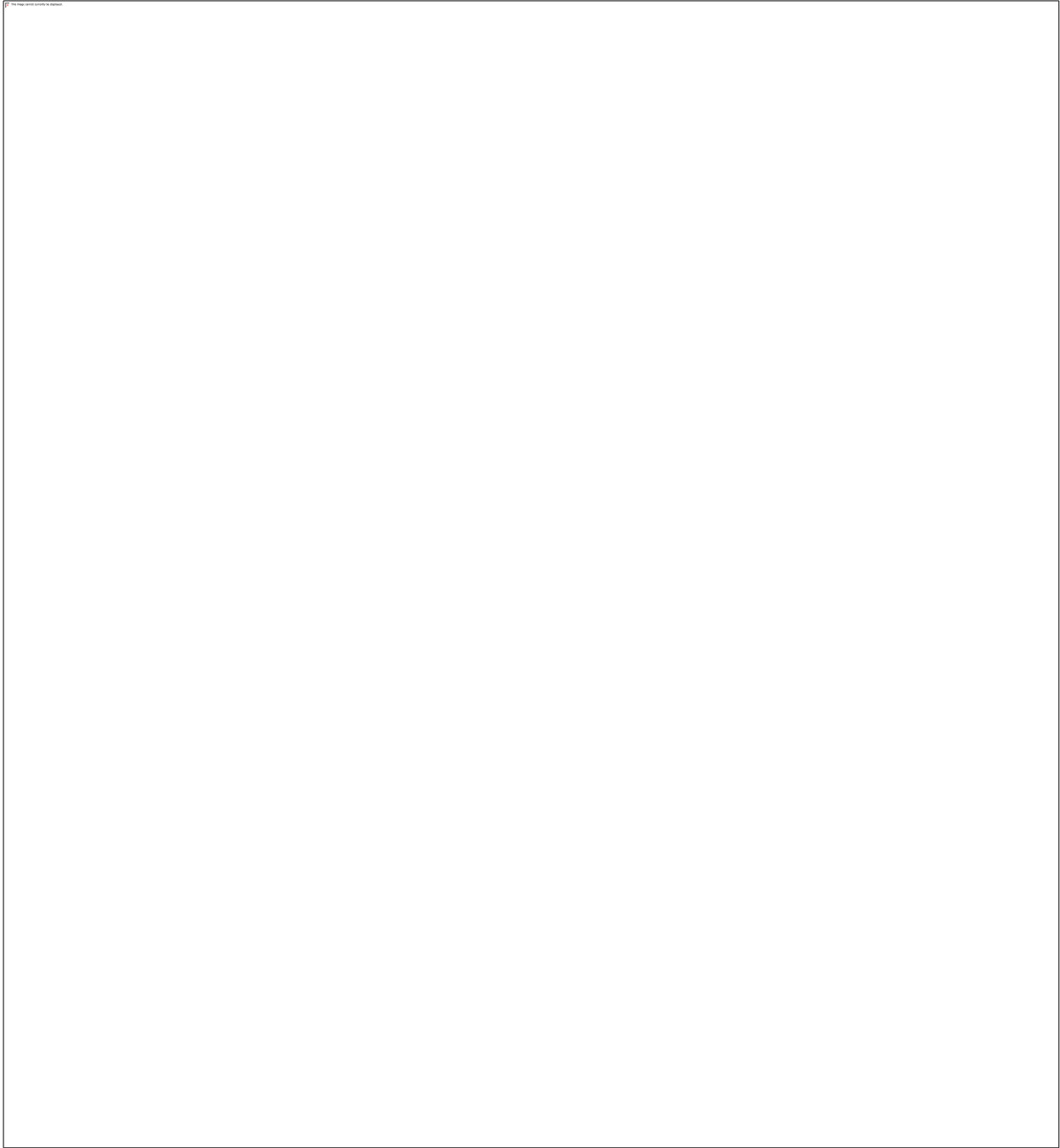
2093

Figure 4. DOE G-1, NASA B-200, and NOAA Twin Otter Flight Tracks during the SW and NW flow periods. The yellow circles indicate the locations of the T0 and T1 ground sites.



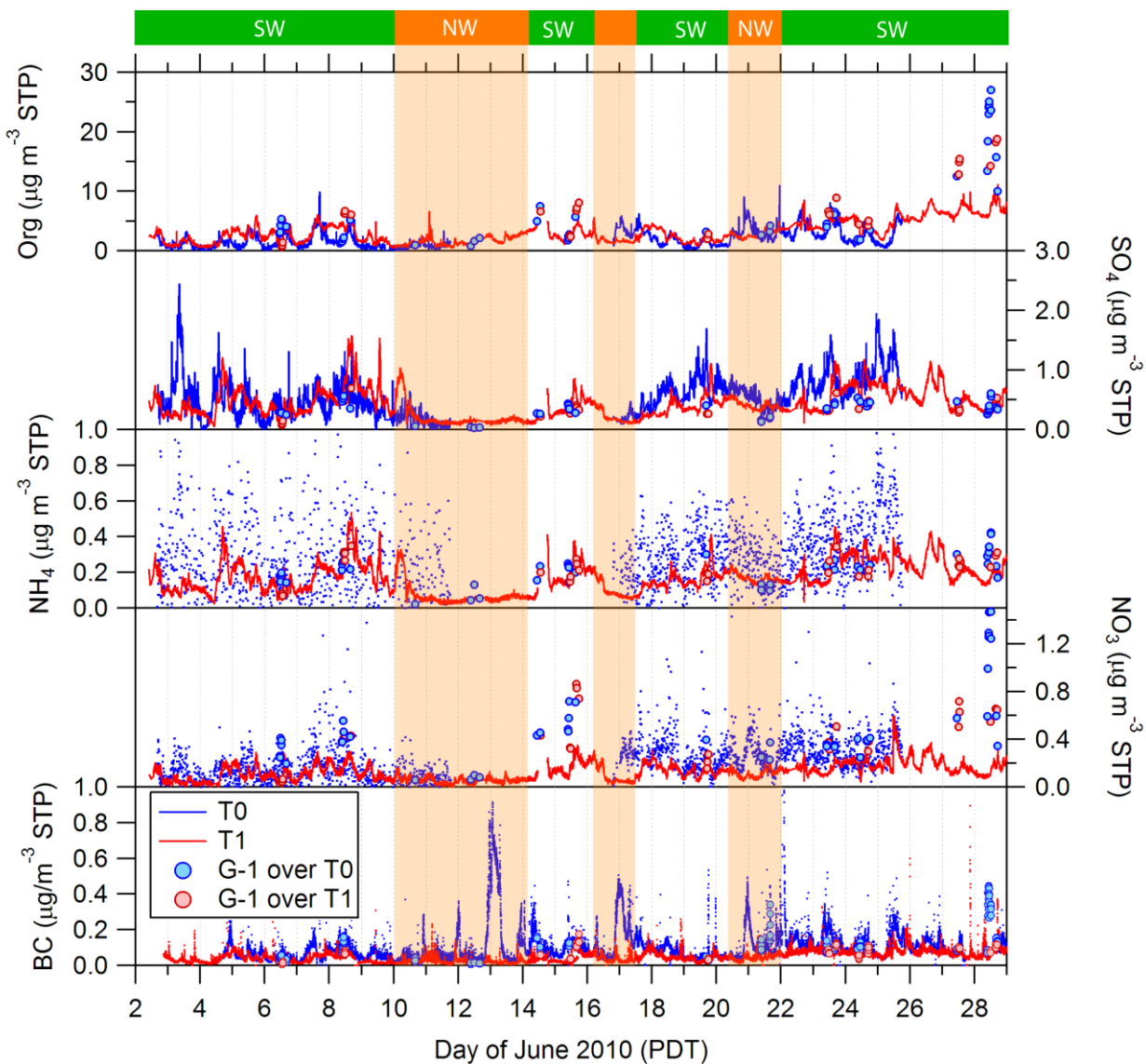
2094
 2095
 2096
 2097
 2098
 2099
 2100
 2101

Figure 5. Time series of standard meteorological variables at the T0 and T1 ground sites. The green-orange bar at the top indicates periods during which the synoptic wind was either southwesterly (SW) or northwesterly (NW). Semi-transparent orange shading for the NW flow periods is also shown over all the plots.



2102
2103
2104
2105
2106
2107
2108

Figure 6. Comparison of trace gases time series at T0 and T1 ground sites along with observations onboard the G-1 during overpasses at the respective sites. The NO_y instrument at the T1 site did not operate until June 11 and the SO₂ instrument at the T0 site did not operate on June 27-28.



2110

2111

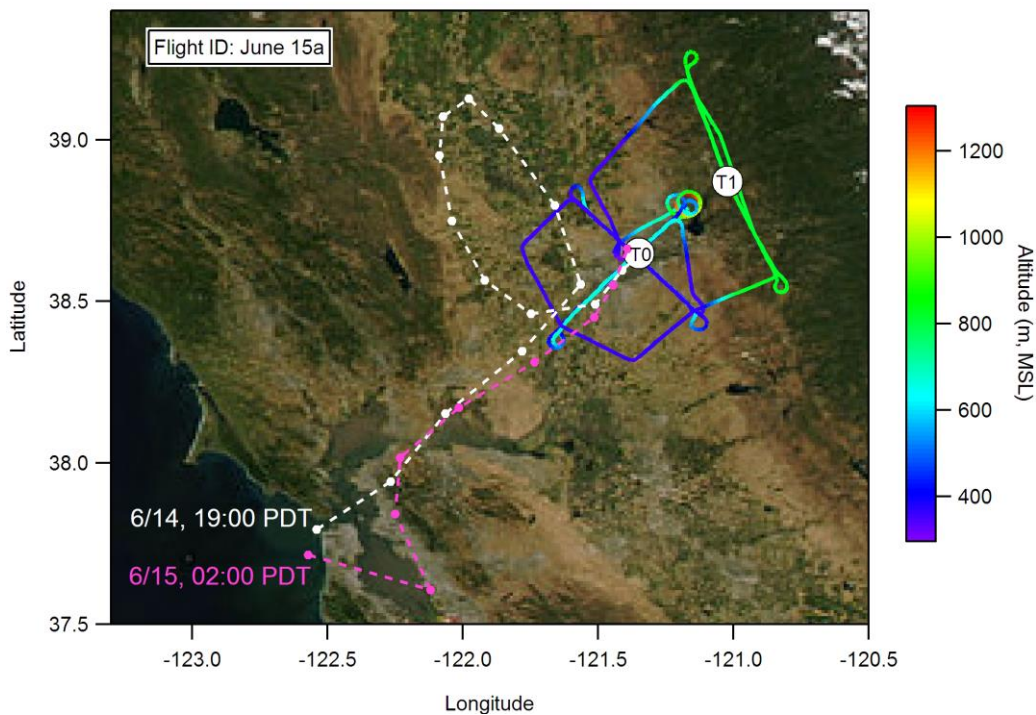
2112

2113 **Figure 7.** Comparison of bulk aerosol species time series at T0 and T1 ground sites along with

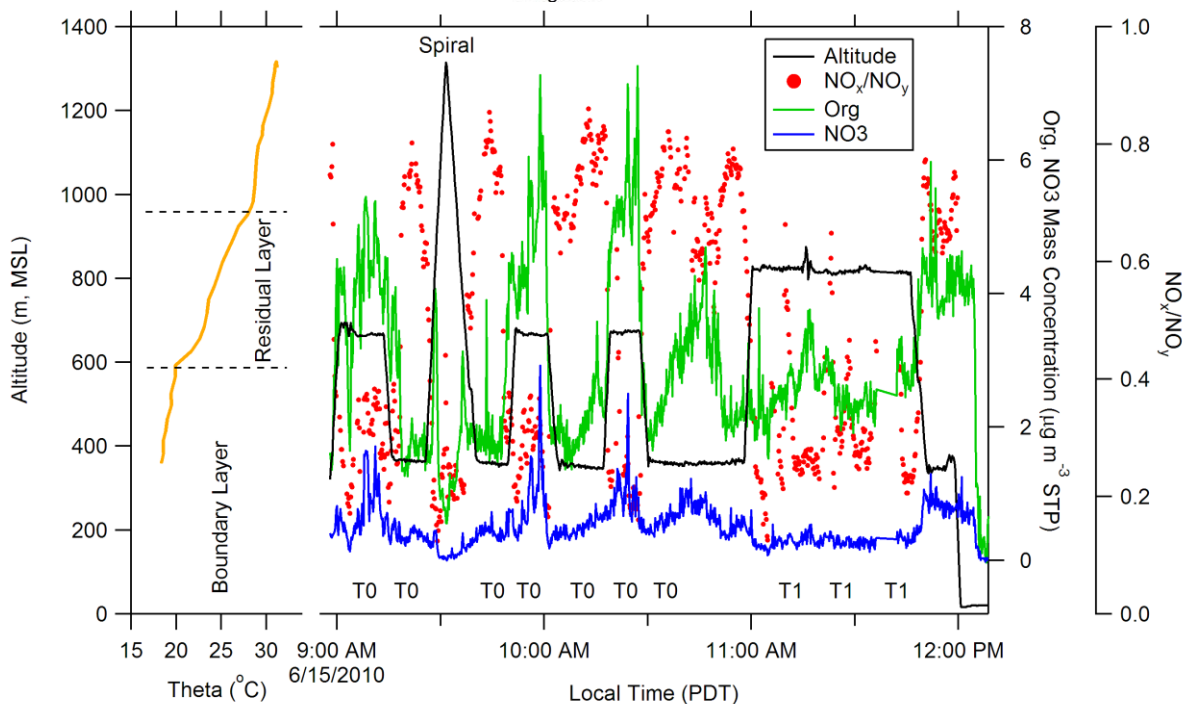
2114 observations onboard the G-1 during overpasses at the respective sites.

2115

2116



2117



2118

2119

2120

2121

2122

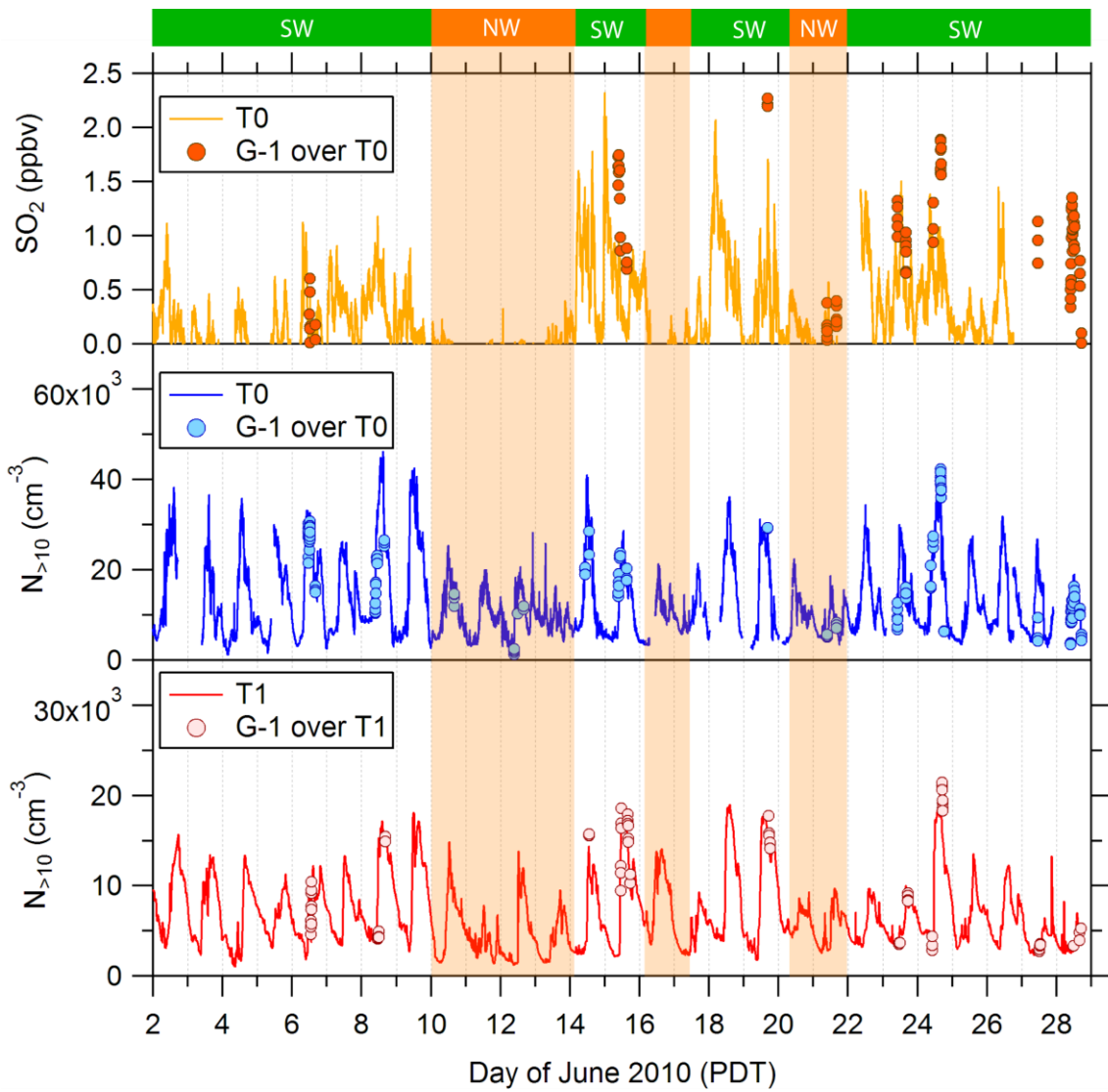
2123

2124

2125

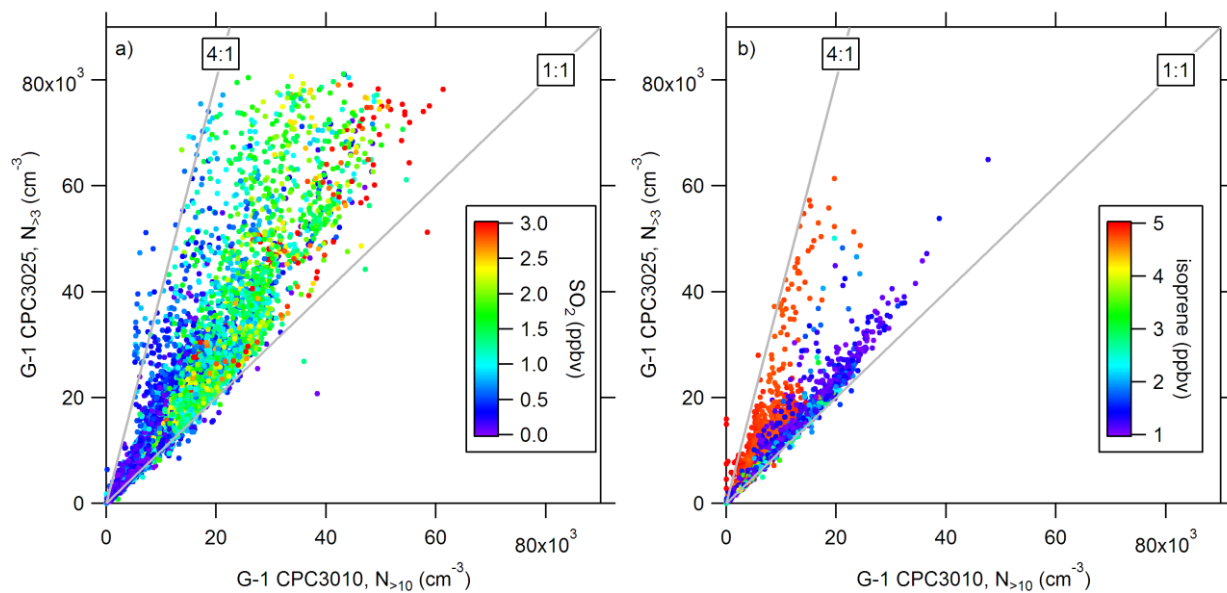
2126

Figure 8. Example of evidence for aged aerosols (enriched in organic and nitrate) that were often found to be present in the residual layer in the morning. Top: G-1 flight tracks on the morning of June 15, color coded by flight altitude. The dotted white and pink lines represent forward trajectories of air parcels (see text). Bottom right: Vertical profile of potential temperature at the location of the spiral. Bottom left: Flight altitude, org and NO₃ mass concentrations, and NO_x/NO_y ratio plotted along the flight track as a function of local time.



2127
 2128
 2129
 2130
 2131
 2132
 2133
 2134

Figure 9. Time series of SO₂ mixing ratio at T0 site and comparison of CPC 3010 number concentration (N_{>10}) time series at T0 and T1 sites along with observations onboard the G-1 during overpasses at the respective sites.

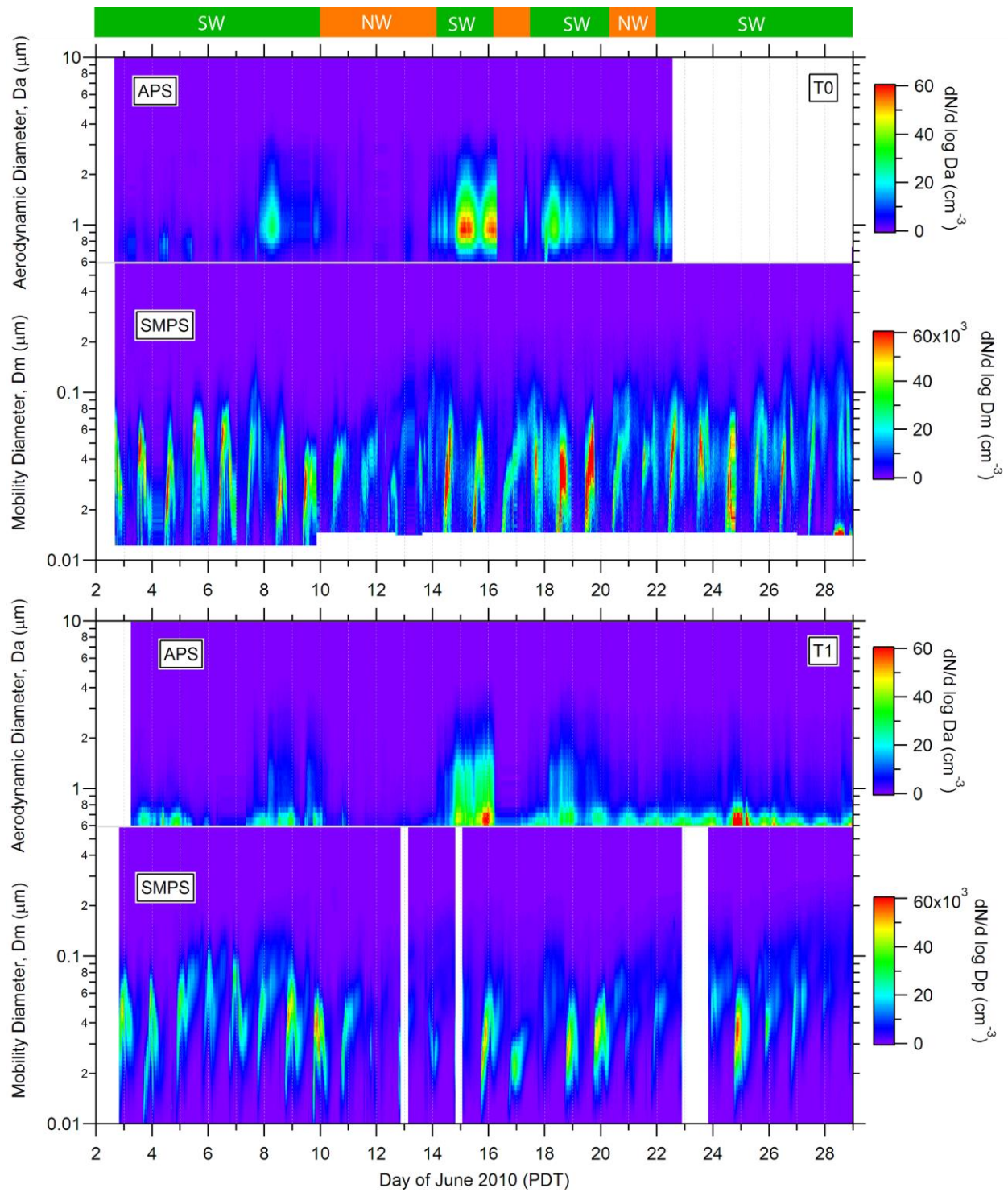


2135

2136

2137 **Figure 10.** Scatter plots of CPC-3025 vs. CPC-3010 number concentrations observed on the G-1: a)
 2138 the points are colored by the corresponding SO_2 mixing ratios; b) the points are colored by the
 2139 corresponding isoprene mixing ratios (points with isoprene mixing ratios < 1 ppbv were removed
 2140 from the plot for clarity). Grey lines show slopes of 4:1 and 1:1.

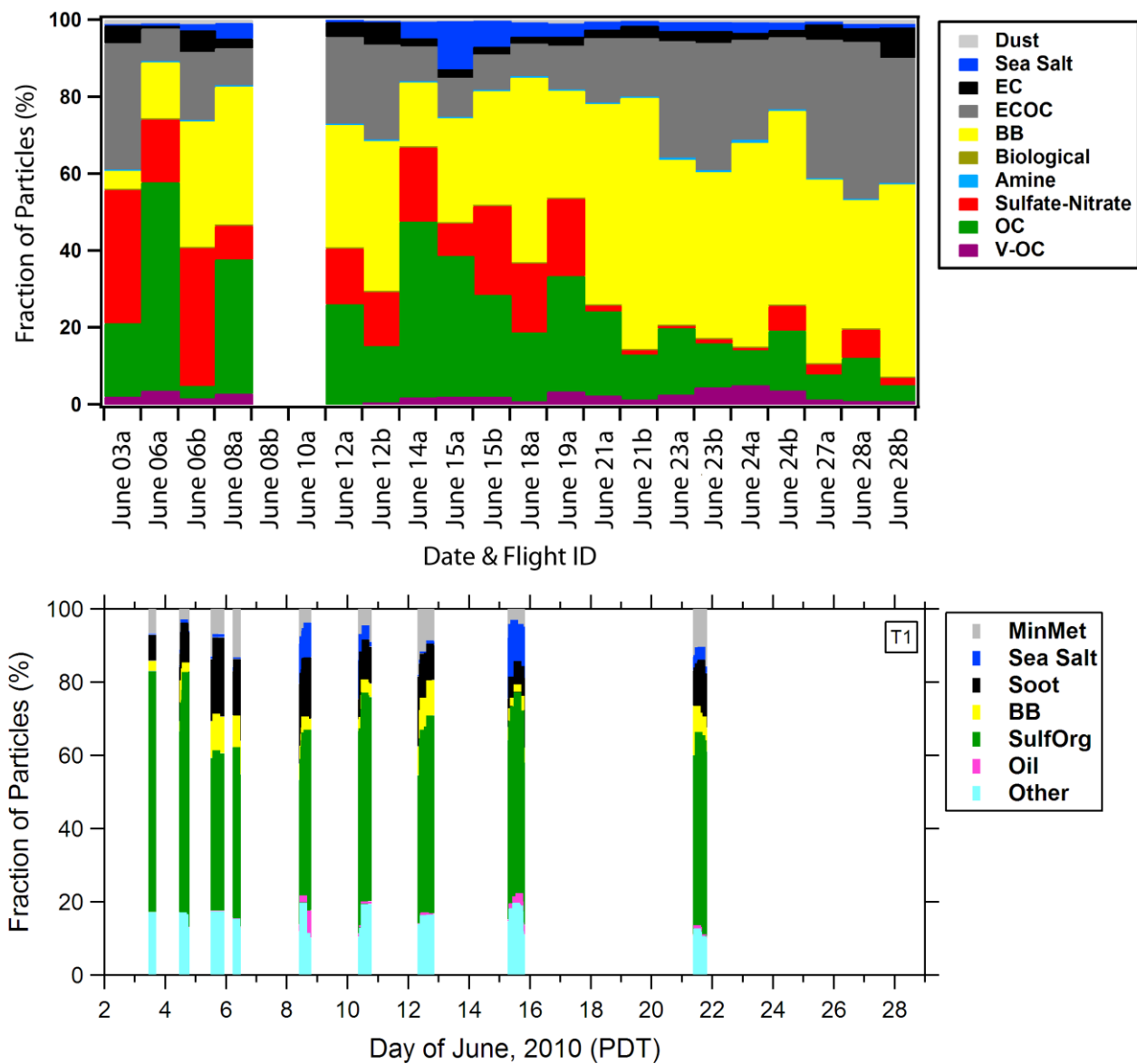
2141



2142
 2143
 2144
 2145
 2146
 2147

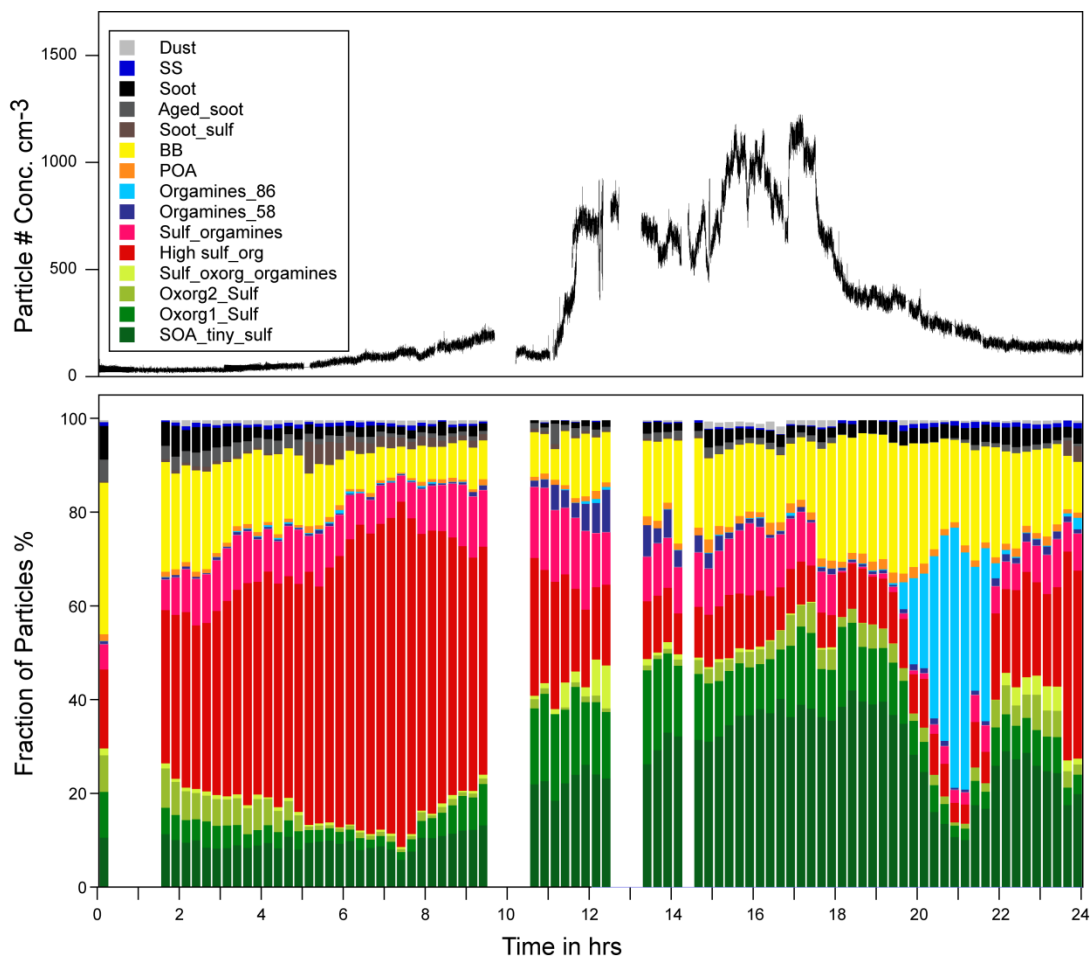
Figure 11. Comparison of aerosol number size distributions at T0 and T1 sites. Note that the color scales for APS and SMPS distributions differ by three orders of magnitude.

2148
2149



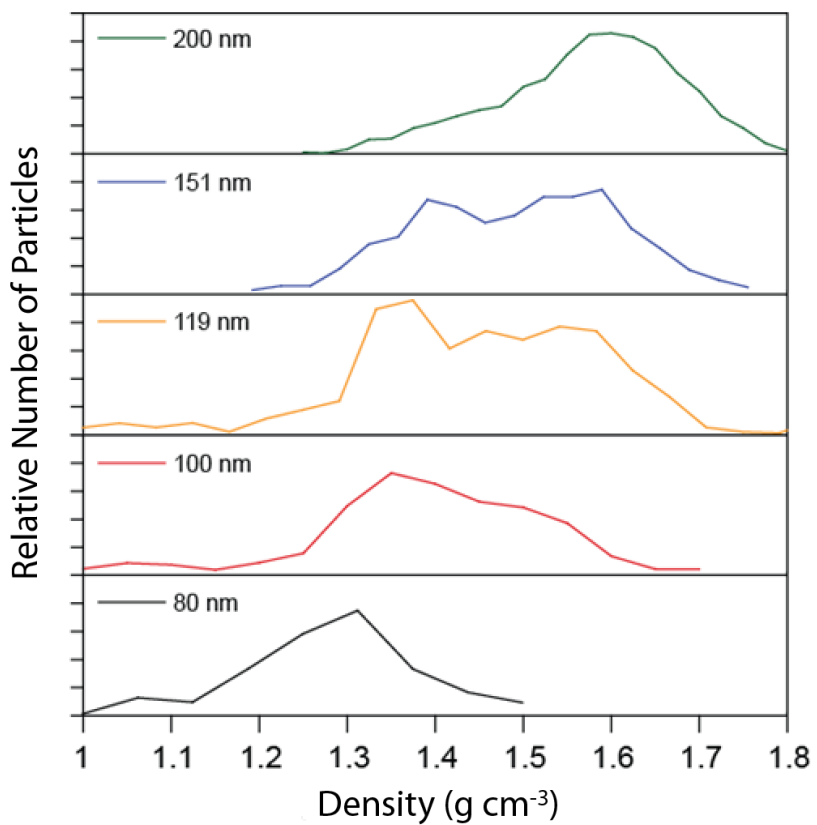
2150
2151
2152
2153
2154
2155
2156
2157
2158

Figure 12. Variations in fractions of different particles observed by ATOFMS aboard the G-1 (upper panel) and by PALMS at the T1 site (lower panel). EC is elemental carbon, BB is biomass burning particles, V-OC is organic particles containing vanadium, MinMet is mineral dust and metallic particles.



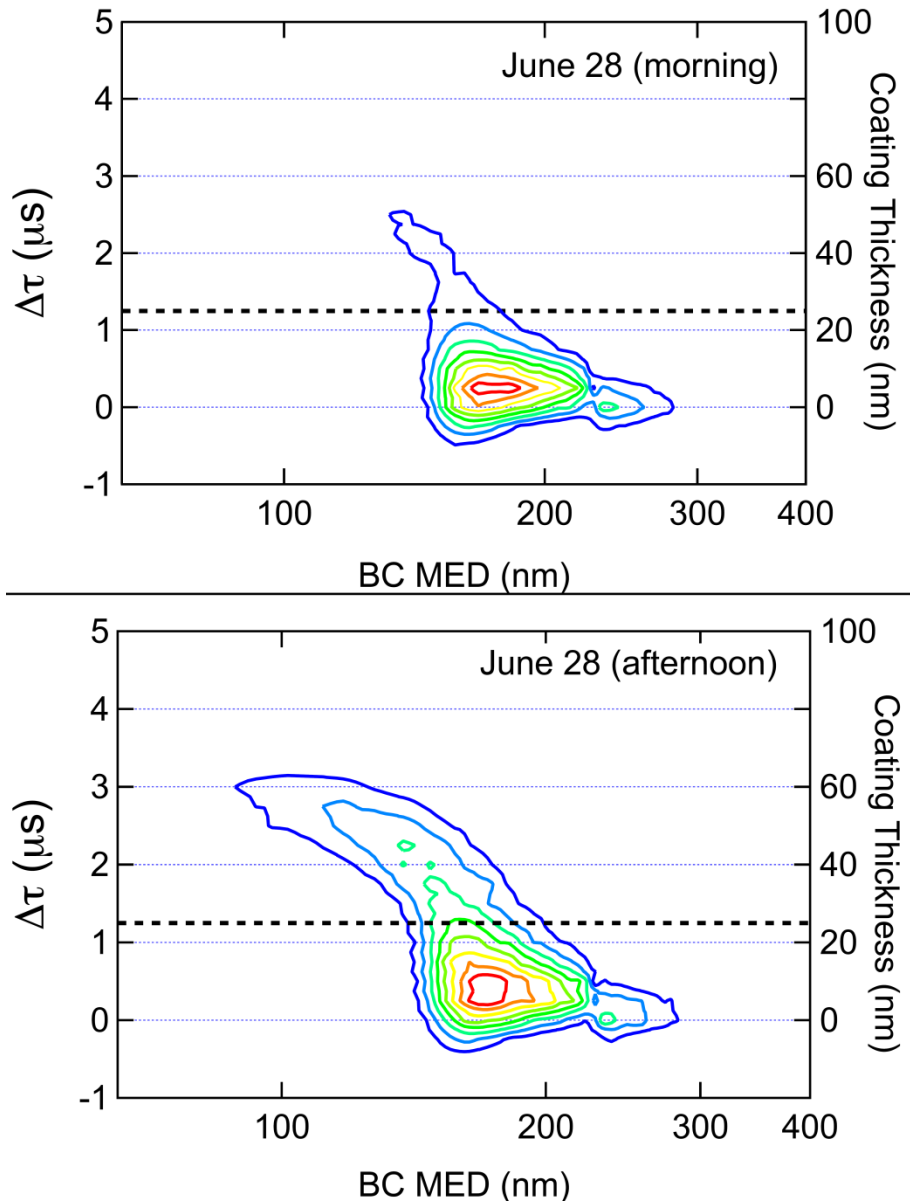
2159
 2160
 2161
 2162
 2163
 2164
 2165
 2166
 2167
 2168

Figure 13. Temporal evolution of particle number concentration (upper panel) and the corresponding fraction of particles with different compositions (lower panel) as observed by SPLAT II on June 6 at the T0 site. SS is sea salt, BB is biomass burning particles.



2169
 2170
 2171
 2172
 2173
 2174

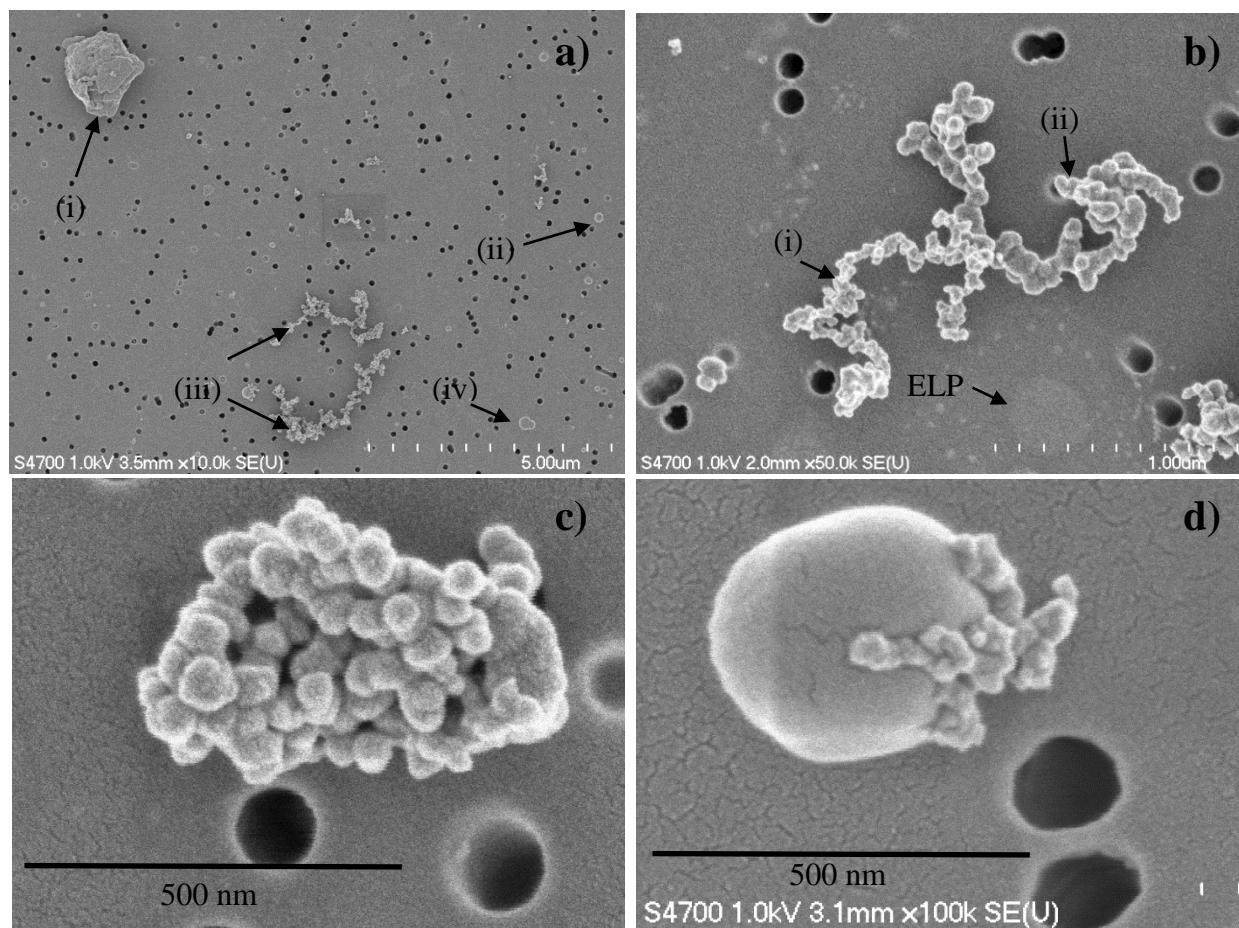
Figure 14. Size-dependent particle densities as measured by SPLAT II on June 6 at 10 am.



2175
 2176
 2177
 2178
 2179
 2180
 2181
 2182
 2183
 2184
 2185
 2186
 2187

Figure 15. The time delay between the observance of the incandescence signal peak relative to the peak in the scattering signal (incandescence-scattering lagtime, $\Delta\tau$) is plotted as a function of the BC mass equivalent diameter (MED) for the morning and afternoon flights conducted on June 28th. Number concentration contours are normalized to unity (red = 0.9, blue = 0.2) to highlight the differences between the two flights. Since the non-refractory coating must be burned off before the BC core will incandesce, the recorded lagtime can serve as a proxy for coating thickness – the larger the lagtime, the greater the coating thickness. The morning ensemble lagtimes are dominated by thinly coated soot whereas in the afternoon an increase in the fraction of thickly coated larger diameter BC core is observed.

2188
2189

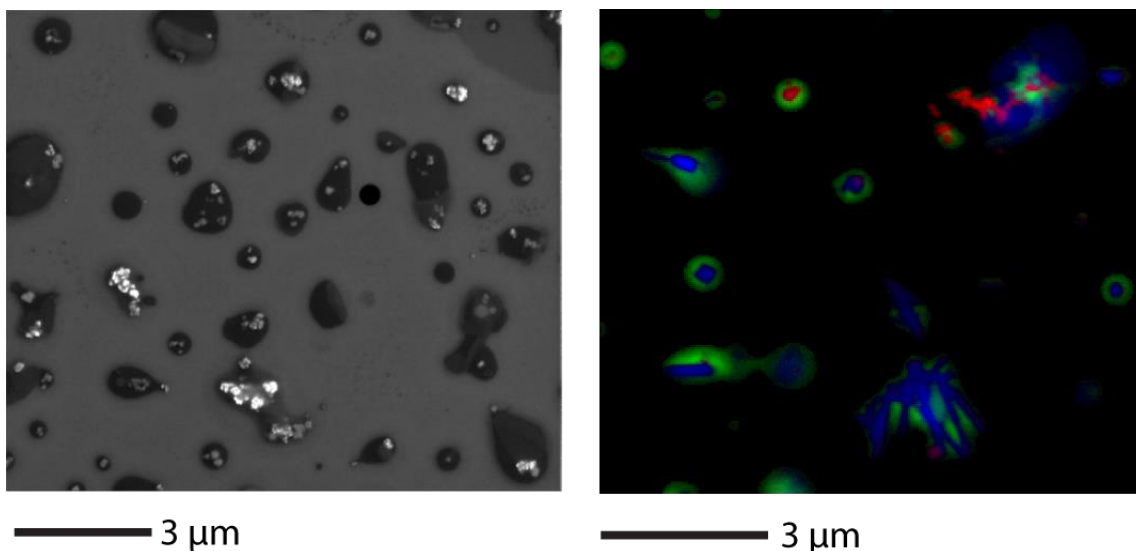


2190

2191

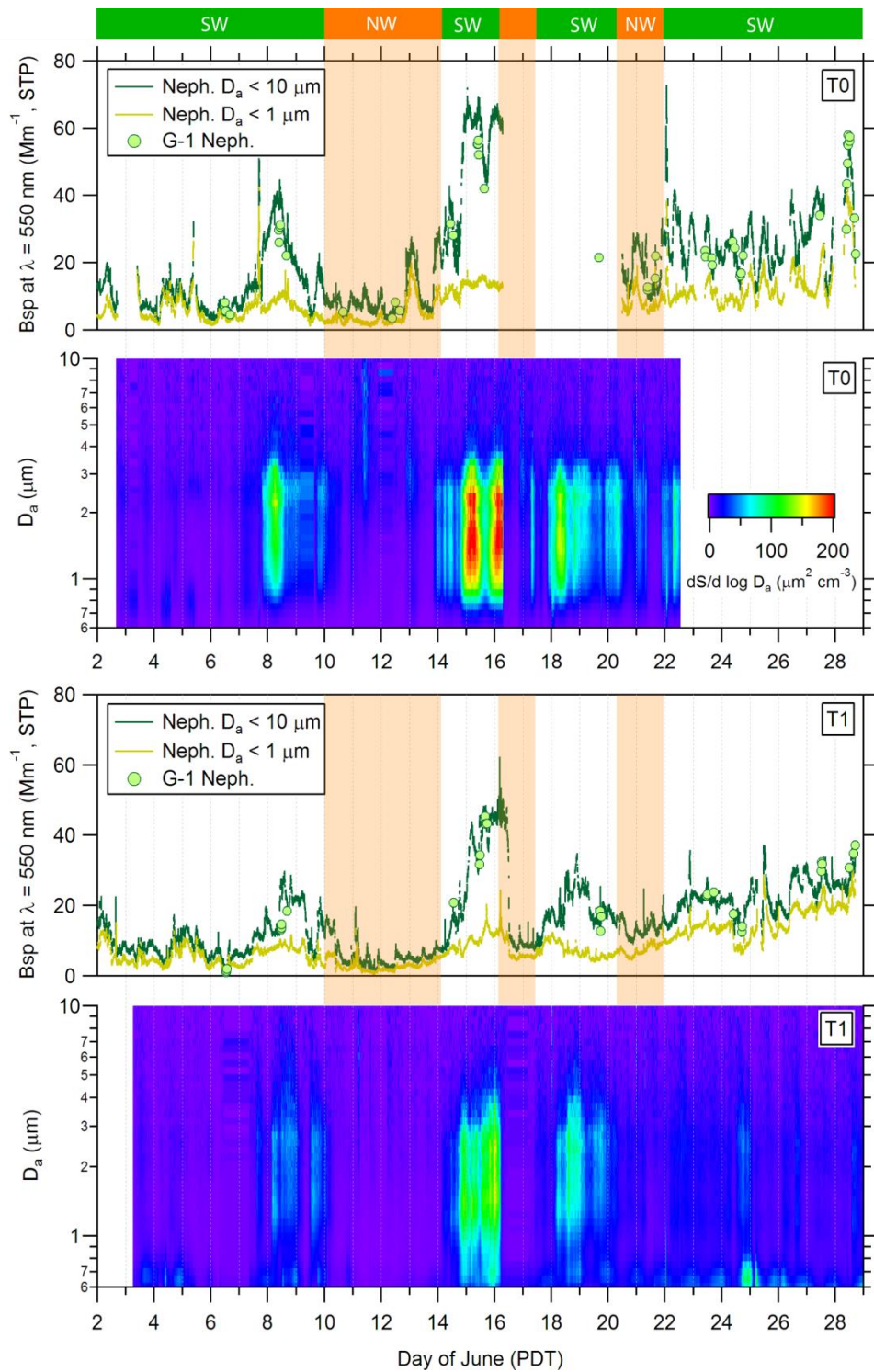
2192 **Figure 16.** FE-SEM images of aerosol particles collected at the T0 site: (a) a low magnification
2193 image showing (i) dust particle, (ii) spherical particle, (iii) fractal-like particles, (iv)
2194 irregularly-shaped particle; (b) fractal-like particle with open structure, (i) soot without evident coating, (ii)
2195 soot with relatively thick coating, ELP – evaporated liquid particle; (c) compacted BC particle
2196 internally mixed; (d) particle with BC inclusion. The dark dots are the pores in the filter.

2197
2198
2199



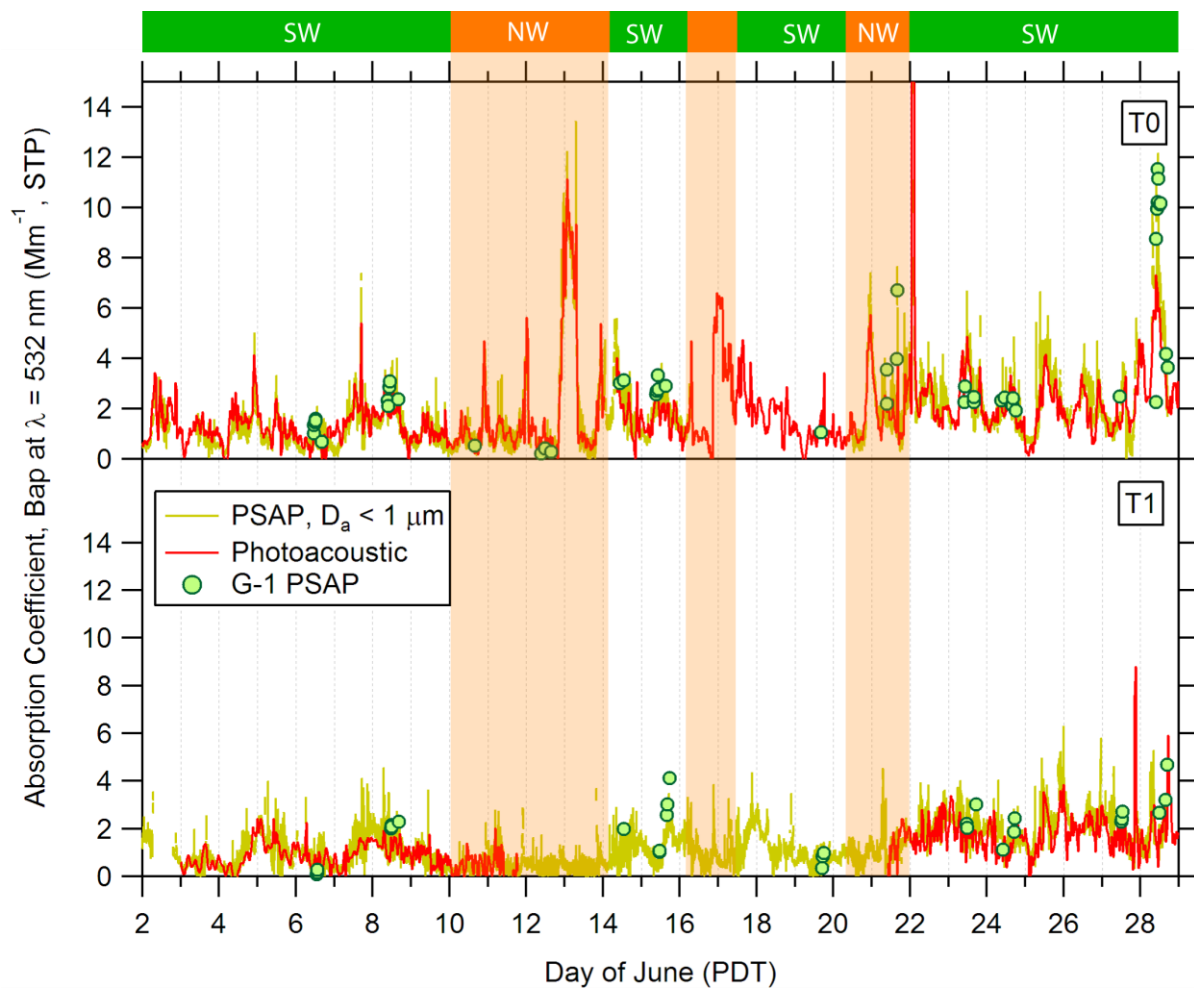
2200
2201
2202
2203
2204
2205
2206
2207
2208

Figure 17. SEM (left panel) and STXM (right panel) images showing internal heterogeneity of particles collected in CARES study. STXM maps derived by singular value decomposition depict organic dominant phase (green), inorganic dominant phase (blue) and elemental carbon (red). Images are not from the same sample region.



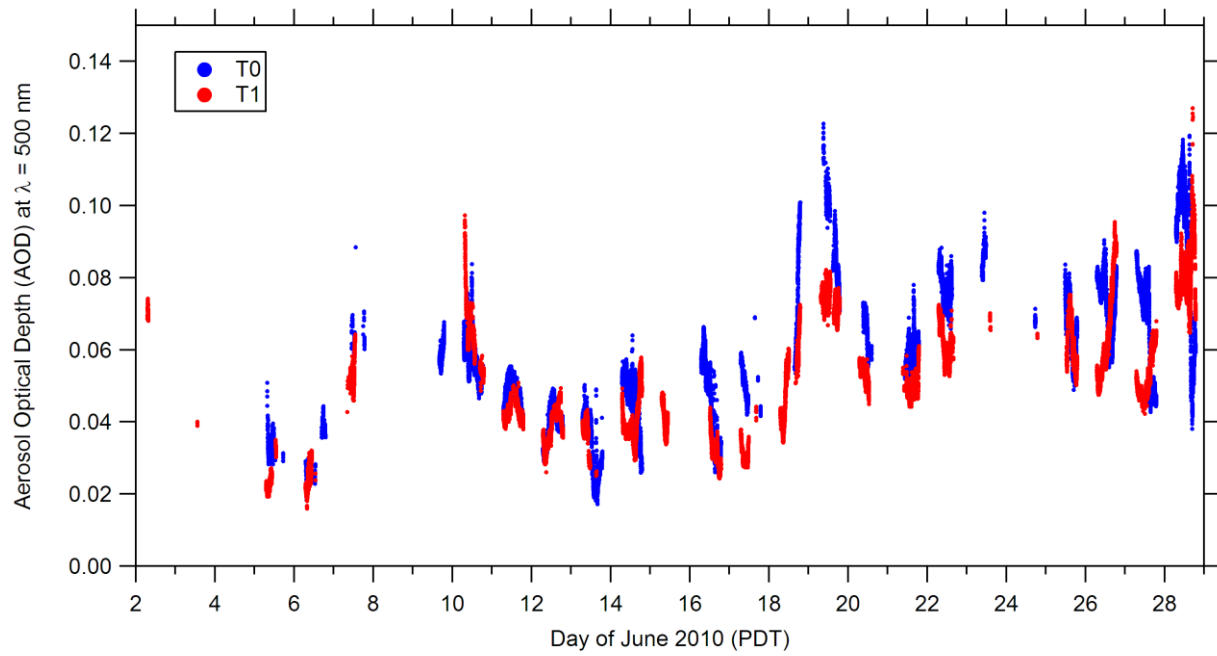
2209
 2210
 2211
 2212
 2213
 2214
 2215

Figure 18. Comparison of scattering coefficient measured by nephelometer at the T0 and T1 sites and onboard the G-1 during overpasses at the respective sites.



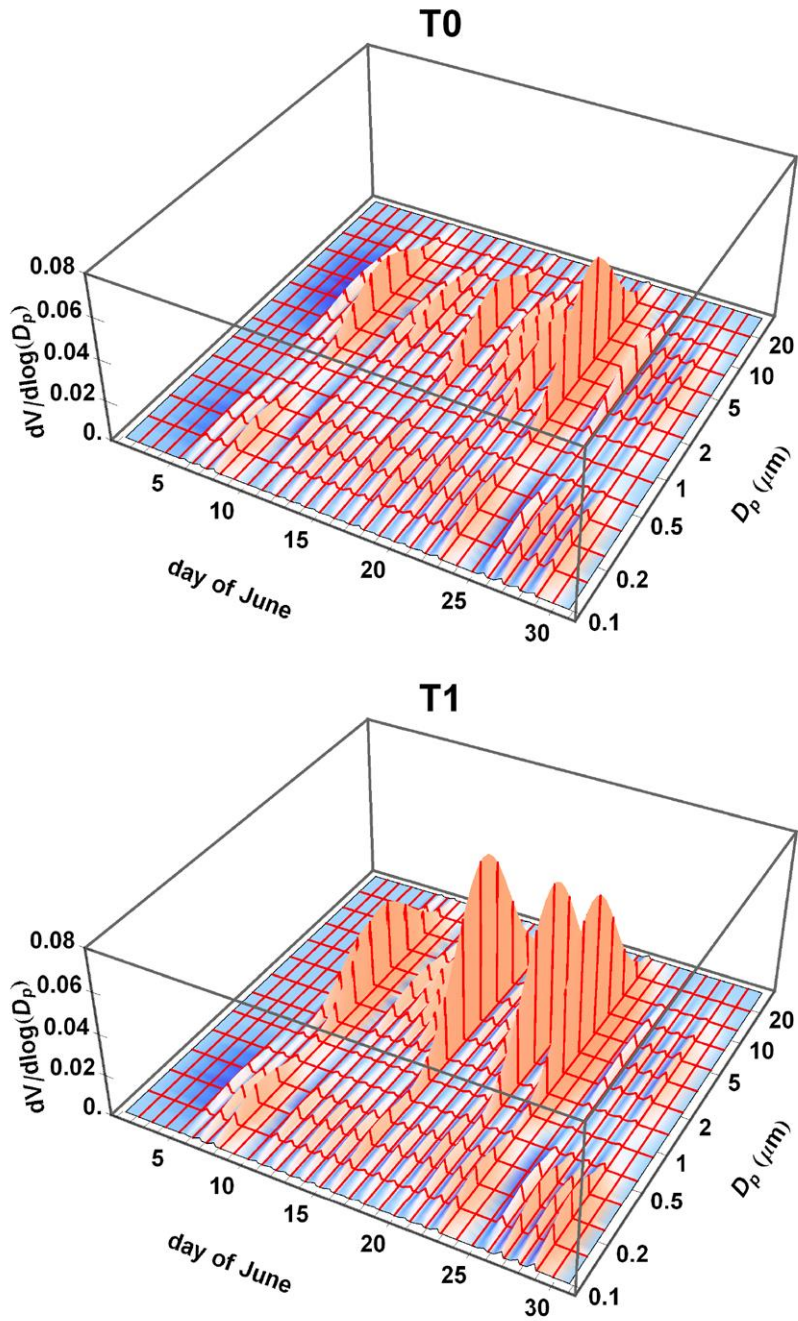
2216
 2217
 2218
 2219
 2220
 2221
 2222

Figure 19. Comparison of absorption coefficient measured at $\lambda = 532$ nm by PSAP and photoacoustic instruments at the T0 and T1 sites and by PSAP ($\lambda = 522$ nm) aboard the G-1 during overpasses at the respective sites.



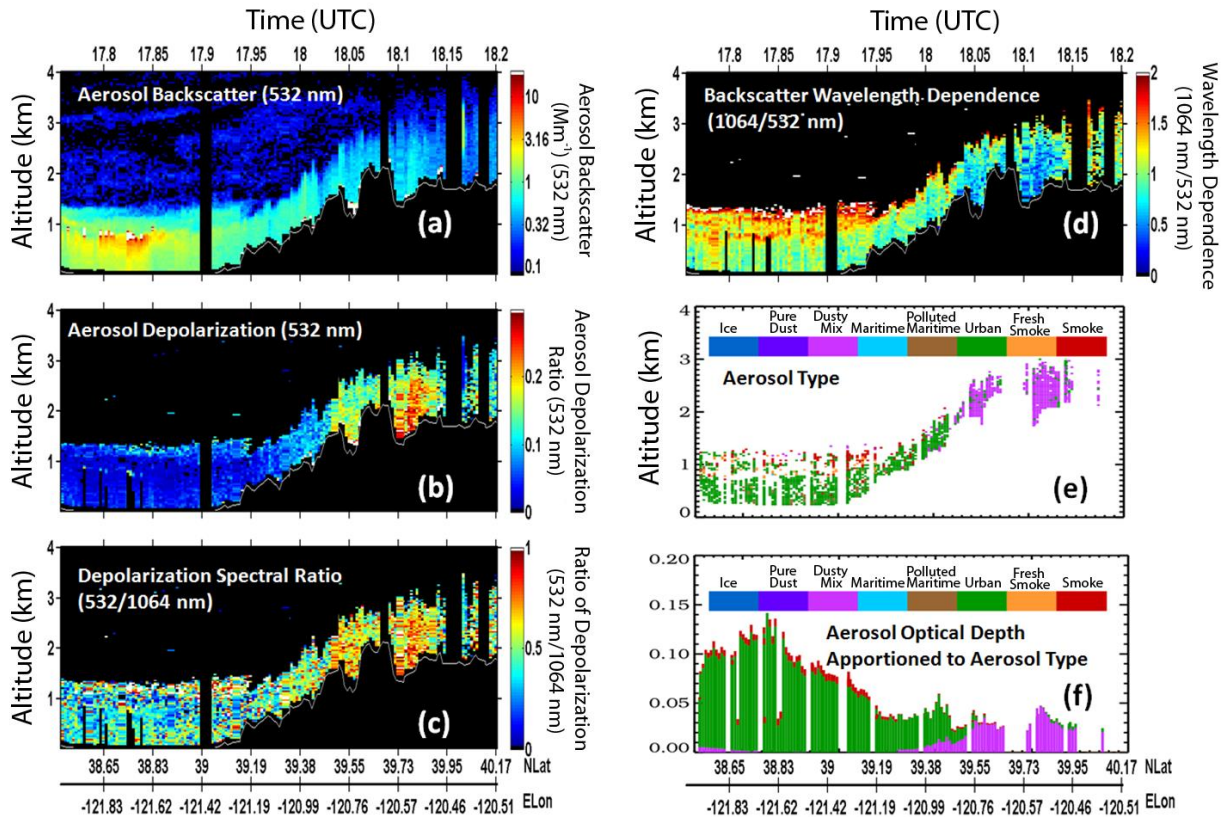
2223
2224
2225 **Figure 20.** Comparison of aerosol optical depth derived from MFRSR observations at T0 and T1
2226 sites.

2227
2228
2229



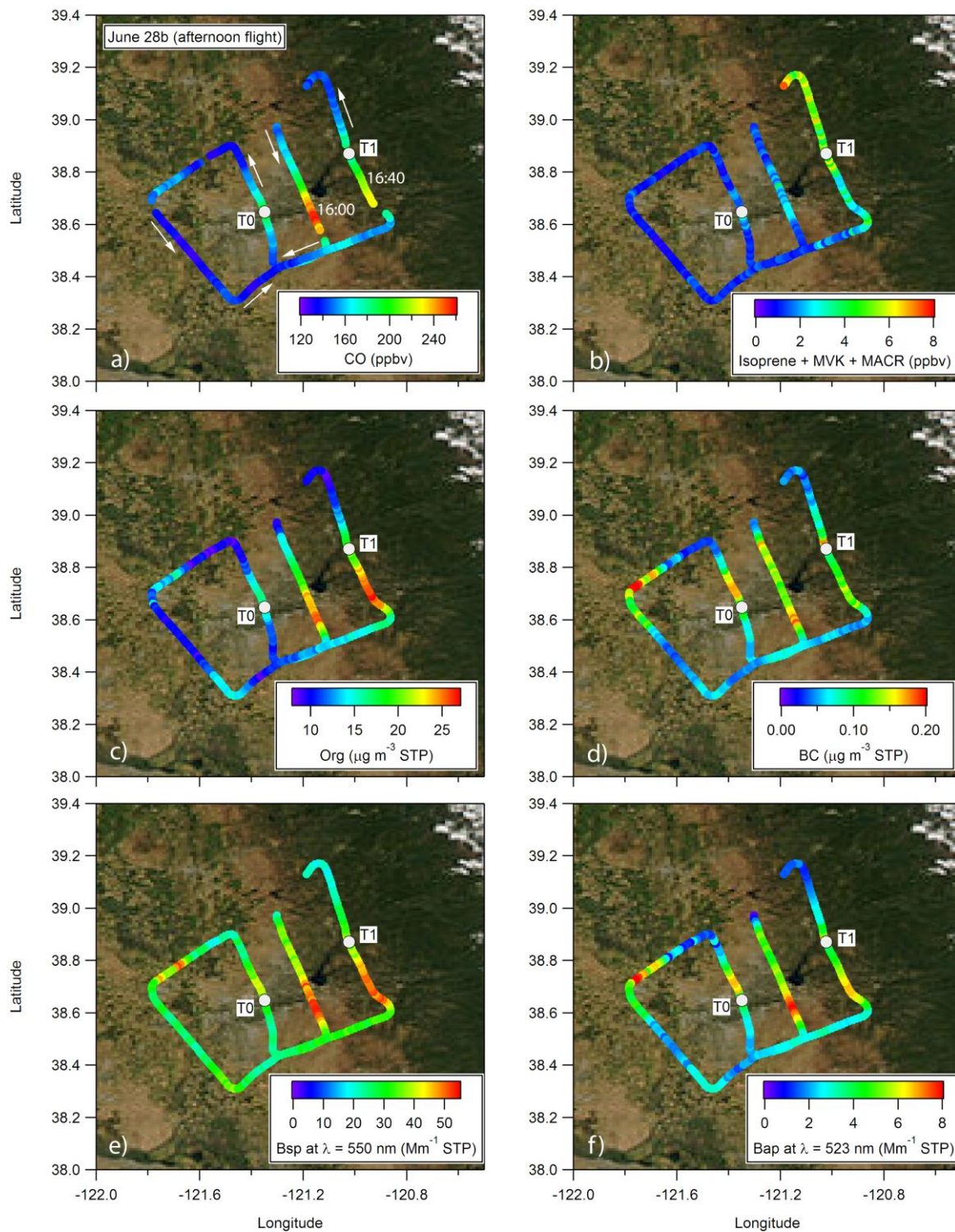
2230
 2231
 2232
 2233
 2234
 2235

Figure 21. Daily average volume size distributions derived from MFRSR observations at T0 and T1 ground sites.



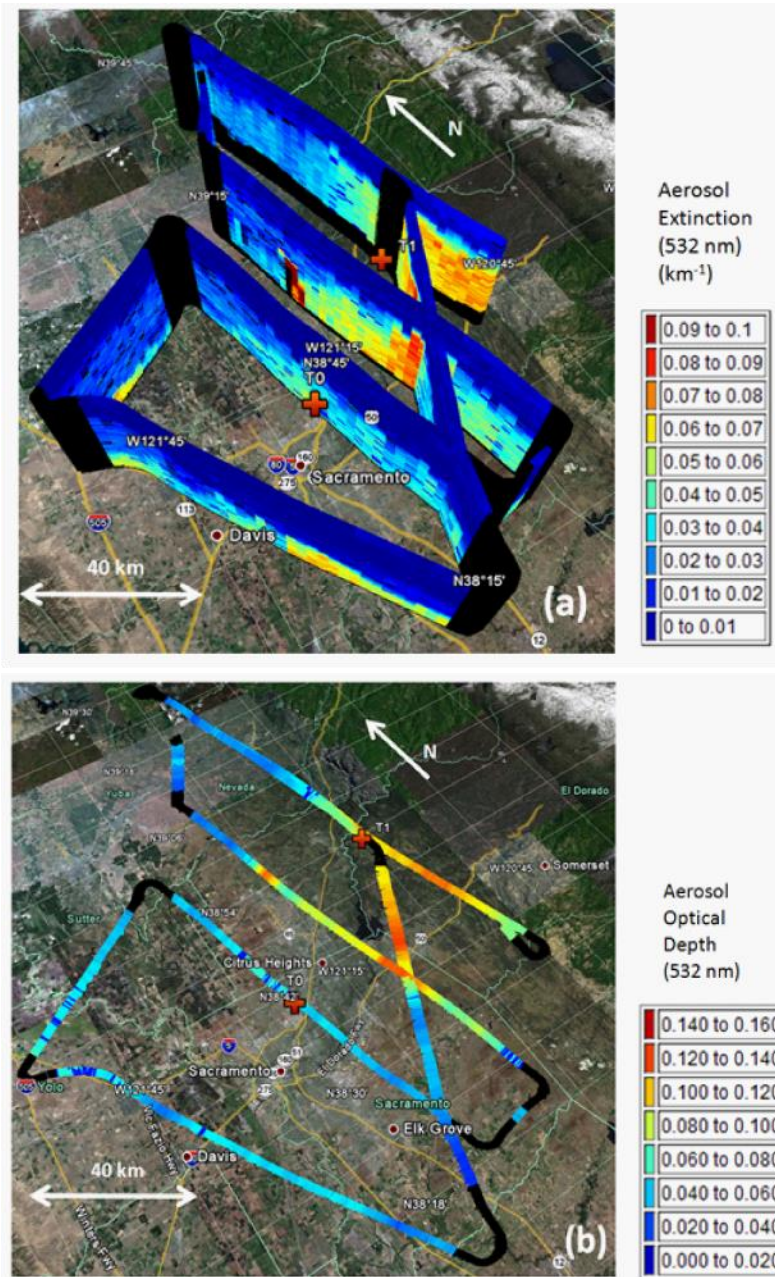
2236
 2237
 2238
 2239
 2240
 2241
 2242
 2243
 2244
 2245
 2246

Figure 22. (a) Aerosol backscatter (532 nm), (b) aerosol depolarization (532 nm), (c) ratio of aerosol depolarization (532/1064 nm), (d) backscatter wavelength dependence ((1064/532 nm) measured by the airborne HSRL between 17:45-18:12 UT on June 19. This portion of the B200 flight covered about 160 km between the Sacramento area (left) and the mountains east of Sacramento (right). The dark area in the bottom part of the images represents the ground surface. (e) aerosol type inferred from the HSRL measurements of aerosol intensive parameters. (f) AOD apportioned to aerosol type.



2247
 2248
 2249
 2250
 2251
 2252
 2253

Figure 23. Semi-Lagrangian G-1 flight tracks on the afternoon of June 28, with the points color coded by: a) CO, b) sum of isoprene, methyl vinyl ketone (MVK), and methacrolein (MACR), c) organic aerosol mass concentration, d) BC mass concentration, e) Nephelometer scattering coefficient at $\lambda = 550$ nm, and f) PSAP absorption coefficient at $\lambda = 523$ nm.



2255

2256

2257

2258

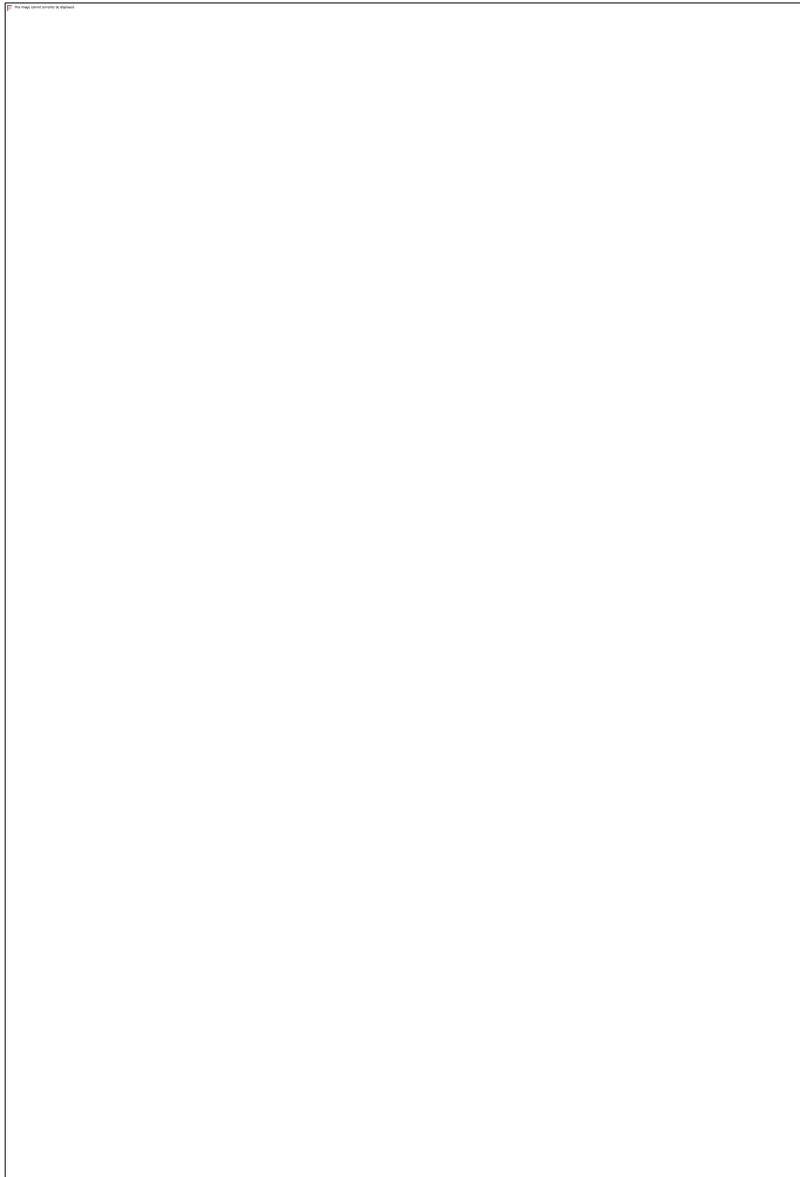
2259

2260

2261

2262

Figure 24. (a) Aerosol extinction (532 nm) profiles derived from airborne HSRL measurements acquired over the Sacramento region between 15:56 PDT and 17:28 PDT on June 28. Profiles acquired between the surface and 3 km altitude are shown. (b) AOD derived from the HSRL measurements along this same flight track. In both panels the locations of the T0 and T1 ground sites are indicated by red crosses.



2263

2264

2265

2266

2267

2268

2269

2270

2271

2272

Figure 25. (a) Ozone mixing ratio profiles measured with the TOPAZ lidar and (b) NO₂ vertical column densities measured with the CU AMAX DOAS system over the Sacramento area on June 28. Data are from two flight segments from 11:28 – 12:03 and 13:04 – 13:52 PDT. The ozone profiles extend from near the ground to 1500 m MSL. The colored line above the ozone “curtain” plot represents the ozone in situ measurements at flight level (approx. 2100 m MSL). The locations of the T0 and T1 ground sites are indicated by yellow pushpin markers.